UNIVERSIDAD NACIONAL AUTÓNOMA DE MÉXICO

POSGRADO EN CIENCIAS FÍSICAS
INSTITUTO DE CIENCIAS FÍSICAS
FÍSICA DE ALTAS ENERGÍAS, FÍSICA NUCLEAR, GRAVITACIÓN Y FÍSICA MATEMÁTICA

BARYON ACOUSTIC OSCILLATIONS ANALYSIS IN THE ERA OF STAGE-IV DARK ENERGY EXPERIMENTS

TESIS
QUE PARA OPTAR POR EL GRADO DE:
MAESTRO EN CIENCIAS (FÍSICA)

PRESENTA:
ALEJANDRO PÉREZ FERNÁNDEZ

TUTOR PRINCIPAL:
DR. SÉBASTIEN MICKAËL MARC FROMENTEAU
INSTITUTO DE CIENCIAS FÍSICAS

COMITÉ TUTOR:
DRA. MARIANA VARGAS MAGAÑA
INSTITUTO DE FÍSICA

DR. JOSÉ RUBÉN ALFARO MOLINA
INSTITUTO DE FÍSICA

CUERNAVACA, MORELOS, AGOSTO 2022

A mis padres

Resumen

Durante sus primeros 400,000 años, el Universo se encontraba en un estado tan caliente y denso que los electrones, bariones y fotones formaban un plasma. La dinámica de este plasma estuvo regida por dos componentes contrapuestos: la gravedad, que hace colapsar a las sobredensidades; y un desequilibrio de presión, que se opone al colapso. Como resultado, ondas sonoras se propagaron libremente a través del plasma hasta la época de recombinación, cuando la velocidad del sonido bajó a cero y las sobredensidades se congelaron. La distancia que una sola perturbación pudo recorrer durante este tiempo se conoce como el horizonte sonoro y es de aproximadamente 150 Mpc. Esta escala característica está impresa en la estadística de dos puntos del Fondo Cósmico de Microondas (CMB), y corresponde a un patrón oscilatorio en el espacio de Fourier, conocido como Oscilaciones Acústicas de Bariones (BAO). Adicionalmente, el mismo patrón se observa en el agrupamiento de galaxias a tiempos tardíos, ya que las sobredensidades que quedaron en la época de recombinación sembraron la formación de estructura a gran escala durante la era dominada por la materia. El patrón oscilatorio se traduce en un solo pico en la función de correlación de dos puntos. De esta manera, la señal de BAO constituye una regla estándar que puede ser utilizada para medir el parámetro de Hubble $H(z)$ y la distancia de diámetro angular $D_A(z)$, ya que se puede calibrar con el valor medido con los datos del CMB. A su vez, la medición de estas cantidades para diferentes corrimientos al rojo resulta en una prueba poderosa para la ecuación de estado de la energía oscura.

El proyecto Dark Energy Spectroscopic Instrument (DESI) es un experimento que actualmente está realizando un sondeo espectroscópico de galaxias con una duración total de 5 años. Se espera que este sondeo genere el mapa más completo del Universo jamás creado. Uno de los objetivos principales de DESI es obtener mediciones de nivel subporcentual tanto para $H(z)$ como para $D_A(z)$. Alcanzar este nivel de precisión requeriría la mitigación de errores sistemáticos en una medida lo suficientemente adecuada. Por lo

tanto, se vuelve indispensable revisar la metodología que se ha utilizado en estudios anteriores.

Este texto se centra en revisar los aspectos principales del método de BAO, así como en presentar algunos de los resultados obtenidos en el contexto de la Etapa 2 del BAO Mock Challenge de la Colaboración DESI. El Mock Challenge tiene como objetivo refinar el *pipeline* utilizado en el análisis cosmológico haciendo uso de catálogos de galaxias provenientes de simulaciones. En particular, los catálogos simulados de ELG provenientes de las simulaciones de UNIT se utilizaron como datos principales, mientras que las matrices de covarianza se construyeron a partir de los catálogos EZmock. Como parte de la Etapa 2, se llevaron a cabo ajustes de BAO considerando distintas variaciones tales como: tipo de matriz de covarianza, algoritmo de reconstrucción, escala de suavizado en la reconstrucción y rango del ajuste. Nuestros resultados muestran una sensibilidad muy baja a todas estas variaciones, lo que puede considerarse como un indicio de la fiabilidad del método.

Nuestro *fitter* de BAO fue implementado en el espacio de configuración y funciona encontrando la distribución posterior de los parámetros del modelo a través de un método Monte Carlo basado en Cadenas de Markov (MCMC). Se utilizó el *sampler* Zeus MCMC, que es una implementación en Python del método *Ensemble Slice Sampling.* La información de las distancias está contenida en los parámetros de dilatación $\alpha_{\|}$ y $\alpha_{\perp}$, paralelo y perpendicular a la línea de visión respectivamente, como consecuencia del efecto Alcock-Paczyński. Estos parámetros son proporcionales al producto $H(z)r_s$ y al cociente $r_s/D_A(z)$, respectivamente, donde r_s es el horizonte sonoro.

Fuimos capaces the probar la metodología con la precisión requerida para los análisis del Año 1 de DESI. Para el catálogo de UNIT utilizado, se encontró un error que corresponde al 25% del error estadístico esperado para el Año 1. Los resultados obtenidos en este trabajo son compatibles, dentro de 2-σ, con la distribución Gaussiana esperada para los errores. Respecto al pronóstico del Año 5, los errores obtenidos son del mismo orden de magnitud, lo que significa que para llevar a cabo el análisis correspondientes al Año 5 será necesario utilizar catálogos sintéticos con un mayor volumen efectivo. Tomando en cuenta las diferentes variaciones en la metodología, se encontró una dispersión del 0.03% y del 0.01% para $\alpha_{\|}$ y $\alpha_{\perp}$, respectivamente; la cual se agregó en cuadratura al error estadístico. Esto significa que, para el catálogo analizado, estas variaciones constituyen un 0.9% del error total para $\alpha_{\|}$ y un 0.4% del error total para $\alpha_{\perp}$

Abstract

During its first 400,000 years, the Universe was in a hot, dense state, such that its electrons, baryons and photons formed a plasma. The dynamics of this plasma was governed by two counteracting components: gravity, which makes the overdensities collapse; and a pressure imbalance, which opposes the collapse. As a result, sound waves propagated freely through the plasma until the recombination epoch, when the sound speed dropped to zero and the overdensities froze. The distance that a single perturbation could travel during this time is known as the sound horizon and it is approximately 150 Mpc. This characteristic scale is imprinted in the two-point statistics of the Cosmic Microwave Background (CMB), and it corresponds to an oscillatory pattern in Fourier space, known as the Baryon Acoustic Oscillations (BAO). In addition, the same pattern is observed in the late-time clustering of galaxies, as the overdensities remaining at the recombination epoch seeded large-scale structure formation during the matter-dominated era. This oscillatory pattern translates into a single peak in the two-point correlation function, where the BAO signal constitutes a standard ruler that can be used to measure the Hubble parameter $H(z)$ and the angular diameter distance $D_A(z)$. In turn, measuring these quantities at different redshifts can yield a powerful probe for the dark energy equation of state.

The Dark Energy Spectroscopic Instrument (DESI) project is a ground-based experiment that is currently conducting a 5-year spectroscopic galaxy survey, which is expected to generate the most comprehensive map of the Universe ever created. One major goal of DESI is to obtain subpercent level measurements for both $H(z)$ and $D_A(z)$. Achieving this level of precision would require the mitigation of systematics to a sufficiently accurate extent. Thus, it becomes paramount to revisit the methodology that has been used in past studies.

This text focuses on reviewing the principal aspects of the BAO method, as well as presenting some of the results obtained in the context of the Stage 2 of the BAO Mock Challenge of the DESI Collaboration. The Mock Chal-

lenge has the objective of refining the pipeline used in the cosmological analysis by making use of mock galaxy catalogues coming from simulations. In particular, ELG mock catalogues coming from the UNIT simulations were used as the main data, while covariance matrices were constructed from EZmock catalogues. As part of the Stage 2, BAO fits were performed examining distinct variations such as: type of covariance matrix, reconstruction algorithm, smoothing scale in the reconstruction, and fitting range. Our results show a very low sensitivity to these variations, showing the method to be reliable.

Our BAO fitter is implemented in configuration space and it works by finding the posterior distribution of the model parameters via a Markov Chain Monte Carlo (MCMC) method. The Zeus MCMC sampler was made use of, which is a Python implementation of the Ensemble Slice Sampling method. The distance information is contained in the dilation parameters $\alpha_{\parallel}$ and $\alpha_{\perp}$, parallel and perpendicular to the line of sight respectively, as a consequence of the Alcock-Paczyński effect. These parameters are proportional to the product $H(z)r_s$ and the ratio $r_s/D_A(z)$, respectively, where r_s is the sound horizon.

We were able to test the methodology with the required precision for the Year 1 analyses. For this UNIT catalogue, we found an error that corresponds to 25% of the statistical error expected for DESI Year 1 data. The results obtained in this work are compatible within 2-σ with the Gaussian distribution expected for the errors. With respect to the Year 5 forecast, the errors obtained are of the same order of magnitude, which means that for Year 5 analyses mocks with greater effective volume would be required in order to reach the required precision. Taking into account the different variations in the methodology, a scattering of 0.03% and 0.01% was found for $\alpha_{\parallel}$ and $\alpha_{\perp}$, respectively; which was added in quadrature to the statistical error. This signifies that, for the analysed mock, these variations could only account for 0.9% of the total error for $\alpha_{\parallel}$ and 0.4% of the total error for $\alpha_{\perp}$.

Agradecimientos

Quisiera agradecer principalmente a mis padres, Carolina y Alejandro, por apoyarme incondicionalmente en todo lo que me he propuesto. Gracias por enseñarme la importancia de la familia y del trabajo duro, así como a nunca darme por vencido. Cada día me inspiran a ser una mejor persona.

Mis amigos también me ayudaron a encontrar inspiración durante estos dos años y medio. Gracias Sergio, David y Adán, por los buenos momentos dentro y fuera del posgrado. Especialmente gracias a Alena, por haberme ayudado a revisar que mi inglés estuviera libre de errores en este texto y por alentarme a salir de la rutina.

Agradezco al Dr. Sébastien Fromenteau y a la Dra. Mariana Vargas por su paciencia, apoyo y dedicación durante mi tiempo en la maestría. Gracias por sus enseñanzas y retroalimentación, que me permitieron adentrarme por primera vez en la fascinante área de la Cosmología. También agradezco al Dr. Rubén Alfaro, quien siempre estuvo pendiente de mi avance.

Agradezco a los Dres. César Bonilla, Alma González, Juan Carlos Hidalgo y Octavio Valenzuela por haber leído esta tesis y por sus valiosos comentarios, que me ayudaron a afinar varios puntos.

Finalmente, agradezco el apoyo a través de los proyectos PAPIIT IN108321 y PAPIIT IA103421 por parte de la DGAPA; así como al CONACYT por la beca otorgada.

Contents

Chapter 1

Introduction

Sound waves that originated in the primordial plasma left an imprint as they stopped propagating at the recombination time. This imprint is known as the baryon acoustic peak. The characteristic scale of this peak is well known from Cosmic Microwave Background (CMB) and Big Bang Nucleosynthesis (BBN) data, and it constitutes a standard ruler, which can be used to measure the expansion history of the universe. The robustness of this method has been demonstrated (Eisenstein, Seo, and White 2007) and it relies on the fact that the acoustic peak cannot be mimicked by systematics. Particularly, these measurements can be used to determine the nature of dark energy, through its equation of state.

The understanding of the baryon acoustic oscillations as a possible hallmark in the matter power spectrum at low redshifts can be traced back to the early 1970's. However, it was not until the late 1990's that it was seriously considered as a feasible standard ruler (cf. Weinberg et al. 2013 for a more detailed chronology). The breakthrough came in 2005 when two separate groups published convincing detections of the BAO signal in the clustering of galaxies (Cole et al. 2005; Eisenstein, Zehavi, et al. 2005). Some years later, the first BAO detection in the Lyman-α forest was reported as well (Busca et al. 2013).

Soon after the first detections, the BAO method was considered of great significance in the context of cosmological model constraints. The Dark Energy Task Force (Albrecht et al. 2006) featured the BAO method as one of the four primary methods to probe dark energy, the other three being Supernovae (SN), Galaxy Cluster (CL) and Weak Lensing (WL). The method has preserved its relevance since then, with Stage IV experiments, such as DESI (DESI Collaboration 2016), currently taking place.

The aim of this chapter is to give a description of the phenomena behind the BAO feature and to establish the connection between the early universe physics and the late-time matter clustering. Section 1.1 provides an over-simplified overview on dark energy that should primarily serve to establish some notation.

1.1 Dark Energy

The concept of *dark energy* arose from the necessity to explain the accelerating expansion of the universe, which was first discovered from type Ia supernovae data (Riess et al. 1998; Perlmutter et al. 1999) [1].

According to the acceleration equation,

$$\frac{\ddot{a}}{a} = -\frac{4\pi G}{3}\left(\rho + 3p\right), \tag{1.1}$$

where $a(t)$ is the scale factor, ρ is the total energy density and p is the total pressure, a positive acceleration could only take place provided that the total equation of state $w = \frac{p}{\rho}$ is such that $w < -\frac{1}{3}$. As matter has a zero equation of state and radiation has a positive one, there must be an extra energy contribution with negative w. We shall call it ρ_{DE}, and this is precisely what we shall refer to as dark energy, regardless of what its nature might be. That is, we should think of dark energy as a generic name for the extra energy contributions as a whole.

The most simple explanation to account for the accelerating expansion is a cosmological constant Λ [2], in which case $\rho_{DE} = \rho_\Lambda = \Lambda/8\pi G$ and $w = -1$. Notwithstanding, in a general sense, observational probes of dark energy concern themselves with three possibilities: (i) $w =$ constant, not necessarily -1, (ii) $w = w(z)$ and (iii) modified gravity.

Eq. (1.1) is supplemented by the Friedmann equation:

$$H^2(z) = H_0^2\left(\Omega_r(1+z)^4 + \Omega_m(1+z)^3 + \Omega_k(1+z)^2 + \Omega_{DE} f(z)\right), \tag{1.2}$$

where H_0 is the Hubble constant, Ω_i is the corresponding density parameter for matter (m), radiation (r), curvature (k) and dark energy (DE), and

$$f(z) = \exp\left(3\int_0^z \frac{1+w(u)}{1+u}du\right), \tag{1.3}$$

---

[1] The complete story is a bit more entangled. See Weinberg et al. 2013.

[2] Note that the existence of a cosmological constant Λ was originally proposed by Einstein more than 80 years before the accelerated expansion was discovered, but in a completely different context. Namely, he was looking for solutions for a static Universe.

which results from integration of the fluid equation with an arbitrary equation of state.

Equations (1.1) and (1.2) completely determine the *background* evolution in a Universe described by the *Friedmann–Lemaître–Robertson–Walker* metric.

When considering constraints for w, it is common practice to use the Chevallier-Polarski-Linder (CPL) parametrisation (Chevallier and Polarski 2001; Linder 2003):

$$w(z) = w_0 + w_a \frac{z}{1+z}, \tag{1.4}$$

which gives

$$f(z) = (1+z)^{3(1+w_0+w_a)} \exp\left(-3w_a \frac{z}{1+z}\right) \tag{1.5}$$

Note that this parametrisation reduces the general problem to constraining a two-parameter space (w_0, w_a).

Now, the objective is to find a way to determine the correct values for w_0 and w_a. Roughly speaking, what we do is look at the equations, ask ourselves how different values of these constants would affect things we can measure, go and measure those quantities, come back to the equations and decide which values fit best with our measurements.

As we shall see, Baryon Acoustic Oscillations provide a way to measure $H(z)$ as well as the angular-diameter distance, $D_A(z)$, and that taking into account both of them together results in strong constraints on the dark energy equation of state.

1.2 The perturbed Universe

Our primary interest is to study the structure formation as the Universe evolves with time. Since structures emerge from perturbations to the background densities, we shall focus on the evolution of perturbations. In order to do so, let us consider the distribution function $f(\boldsymbol{r}, \boldsymbol{p}, t)$ of a single species (cold dark matter, neutrinos, radiation, baryons). Here $\boldsymbol{r}$ is the comoving position vector whose dimensions remained fixed as the Universe expands, $\boldsymbol{p}$ is the physical momentum and t is the cosmic time. The collisionless Boltzmann equation (also known as the Vlasov equation) states that the total number of particles is conserved,

$$\frac{df(\boldsymbol{r}, \boldsymbol{p}, t)}{dt} = \frac{\partial f(\boldsymbol{r}, \boldsymbol{p}, t)}{\partial t} + \dot{\boldsymbol{r}} \cdot \nabla_r f(\boldsymbol{r}, \boldsymbol{p}, t) + \dot{\boldsymbol{p}} \cdot \nabla_p f(\boldsymbol{r}, \boldsymbol{p}, t) = 0. \tag{1.6}$$

Here a dot $\dot{}$ indicates the derivative with respect to the cosmic time t. This equation applies to every single cosmological species and it is a partial differential equation in 7 variables. The usual way to tackle this equations is by taking its different moments in terms of the momentum. The treatment presented in this section is based on Dodelson and Schmidt 2021 and follows the same conventions. Note that treating the momentum involves dealing with the geodesic equation, which in turn will depend on the perturbed metric. Considering the *conformal Newtonian gauge* and taking the first two moments for baryons and cold dark matter yields, at first order,

$$\delta_c' + ikv_c = -3\Phi', \tag{1.7}$$

$$v_c' + \frac{a'}{a}v_c = -ik\Psi \tag{1.8}$$

$$\delta_b' + ikv_b = -3\Phi', \tag{1.9}$$

$$v_b' + \frac{a'}{a}v_b = -ik\Psi + \frac{\tau'}{R}\left(v_b + 3i\Theta_1\right), \tag{1.10}$$

where δ_i and v_i represent the *density contrast* and the *peculiar* velocity (i.e., the velocity relative to the comoving grid), respectively; the subscript c indicates cold dark matter, while b denotes baryons. The density contrast in each case is defined as

$$\delta = \frac{\rho - \bar{\rho}}{\bar{\rho}}, \tag{1.11}$$

with $\bar{\rho}$. Additionally, Ψ corresponds to the Newtonian potential, while Φ can be regarded as a perturbation to the spatial curvature[3]. The quantity τ is the optical depth, Θ_1 is the dipole momentum (see below) of the photon perturbations and R is defined as

$$R(t) = \frac{3\rho_b(t)}{4\rho_\gamma(t)}. \tag{1.12}$$

In these equations, the prime notation $'$ is used to indicate derivative with respect to the conformal time η, defined as

$$\eta(t) = \int \frac{dt}{a(t)}, \tag{1.13}$$

where $a(t)$ is the scale factor.

Note that the equations are written in Fourier space—with k denoting the wavenumber. As it is customary for cosmology texts, we shall distinguish

---

[3] Under the assumption of no anisotropic stress, both potentials are equal $\Psi = -\Phi$.

Fourier transforms of quantities by context or by its arguments, as opposed to making use of a special notation. Working on Fourier space has the advantage that at first order Fourier modes evolve independently.

Photons are completely characterised by its temperature contrast with respect to the background temperature

$$\Theta = \frac{\delta T}{T}. \tag{1.14}$$

This quantity can be decomposed in multipole moments, defined as

$$\Theta_\ell(k,\eta) = \frac{1}{(-1)^\ell}\int_{-1}^{1}\frac{d\mu}{2}\mathcal{L}_\ell(\mu)\Theta(\mu,k,\eta), \tag{1.15}$$

where $\mathcal{L}_\ell$ is the Legendre polynomial of order ℓ and $\mu = \hat{\boldsymbol{p}}\cdot\hat{\boldsymbol{k}}$. This definition is motivated by considering the expansion of Θ in configuration space in terms of spherical harmonics evaluated at the origin (where the observer is located) and then taking into account the Fourier transform.

Equations (1.7) and (1.8) completely describe the evolution of cold dark matter, under the assumption of no anisotropic stress. These equations represent how overdensities tend to grow due to the presence of a gravitational potential, but the growth is slowed down as a consequence of the background expansion (the term proportional to v_c in equation (1.8)).

Analogously, equations (1.9) and (1.10) describe the evolution of baryon overdensities. Note that there is an additional term in (1.10), proportional to the ratio τ'/R, which takes into account the fact that photons are constantly bouncing off electrons via Compton scattering during the radiation-dominated era.

The Boltzmann equation for photons can be written as

$$\Theta' + ik\mu\Theta = -\Phi' - ik\mu\Psi - \tau'\left(\Theta_0 - \Theta + \mu v_b - \frac{1}{2}\mathcal{L}_2(\mu)\Pi\right). \tag{1.16}$$

This is done by taking eq. (1.6) and expanding f around a Bose-Einstein distribution (the photon's zeroth-order distribution). Here

$$\Pi = \Theta_2 + \Theta_{P,2} + \Theta_{P,0}, \tag{1.17}$$

where Θ_P is the photon polarisation field.

Analogously, the equation for the neutrino temperature perturbation $\mathcal{N}$ is

$$\mathcal{N}' + ik\mu\frac{p}{E_\nu(p)}\mathcal{N} - Hp\frac{\partial}{\partial p}\mathcal{N} = -\Phi' - ik\mu\frac{E_\nu(p)}{p}\Psi. \tag{1.18}$$

Note that the energy E_ν, where ν denotes neutrinos, appears explicitly in this equation to account for the fact that their mass is not zero.

This system is supplemented by the Einstein's equations for the perturbed metric:

$$k^2\Phi + 3\frac{a'}{a}\left(\Phi' - \Psi\frac{a'}{a}\right) = 4\pi G a^2\left(\rho_m\delta_m + 4\rho_r\Theta_{r,0}\right), \tag{1.19}$$

$$k^2\left(\Phi + \Psi\right) = -32\pi G a^2 \rho_r \Theta_{r,2}. \tag{1.20}$$

Here, m denotes the total matter and r the total radiation; whereas G is the gravitational constant.

In general, equations (1.7) to (1.20) describe the evolution of overdensities at any given time at linear order. However, it is usually more convenient to focus on specific solutions at the different epochs of interest, since the equations simplify under various circumstances, which helps gain physical insight. For example, in the matter-dominated era, equation (1.19) reduces to the regular Poisson equation.

Although analytical solutions can be approximated under different circumstances, the system of Boltzmann-Einstein equations can be solved numerically. There are various public codes available, among which the most popular are CAMB and CLASS.

1.3 Baryon Acoustic Oscillations

There are two convenient ways to explain the baryon acoustic oscillations phenomena. The first one is considering the standing wave description in Fourier space, while the second consist of considering the travelling waves decomposition in real space.

Le us begin by considering the description in Fourier space of the photon perturbations. During its first 400,000 years, prior to the recombination epoch, the rate of the Compton scattering between electrons and photons was higher than the expansion rate, causing baryons, electrons and photons to constitute a plasma, since neutral atoms were not able to form. The Boltzmann equations take the tightly-coupled limit, under which the evolution of Θ_0 is described by

$$\Theta_0'' + \frac{a'}{a}\frac{R}{1+R}k\Theta_0' + k^2 c_s^2 \Theta_0 = -\frac{k^2}{3}\Psi - \frac{a'}{a}\frac{R}{1+R}\Phi' - \Phi'', \tag{1.21}$$

where the speed of sound is given by

$$c_s(\eta) = \frac{1}{\sqrt{3\left(1 + R(\eta)\right)}}. \tag{1.22}$$

This is the equation of a forced harmonic oscillator in Θ_0, and thus give rise to the oscillatory pattern observed in the CMB power spectrum (cf. Figure 1.1). Note that the acoustic peaks (local maxima) in the CMB that we observed today are the imprint left at the epoch of recombination, since photons have travelled (almost) freely since then. The remarkable feature of this signal is that it can also be detected in the matter clustering at low redshifts, as we shall explain below.

In order to get a picture of what the baryon acoustic peak looks like in configuration space, let us start by considering the universe prior to the recombination epoch and focusing on a single point where a primordial matter density fluctuation took place. This density fluctuation produced a pressure unbalance in the photon-baryon-electron plasma, thus creating a spherical sound wave, much like the effect of dropping a pebble into a pond. The sound wave travels outwards from the initial perturbation until the recombination time at a speed c_s. At this moment, the speed of sound drops, causing the wave to stop propagating. As a result, the baryon overdensities at the spherical wavefront freeze in place. The (comoving) radius up to which the sound wave travelled before stopping is known as the sound horizon,

$$r_s = \int_{z_{rec}}^{\infty} c_s(z) \frac{dz}{H(z)}, \tag{1.23}$$

which, according to CMB+BBN data, has a value of $r_s \approx$ 150 Mpc. In contrast, while this process was occurring, the initial dark matter overdenisty grew at the initial point and became much larger than the baryon overdensity at the spherical shell. Consequently, both overdense regions serve to seed large-structure formation in the matter-dominated era. The whole process is illustrated in Figure 1.2, which follows the density profile of a density shell.

As a consequence of this process, we would expect to observe an excess of correlation between galaxies at the characteristic distance of the sound horizon—since galaxies are known to form within dark matter halos. This translates into observing a peak in the two-point correlation function (introduced in the next section).

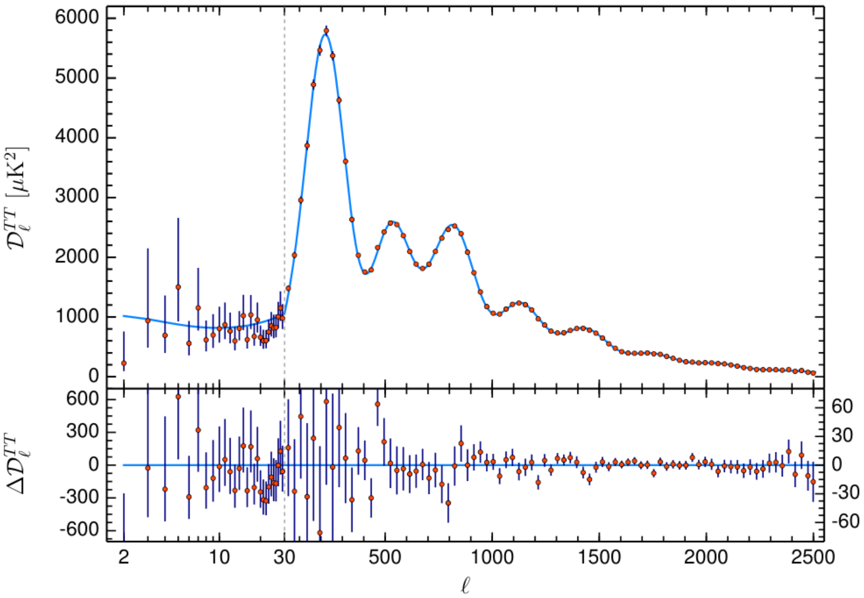

Figure 1.1: Temperature power spectrum of the CMB. Taken from Planck Collaboration, Aghanim, et al. 2020. The blue line represents the theoretical ΛCDM model. The x-axis ℓ indicates the multipole moment. The y-axis correspond to $D_\ell^{TT} = \ell(\ell+1)C(\ell)T_0^2/2\pi$, where T_0 is the mean temperature of the CMB, while $C(\ell)$ is the angular power spectrum (i.e., the variance of the harmonic coefficients in the expansion of Θ in terms of spherical harmonics). Computing $C(\ell)$ requires knowing the values for Θ_ℓ at the present time, which in turn can be written in terms of the monopole and dipole at the recombination time. The oscillatory pattern comes primarily from the monopole contribution, described by eq.(1.21).

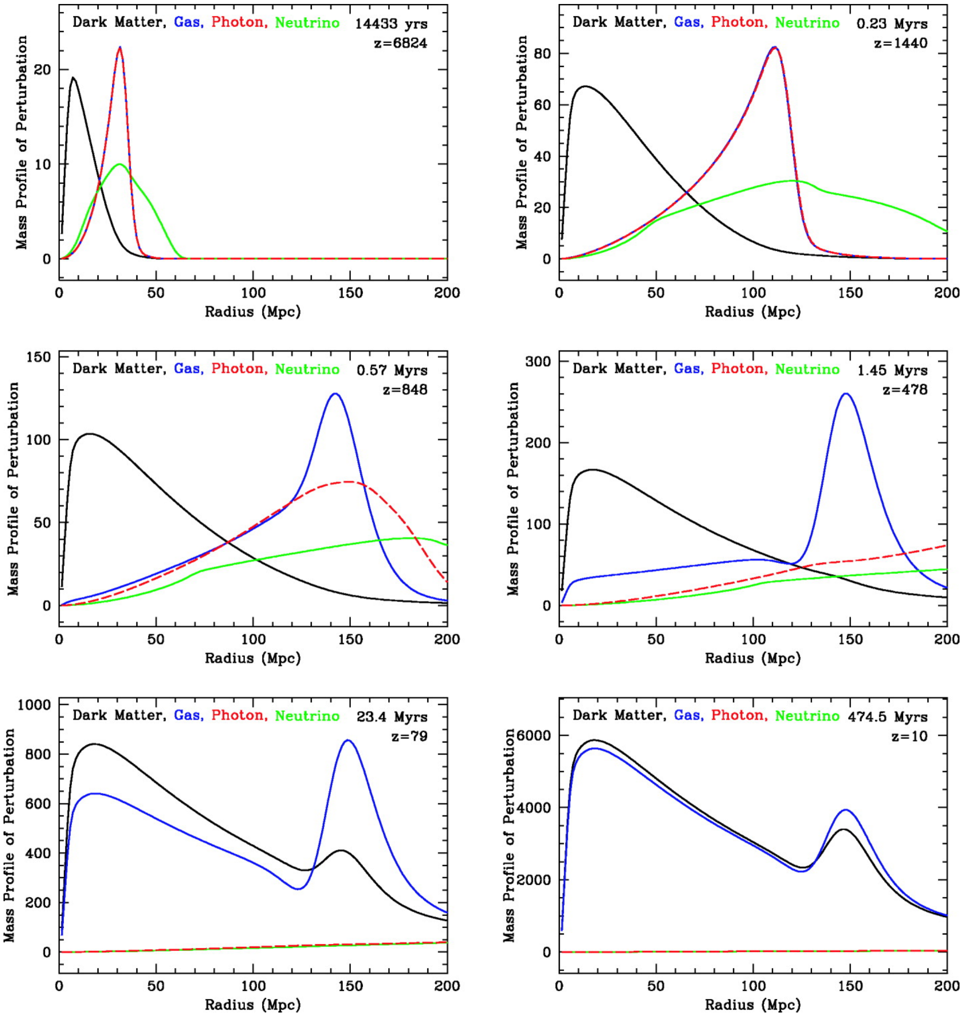

Figure 1.2: Evolution of the radial overdensity profile of a point-like perturbation. The x-axis denotes the distance from the origin, where the initial perturbation takes place, whereas the y-axis represents the mass profile of the perturbations. The panels are ordered from left to right and from top to bottom. Initially, all of the species are perturbed at the same point (assuming the perturbations to be adiabatic). The spherical shell of baryons (gas) and photons travel outwards jointly until recombination time at approximately $z \sim 1100$. After that time, the photons decouple from the baryons and begin to move freely. Meanwhile, the cold dark matter overdensity has grown in place. Finally, during the matter-dominated era, gravity causes the profiles of both dark matter and baryons to be almost identical. Figure taken from Eisenstein, Seo, and White 2007.

1.4 Two-point correlation function and power spectrum

When studying the galaxy distribution in the universe, we would like to have a measure of the clustering; in other words, we would like to know, given a radius r, what is the probability that any two galaxies stay a distance r apart from each other. The two-point correlation function, $\xi(r)$, can be interpreted as the excess probability in comparison to what we would expect if the galaxies were randomly distributed:

$$dP(r) = n(1 + \xi(r))dV, \tag{1.24}$$

where n is the mean number density.

In practice, in order to calculate $\xi(r)$, distances between pairs of galaxies are measured, and then compared with random catalogues. The most common way to determine the two-point correlation function is using the Landy-Szalay estimator (Landy and Szalay 1993):

$$\xi(r) = \frac{1}{RR(r)}\left[DD(r)\left(\frac{n_R}{n_D}\right)^2 - 2DR(r)\left(\frac{n_R}{n_D}\right) + RR(r)\right], \tag{1.25}$$

where n_D and n_R are the number densities of the data and the random catalogue, respectively; DD is the count of pairs of galaxies a distance r apart in the observational data, RR is the equivalent for the random catalogue and DR is the count between the data and the random catalogue.

In contrast, the theoretical matter two-point correlation function is defined as

$$\xi(r) = \langle \delta_m(\boldsymbol{x})\delta_m(\boldsymbol{x}+\boldsymbol{r})\rangle_{\boldsymbol{x}}, \tag{1.26}$$

where $\langle\rangle_{\boldsymbol{x}}$ denotes the ensemble average. The correlation function is assumed to be dependent on the magnitude of $\boldsymbol{r}$ only by virtue of statistical homogeneity and isotropy. As we shall see in the next chapters, comparing measurements of the 2 point statistic from a galaxy survey to those coming from theory will play the central role in the BAO method.

As noted earlier, the acoustic peak is an expected feature of the two-point correlation function. Recall that the power spectrum, $P(k)$, is defined to be the Fourier transform of $\xi(r)$, so that the information contained in the peak will corresponds to an oscillatory pattern in the power spectrum, which is what we refer to as *baryon acoustic oscillations*. A comparison between $\xi(r)$ and $P(k)$ is shown in Figure 1.3.

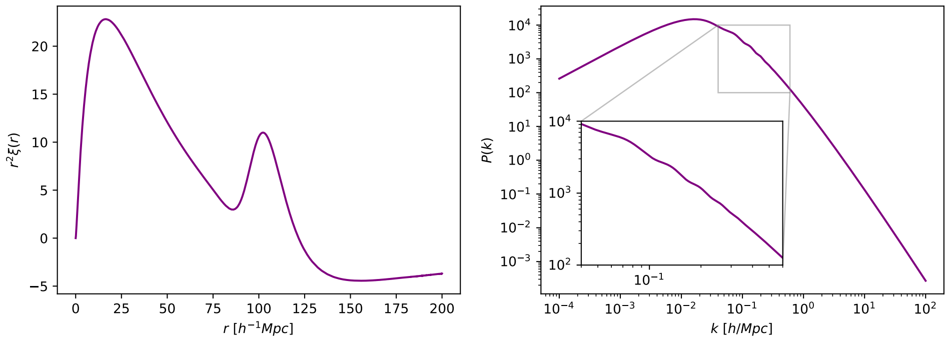

Figure 1.3: Left: Two-point correlation function; the acoustic peak is located approximately at $100h^{-1}$ Mpc. Note that it is usual to multiply by r^2 when plotting, as it makes it easier to distinguish the peak. Right: The corresponding power spectrum, where the peak in $\xi(r)$ translates into oscillatory behaviour, as shown in the inset. The power spectrum was computed for $z = 0.5$ using CAMB, the two-point correlation function was computed by Fourier transforming. The peak looks sharp (and the oscillations neat) because non-linear effects were not included.

Chapter 2

The BAO template

The BAO method consists in making use of the BAO signal observed in the late-time 2-point statistics of galaxies in order to measure the angular-diameter distance $D_A(z)$ and the Hubble parameter $H(z)$ at the effective redshift of a galaxy catalogue. In order to do so, data has to be compared with theory. The BAO measurement is so robust that, generally, it is not necessary to use a sophisticated theoretical model that accurately accounts for broad-band modifications to the linear power spectrum/correlation function—as one would expect, for example, from a perturbation theory approach. It is sufficient to use a *template* that correctly describes the relevant physics for this measurement. This chapter is concerned with introducing the most important aspects for constructing such template.

When surveying the sky, there is direct access to angular positions and redshift measurements, which afterwards can be converted into comoving coordinates, thus yielding a 3D map of the corresponding patch in the sky. When converting from redshift space to real space, a fiducial cosmology has to be assumed. A wrong assumption will bring about a distortion in the *observed* coordinates relative to the *real* coordinates. Moreover, redshift measurements are contaminated by *peculiar velocities*, i.e. velocities relative to the comoving grid, which in turn will contaminate the real space measurements. The former effect is known as the Alcock-Paczyński effect (Alcock and Paczynski 1979), whereas the latter is referred to as redshift-space distortions (RSD).

While having to deal with these effects might seem daunting at first, they are, in fact, powerful tools to gain insight into different cosmological information. In particular, the Alcock-Paczyński test is of prime importance in the context of the BAO method, since it allows for breaking the degeneracy between the corresponding $D_A(z)$ and $H(z)$ measurements. In contrast, RSD measurements comprise information concerning the growth of structure, and analysis of this sort are often focused on constraining the logarithmic growth rate f, which in turn can be used to test General Relativity. The proper description of how these two effects are to be taken into account will be given in sections 2.1, 2.2 and 2.3.

As the gravitational collapse evolves with time, the BAO imprint in the galaxy power spectrum/correlation function undergoes some degradation due to the effects of bulk flows and non-linear collapse. We shall review how this comes about in section 2.5. Section 2.6 will be dedicated to describing *reconstruction* techniques, which roughly speaking is a method applied to the data in order to "undo" the effects that wash out the acoustic signature.

Finally, in section 2.7 the template that takes into account all of the above-mentioned effects will be presented, along with a number of variations that have been used in some relevant articles.

2.1 Redshift Space distortions

In a spectroscopic survey, distances to galaxies are inferred from their redshift, which is determined by the Hubble flow—which reflects the actual comoving position—plus peculiar velocities of galaxies. The Doppler effect induced by peculiar velocities modifies the measured redshift yielding

$$1 + z = \frac{1}{a}(1 + v). \tag{2.1}$$

Note that we simply denote v to the peculiar velocity, to be consistent with the fact that our treatment has focused on comoving coordinates.

As a result of this contamination, the observed comoving positions of tracers will appear shifted relative to the real ones. If we denote $\boldsymbol{s}$ to the position in *redshift space* then

$$\boldsymbol{s} = \boldsymbol{r} + \frac{\boldsymbol{v} \cdot \hat{\boldsymbol{n}}}{aH}\hat{\boldsymbol{n}}, \tag{2.2}$$

where $\hat{\boldsymbol{n}}$ is a unit vector pointing along the line of sight.

The density contrast field measured in redshift space $\delta^s(\boldsymbol{s})$ will differ with respect to the real one, since peculiar velocities will make tracers systematically appear closer or further away from overdensities or underdensities, depending on the observed scales. While statistical homogeneity will be lost in redshift space, rotational symmetry will still hold around the observer. Strictly speaking the two-point statistics in redshift space should be functions of three arguments (Hamilton 1998):

$$\xi(r) \to \xi^s(s_1, s_2, |\boldsymbol{s}_1 + \boldsymbol{s}_2|) \tag{2.3}$$

$$P(k) \to P^s(k_1, k_2, |\boldsymbol{k}_1 + \boldsymbol{k}_2|). \tag{2.4}$$

Here and hereafter in this text, quantities with no subscript will refer to those of tracers/galaxies, as opposed to matter, unless otherwise specified.

If the region of space dealt with is sufficiently distant from the observer, so that it subtends a small angle on the sky, then the distortions can be considered as happening along one of the Cartesian axes. This is commonly refer to as the *distant observer* or *plane parallel* approximation. In this case, the analysis simplifies, since now the power spectrum and the correlation function reduce to functions of two arguments, such as

$$\xi^s(s_1, s_2, |\boldsymbol{s}_1 + \boldsymbol{s}_2|) \to \xi^s(s_\parallel, s_\perp), \tag{2.5}$$

$$P^s(k_1, k_2, |\boldsymbol{k}_1 + \boldsymbol{k}_2|) \to P^s(k_\parallel, k_\perp), \tag{2.6}$$

where $s_\parallel$ and $s_\perp$ are the components of $|\boldsymbol{s}_1 + \boldsymbol{s}_2|$ parallel and perpendicular to the line of sight, respectively. And analogously for $k_\parallel$ and $k_\perp$. Furthermore, under the distant observer approximation, statistical homogeneity is recovered.

Alternatively, it is common practice to work with

$$(s, \mu) = \left(\sqrt{s_\parallel^2 + s_\perp^2}, s_\parallel/s\right), \tag{2.7}$$

$$(k, \mu_k) = \left(\sqrt{k_\parallel^2 + k_\perp^2}, k_\parallel/k\right). \tag{2.8}$$

It should be clear that μ and μ_k are different variables, so that when there is no risk of confusion, we shall drop the subscript when working on Fourier space. The μ variable in both cases is simply the cosine of the angle between the vector in the corresponding space and the line of sight direction. One of the advantages of working with this variables is the fact that the correlation function and the power spectrum can be written in terms of a multipole expansion:

$$\xi^s(s, \mu) = \sum_{\ell=0}^{\infty} \xi_\ell(s)\mathcal{L}_\ell(\mu), \tag{2.9}$$

$$P^s(s, \mu) = \sum_{\ell=0}^{\infty} P_\ell(s)\mathcal{L}_\ell(\mu), \tag{2.10}$$

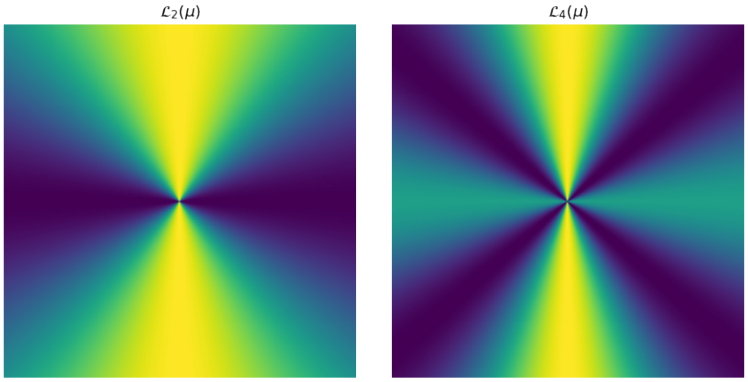

Figure 2.1: Legendre polynomials of order 2 and 4 as a function of the cosine of the angle relative to the line of sight. The line of sight lies along the vertical direction and the centre of each figure corresponds to the centre of reference.

with

$$\xi_\ell(s) = \frac{2\ell+1}{2}\int_{-1}^{1} d\mu\ \xi^s(s,\mu)\mathcal{L}_\ell(\mu), \tag{2.11}$$

$$P_\ell(k) = \frac{2\ell+1}{2}\int_{-1}^{1} d\mu\ P^s(k,\mu)\mathcal{L}_\ell(\mu), \tag{2.12}$$

where $\mathcal{L}_\ell$ is the Legendre polynomial[1] of order ℓ. Figure 2.1 shows the Legendre polynomials of order 2 and 4 as a function of μ. In real space, the only non-zero multipole would be the monopole ($\ell = 0$). In this case, RSD anisotropies give rise to the higher-order multipoles. Due to symmetry, the odd-order multipoles are always zero. In addition, multipoles in configuration space are related to those in Fourier space, via

$$\xi_\ell(s) = i^\ell \int \frac{k^3 d\log(k)}{2\pi^2} P_\ell(k) j_\ell(kr), \tag{2.13}$$

where j_ℓ is the spherical Bessel function of order ℓ.

The multipoles of the correlation function/power spectrum will be the central object of our study. The multipoles for a given catalogue of galaxies

---

[1] Note that in the literature Legendre polynomial are usually denoted as P_ℓ. We have avoided this notation, in order to avoid confusion with the power spectrum.

will be the data to be fitted to the theoretical template for the multipoles described in this chapter.

The rest of this section is devoted to the description of how clustering is distorted in redshift-space. Phenomenologically, redshift-space distortions (RSD) can be divided into two contributions: distortions due to coherent motion and distortions due to incoherent velocities. The former is of linear nature and mainly affects large scales measurements; it introduces a *squashing* effect along the line of sight. The other type of RSD has a non-linear behaviour, which takes place at small scales, where structure formation has already virialised. This type of effect brings about a peculiar feature in which overdensities seem to elongate along the line of sight at sufficiently small scales. We shall refer to this effect as the *Finger of God* effect.

A brief account of linear RSD is given in the following subsection 2.1.1, where it is shown how the amplitude of the linear redshift-space power spectrum differs from that of the real-space one by a factor which depends on μ^2 only, known as the *Kaiser Boost* term (Kaiser 1987). In subsection 2.1.2 the Finger of God effect is discussed.

2.1.1 Kaiser Boost

In the plane parallel approximation, the redshift space position vector $\boldsymbol{s}$ is given by

$$\boldsymbol{s} = \boldsymbol{r} + \frac{v_z(\boldsymbol{r})}{aH}\hat{\boldsymbol{z}}, \tag{2.14}$$

where we have arbitrarily chosen the z direction as the line-of-sight direction.

The relation between redshift space and real space is merely a change of coordinates, which means that the number of galaxies in a given infinitesimal volume element in redshift space should be the same number of galaxies quantified in the corresponding infinitesimal volume element in real space. In other words, conservation of matter implies that

$$(1 + \delta^s(\boldsymbol{s}))\, d^3s = (1 + \delta(\boldsymbol{r}))\, d^3r, \tag{2.15}$$

which is equivalent to

$$J\,(1 + \delta^s(\boldsymbol{s})) = 1 + \delta(\boldsymbol{r}), \tag{2.16}$$

where $J = \left|\frac{\partial \boldsymbol{s}}{\partial \boldsymbol{r}}\right|$ is the Jacobian. Notice that

$$\frac{\partial \boldsymbol{s}}{\partial \boldsymbol{r}} = \begin{pmatrix} 1 & 0 & 0 \\ 0 & 1 & 0 \\ \frac{\partial v_z}{\partial x}/(aH) & \frac{\partial v_z}{\partial y}/(aH) & 1 + \frac{\partial v_z}{\partial z}/(aH) \end{pmatrix}, \tag{2.17}$$

which yields

$$\left|\frac{\partial \boldsymbol{s}}{\partial \boldsymbol{r}}\right| = 1 + \frac{1}{aH}\frac{\partial v_z}{\partial z}. \tag{2.18}$$

Thus,

$$\delta^s(\boldsymbol{s}) = \left(1 + \frac{1}{aH}\frac{\partial v_z}{\partial z}\right)^{-1}(1+\delta(\boldsymbol{r})) - 1. \tag{2.19}$$

This expression is valid at every order and at any scale range, under the plane parallel approximation. At linear order it simplifies to

$$\delta^s(\boldsymbol{r}) = \delta(\boldsymbol{r}) - \frac{1}{aH}\frac{\partial v_z}{\partial z}. \tag{2.20}$$

That being said, galaxies do not constitute an unbiased tracer of the underlying matter distribution. For example, if two sets of galaxies are selected in different ways, the correlation functions computed for the different sets will differ in amplitude but not in shape.

The linear biasing model establishes that the galaxy overdensity field is related to the matter overdensity field by a constant factor b, while the velocity field is assumed to be unbiased, as the galaxies follow the total matter velocity field exceptionally well at first order:

$$\delta(\boldsymbol{r}) = b\delta_m(\boldsymbol{r}), \tag{2.21}$$

$$\boldsymbol{v}(\boldsymbol{r}) = \boldsymbol{v}_m(\boldsymbol{r}). \tag{2.22}$$

Linear bias can be justified at linear order and at large scales (Dodelson and Schmidt 2021), although it must be pointed out that, in general, b depends on the galaxy sample considered as well as redshfit.

Recall that the linearised continuity equation for matter is

$$\dot{\delta}_m + \frac{1}{a}\nabla\cdot\boldsymbol{v}_m = 0, \tag{2.23}$$

which in terms of the galaxy overdensity and using the linear solution can be rewritten as

$$\frac{1}{b}aHf\delta + \nabla\cdot\boldsymbol{v} = 0. \tag{2.24}$$

In Fourier space,

$$\frac{1}{b}aHf\delta + i\boldsymbol{k}\cdot\boldsymbol{v} = 0. \tag{2.25}$$

Assuming that the velocity is a longitudinal field (i.e., its curl is zero),

$$\boldsymbol{v}(\boldsymbol{k}) = i\frac{\boldsymbol{k}}{k^2}\beta aH\delta, \tag{2.26}$$

where the linear distortion parameter is defined as

$$\beta = \frac{f}{b}. \tag{2.27}$$

Replacing (2.26) into the Fourier-space version of (2.20) yields

$$\delta^s(\boldsymbol{k}) = \left(1 + \beta\mu^2\right)\delta(\boldsymbol{k}), \tag{2.28}$$

where $\mu = k_z/k$ is the cosine of the angle between the wavevector $\boldsymbol{k}$ and the line of sight. This implies that the redshift-space power spectrum is related to the real-space power spectrum through

$$P^s(k,\mu) = \left(1 + \beta\mu^2\right)^2 P(k), \tag{2.29}$$

where the prefactor $\left(1 + \beta\mu^2\right)^2$ is known as the Kaiser Boost.

The interpretation of eq. (2.28) is straightforward. Along the line of sight, overdensities are enhanced, for galaxies appear closer together than they really are. The opposite is observed with underdensities.

2.1.2 Finger of God effect

At small scales, the linear analysis discussed in the previous section is no longer valid. Thermal motions cause redshift surveys to feature an elongation along the line of sight within virialised structures; these features are commonly known as *Fingers of God* (Jackson 1972). In terms of the clustering, this effect introduces a damping factor in the observed galaxy power spectrum. Clustering measurements from galaxy surveys are consistent with $P^s(k,1)/P^s(k,0)$ being a Lorentzian function, which in turn, corresponds to a exponential probability distribution function for the pairwise velocities along the line of sight (see for example Landy, Szalay, and Broadhurst 1998; Landy 2002, or Davis and Peebles 1983 for a configuration space equivalent.)

Assuming the velocity distribution is independent of scale and neglecting the effects of infall, the redshift-space two-point correlation function can be written as a convolution:

$$\xi^s(s_\parallel, s_\perp) = \int dr_\parallel \xi\left(\sqrt{r_\parallel^2 + r_\perp^2}\right)\mathcal{P}\left(aH(s_\parallel - r_\parallel)\right), \tag{2.30}$$

where $\mathcal{P}$ is the pairwise-velocity probability distribution function. This equation illustrates how a galaxy at a distance $r_\parallel$ is mapped into a separation $s_\parallel$ by virtue of its peculiar velocity $v_\parallel = aH(s_\parallel - r_\parallel)$ with a given probability $\mathcal{P}(v_z)$.

In Fourier space, the convolution can we rewritten as a product,

$$P^s(\boldsymbol{k}) = \mathcal{P}(\boldsymbol{k})P(k). \tag{2.31}$$

In principle, $\mathcal{P}$ should account for both small and large scales effects. As stated above, the small scale contribution is consistent with

$$\mathcal{P}(\boldsymbol{k}) \rightarrow \mathcal{D}(k\mu\sigma_p) = \frac{1}{1 + k^2\mu^2\sigma_p^2/2,} \tag{2.32}$$

where σ_p is the pairwise velocity dispersion. Measured values estimate $\sigma_p \sim 300$–400 km/s. Notice that in fact, from previous equation σ_p has units of Mpc/h so that the conversion factor H_0 is needed when reporting values in velocity units. Under this phenomenological description, the total redshift-space power spectrum is then written as

$$P^s(\boldsymbol{k}) = \mathcal{D}(k\mu\sigma_p)(1 + \beta\mu^2)^2 P(k). \tag{2.33}$$

Some authors (J. A. Peacock and Dodds 1994; Fisher et al. 1994) have also opted for a Gaussian velocity distribution, for which

$$\mathcal{D}(k\mu\sigma_p) = \exp[-k^2\mu^2\sigma_p^2/2]. \tag{2.34}$$

This is a good approximation, that can simplify the calculations in certain circumstance (see for example Wang, B. Reid, and White 2013).

2.2 Alcock-Paczyński effect

In addition to the RSD corrections discussed in the previous section, the transformation from measured redshifts into actual distances requires further attention. In order to carry out such transformation, a *fiducial* cosmology has to be assumed (i.e. a set of cosmological parameters). The computed distance as a function of redshift is

$$\chi(z) = \int_0^z \frac{dz'}{H^{\rm fid}(z')}, \tag{2.35}$$

where $H^{\rm fid}(z)$ is given by eq. (1.2).

In real life, it is uncertain whether a given fiducial cosmology actually represents the Universe we live in or not. Essentially, clustering analyses are focused on finding constraints on one or more parameters as it would be unatural if such parameters where known a priori with sufficient accuracy.

As a consequence choosing the wrong parameters, the obtained comoving 3D map will be distorted. Alcock and Paczynski 1979 were the first to notice that this effect could be used to probe the expansion history of the Universe.

In order to illustrate this effect, let us consider a hypothetical spherical overdensity. Assuming this overdensity to be far enough from the observer, the separation difference between its nearest and most distant point will be measured to be

$$r_{\parallel}^{\mathrm{fid}} = \frac{\Delta z}{H^{\mathrm{fid}}(z)}, \tag{2.36}$$

where Δz is the difference in redshift between both points, whereas z can be taken as the redshift at the centre of the overdensity. Note that this distance is measured entirely along the line of sight. The *real* separation, however, will be given by

$$r_{\parallel} = \frac{\Delta z}{H(z)}, \tag{2.37}$$

where $H(z)$ is the *real* Hubble factor, computed with the proper cosmological parameters. Analogously, the fiducial and real transverse separation of two diametrically opposed points, will be given by

$$r_{\perp}^{\mathrm{fid}} = (1+z)D_A^{\mathrm{fid}}(z)\Delta\theta, \tag{2.38}$$

$$r_{\perp} = (1+z)D_A(z)\Delta\theta, \tag{2.39}$$

where $D_A(z)$ is the angular diameter distance, whereas $\Delta\theta$ is the angle subtended in the sky between both points. In this fashion, we can define the dilation parameters

$$\alpha_{\parallel} = \frac{H^{\mathrm{fid}}(z)}{H(z)}, \tag{2.40}$$

$$\alpha_{\perp} = \frac{D_A(z)}{D_A^{\mathrm{fid}}(z)}, \tag{2.41}$$

along and transverse to the line of sight, respectively.

Notice that if the diameter of the overdensity is a known value, then measurements of $\alpha_{\parallel}$ and $\alpha_{\perp}$ can turn into independent measurements of $H(z)$ and $D_A(z)$. In contrast, if the diameter is not known, but the overdensity is known to be spherical, then the ratio (Ballinger, J. A. Peacock, and Heavens 1996)

$$F = \frac{\alpha_{\parallel}}{\alpha_{\perp}} \tag{2.42}$$

can turn into a measurement of the product $H(z)D_A(z)$. The physical interpretation of F should be clear: $F > 1$ ($F < 1$) indicates that the object will appear elongated along (across) the line of sight.

2.3 BAO as a standard ruler revisited

As described in the previous section, having a spherical overdensity as a reference allows for probing the expansion history of the Universe. In real life, however, spherical overdensities are evidently not observed in the sky. What is observed are galaxies that are scattered following an underlying matter distribution. Notwithstanding, the BAO signal imprinted on the late matter 2-point statistics can serve as the characteristic scale used in order to exploit the Alcock-Paczyński effect. This section will outline how this is done.

Consider a number of primordial overdensities, around which a spherical wave travelled outwards up to the recombination time (cf. section 1.3). Were these initial overdensities sufficiently rarefied, we would be able to distinguish the spherical overdensity shells as illustrated by the schematic model in the left panel of Fig. 2.2. This is certainly not the case for the galaxy distribution we observe, which is more similar to what is shown in the right panel of the same figure. The sound horizon scale, thus, should be extracted statistically, via the 2-point correlation function (power spectrum) where the peak (oscillatory pattern) corresponds to the characteristic scale. As with any other distance measurement, the sound horizon measured from a galaxy redshift survey may be distorted due to wrong assumption when selecting the fiducial cosmology in the distance-redshift relation. Since the real value is well known from CMB two-point statistics (at $z \approx 1100$) together with BBN, this scale can be used as the reference calibration when taking into account the Alcock-Packynski effect. We thus refer to the BAO signal as a *statistical* standard ruler.

Let us now see how this is to be taken into account quantitatively. Let us denote $\boldsymbol{s}$ to the fiducial position vector and $\boldsymbol{s}'$ to the one calculated with the *true* cosmological parameters, so that

$$\boldsymbol{s} = \int_0^z \frac{dz'}{H^{\mathrm{fid}}(z')}\hat{\boldsymbol{s}}, \tag{2.43}$$

$$\boldsymbol{s}' = \int_0^z \frac{dz'}{H(z')}\hat{\boldsymbol{s}}, \tag{2.44}$$

where $\hat{\boldsymbol{s}}$ is a unit vector determined by the two measured angles in the sky. Notice that we have made use of the letter s to make emphasis that the treatment is effectively in redshift space, since the z on the integral limit contains the peculiar velocity contribution.

In principle, the dilation parameters discussed on the previous section depend on redshift. In practice, redshifts are close enough that we can

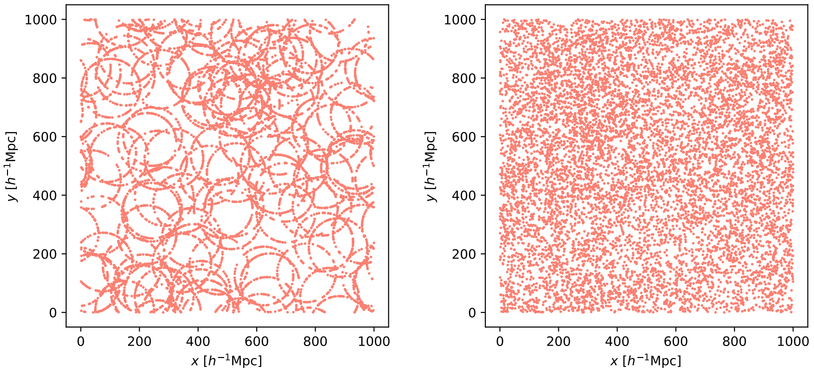

Figure 2.2: Schematic model of a distribution of particles in 2D where there is a preferred length scale equal to the sound horizon. In both panels, the number density is the same. On the left, there is a small number of shells, each shell contains several particles; making the characteristic scale easily distinguishable. On the right, the number of shells is 10 times larger, and there are fewer particles per shell. The characteristic scale cannot be determined just by looking at the distribution. This figure is inspired by a similar one found in Bassett and Hlozek 2009.

assume the alpha parameters to be constant and evaluated at the effective redshift of the survey (Eisenstein, Zehavi, et al. 2005). Moreover, since the sound horizon is being used as the reference, it is common practice to redefine

$$\alpha_{\parallel} = \frac{H^{\text{fid}}(z) r_s^{\text{fid}}}{H(z) r_s}, \tag{2.45}$$

$$\alpha_{\perp} = \frac{D_A(z) r_s^{\text{fid}}}{D_A^{\text{fid}}(z) r_s}. \tag{2.46}$$

The *observed* correlation function will be the same as the *true* one (in redshift-space),

$$\xi^{\text{obs}}(\boldsymbol{s}) = \xi^s(\boldsymbol{s}'[\boldsymbol{s}]), \tag{2.47}$$

where each separation vector can be split into a line-of-sight component and a transverse 2D vector, which yields

$$\boldsymbol{s}' = s'_{\parallel}\hat{\boldsymbol{n}} + \boldsymbol{s}'_{\perp} = \alpha_{\parallel} s_{\parallel}\hat{\boldsymbol{n}} + \alpha_{\perp}\boldsymbol{s}_{\perp}, \tag{2.48}$$

where $\hat{\boldsymbol{n}}$ is the unit vector along the line of sight.

Thus in (s, μ) coordinates the transfomation is given by

$$s' = \alpha_\perp s \left[1 + \mu^2 \left(F^2 - 1\right)\right]^{1/2}, \tag{2.49}$$

$$\mu' = F\mu \left[1 + \mu^2 \left(F^2 - 1\right)\right]^{-1/2} \tag{2.50}$$

with the same definition of F as in 2.42.

In Fourier space,

$$\begin{aligned} P^{\mathrm{obs}}(\boldsymbol{k}) &= \int d^3 s e^{-i\boldsymbol{k}\cdot\boldsymbol{s}} \xi^s(\boldsymbol{s}'[\boldsymbol{s}]) \\ &= \int d^3 s' J e^{-i\boldsymbol{k}\cdot\boldsymbol{s}[\boldsymbol{s}']} \xi^s(\boldsymbol{s}'), \end{aligned} \tag{2.51}$$

where in this case the Jacobian is

$$J = \left|\frac{\partial \boldsymbol{s}}{\partial \boldsymbol{s}'}\right| = \frac{\left((1+z)D_A^{\mathrm{fid}}(z)\right)^2}{\left((1+z)D_A(z)\right)^2} \left|\frac{ds}{ds'}\right| = \left(\frac{D_A^{\mathrm{fid}}(z)}{D_A(z)}\right)^2 \frac{H(z)}{H^{\mathrm{fid}}(z)}, \tag{2.52}$$

notice that in the second equality we have made use of the fact that angular positions are not distorted, while in the third equality the derivate was replaced by

$$\frac{ds}{ds'} = \frac{ds}{dz}\frac{dz}{ds'} = \frac{H(z)}{H^{\mathrm{fid}}(z)}. \tag{2.53}$$

Hence, the Jacobian can be rewriten as

$$J = \left(\frac{r_s^{\mathrm{fid}}}{r_s}\right)^3 \frac{1}{\alpha_\perp^2 \alpha_\parallel}. \tag{2.54}$$

In addition, the dot product can be explicitly expanded as

$$\boldsymbol{k} \cdot \boldsymbol{s} = k_\parallel \frac{s'_\parallel}{\alpha_\parallel} + \boldsymbol{k}_\perp \cdot \frac{\boldsymbol{s}'_\perp}{\alpha_\perp} = \boldsymbol{k}' \cdot \boldsymbol{s}', \tag{2.55}$$

where the true wavenumber is given by

$$\boldsymbol{k}' = \frac{k_\parallel}{\alpha_\parallel}\hat{\boldsymbol{n}} + \frac{\boldsymbol{k}_\perp}{\alpha_\perp}. \tag{2.56}$$

Consequently, the observed power spectrum will be related to the true one through

$$P^{\mathrm{obs}}(\boldsymbol{k}) = \left(\frac{r_s^{\mathrm{fid}}}{r_s}\right)^3 \frac{1}{\alpha_\perp^2 \alpha_\parallel} P^s(\boldsymbol{k}'[\boldsymbol{k}]). \tag{2.57}$$

Analogously to the configuration space counterpart, the transformation for (k, μ) will be

$$k' = \frac{k}{\alpha_\perp}\left[1 + \mu^2\left(\frac{1}{F} - 1\right)\right]^{1/2}, \tag{2.58}$$

$$\mu' = \frac{\mu}{F}\left[1 + \mu^2\left(\frac{1}{F} - 1\right)\right]^{-1/2}. \tag{2.59}$$

On this account, BAO analyses focus on fitting the theoretical template to the observed two-point statistics by treating the dilation parameters as free parameters—along with other nuisance parameters which are usually marginalised over. Constraining both $\alpha_\parallel$ and $\alpha_\perp$ translate into constraints to $H(z)$ and $D_A(z)$.

2.4 Interlude: The Zeldovich approximation

Before continuing with the remaining aspects of the BAO template, this section will serve to introduce the Lagrangian displacement field, as well as the Zeldovich approximation; both of which will be necessary in order to understand the following two sections. As opposed to Eulerian Perturbation Theory—where the fields of interest are the density contrast and the velocity—Lagrangian Perturbation Theory (LPT) focuses on following the trajectories of particles. Eulerian coordinates $\boldsymbol{r}(t)$ and Lagrangian coordinates $\boldsymbol{q}$ are related by

$$\boldsymbol{r}(t) = \boldsymbol{q} + \boldsymbol{\Psi}(\boldsymbol{q}, t), \tag{2.60}$$

which defines the Lagrangian displacement field $\boldsymbol{\Psi}(\boldsymbol{q}, t)$.

Zeldovich's approach consisted on assuming that the displacement can be separated as

$$\boldsymbol{\Psi}(\boldsymbol{q}, t) = g(t)\boldsymbol{\psi}(\boldsymbol{q}). \tag{2.61}$$

In other words, particles are assumed to keep moving in the same direction at any given time.

By conservation of mass, and assuming the initial density contrast field is sufficiently uniform,

$$\rho(\boldsymbol{r}, t)d^3r = \rho(\boldsymbol{q}, t)d^3q, \tag{2.62}$$

$$\bar{\rho}(t)\left[1 + \delta(\boldsymbol{r}, t)\right]d^3r = \bar{\rho}(t)d^3q, \tag{2.63}$$

which implies

$$\delta(\boldsymbol{r}, t) = J^{-1} - 1, \tag{2.64}$$

with

$$J = \left|\frac{\partial \boldsymbol{r}}{\partial \boldsymbol{q}}\right| = (1 + g(t)\lambda_1)\,(1 + g(t)\lambda_2)\,(1 + g(t)\lambda_3)\,, \tag{2.65}$$

where λ_i are the eigenvalues of the matrix $\partial\boldsymbol{\psi}/\partial\boldsymbol{q}$. From the previous equation, at linear order, the density contrast can be expressed as

$$\delta(\boldsymbol{r}, t) = -g(t)\,(\lambda_1 + \lambda_2 + \lambda_3) = -\nabla_{\boldsymbol{q}} \cdot \boldsymbol{\Psi}(\boldsymbol{q}, t), \tag{2.66}$$

which implies that, in fact, $g(t)$ must be equal to the linear growth factor $D(t)$. Fourier transforming eq. (2.66),

$$\begin{aligned}\delta(\boldsymbol{k}, t) &= -\int d^3r e^{i\boldsymbol{k}\cdot\boldsymbol{r}} \nabla_{\boldsymbol{q}} \cdot \boldsymbol{\Psi}(\boldsymbol{q}, t) \\ &= -\int d^3q J e^{i\boldsymbol{k}\cdot(\boldsymbol{q}+\Psi)} \nabla_{\boldsymbol{q}} \cdot \boldsymbol{\Psi}(\boldsymbol{q}, t) \\ &= -\int d^3q e^{i\boldsymbol{k}\cdot\boldsymbol{q}} \left(\nabla_{\boldsymbol{q}} \cdot \boldsymbol{\Psi}(\boldsymbol{q}, t) + \mathcal{O}(\Psi^2)\right).\end{aligned} \tag{2.67}$$

Thus, at first order

$$\delta(\boldsymbol{k}, t) = -i\boldsymbol{k} \cdot \boldsymbol{\Psi}(\boldsymbol{k}, t). \tag{2.68}$$

If in addition the displacement field is assumed to be longitudinal, then

$$\boldsymbol{\Psi}(\boldsymbol{k}, t) = i\frac{\boldsymbol{k}}{k^2}\delta(\boldsymbol{k}, t). \tag{2.69}$$

Note that this result is compatible with eq. (2.26), since the velocity and the displacement field are related

$$\boldsymbol{v} = a\dot{\boldsymbol{r}} = a\dot{\boldsymbol{\Psi}}. \tag{2.70}$$

2.5 Non-linear degradation of the BAO

While at linear order modes evolve independently, non-linearities become more evident as the gravitational collapse evolves in time. One can think of this as follows: the scale k_{NL} at which the linear power spectrum differs from the non-perturbative power spectrum decreases with time. In particular, bulk flows, mode coupling, and cluster formation degrade the acoustic signature, making it harder to recover the scale information from a galaxy survey. From the Fourier space perspective, the degradation presents as an attenuation of the oscillatory pattern, more precisely in the high harmonics. In configuration space, the effect of the non-linearities is the broadening of the acoustic peak at approximately 100 Mpc/h. This broadening is brought about by the fact that tracers are moved around by ~ 10 Mpc relative to their initial positions as a result of velocity flows and non-linear collapse.

As argued by Eisenstein, Seo, and White 2007, the dominant non-linear effect is the differential motion of pairs of tracers. This section will recapitulate the heuristic approach they followed in order to model this effect. Let us start by assuming that the real-space two-point correlation function can be written as a convolution of the form

$$\xi(\boldsymbol{r}) = \int d^3q_{12} d^3\Psi_{12}\ \xi(\boldsymbol{q}_{12})\mathcal{P}(\boldsymbol{\Psi}_{12}|\boldsymbol{q}_{12})\delta^{(3)}(\boldsymbol{q}_{12} + \boldsymbol{\Psi}_{12} - \boldsymbol{r}), \tag{2.71}$$

where the subscripts 1 and 2 represent different points, $\boldsymbol{q}_{12} = \boldsymbol{q}_1 - \boldsymbol{q}_2$ is the separation in Lagrangian coordinates and $\boldsymbol{\Psi}_{12} = \boldsymbol{\Psi}_1 - \boldsymbol{\Psi}_2$ is the pairwise Lagrangian displacement. Here, $\mathcal{P}(\boldsymbol{\Psi}_{12}|\boldsymbol{q}_{12})$ is the conditional probability distribution function of the displacements, where the implicit assumption has been made that it does not depend on the initial overdensities $\delta(\boldsymbol{q}_1)$, $\delta(\boldsymbol{q}_2)$. This assumption is not the case in reality, as overdense regions tend to move towards each other.

If one assumes the distribution to be Gaussian, then by homogeneity it must have a zero mean, and it should be solely determined by its variance. Furthermore, the variance should be a function of the angle between $\boldsymbol{\Psi}_{12}$ and $\boldsymbol{q}_{12}$. In redshift-space, there is an additional dependence on the angle between $\boldsymbol{\Psi}_{12}$ relative to the line of sight.

Eisenstein, Seo, and White 2007 made use of the N-body simulations presented in Seo and Eisenstein 2005 in order to test this hypothesis. They investigated the distribution of $\boldsymbol{\Psi}_{12}$ for pairs separated by a representative distance of 100 Mpc/h. They found it to be compatible with a Gaussian in the radial and transverse directions (i.e., relative to the initial separation), with a slight skewness towards the infall displacements. They also found the rms value $\langle\Psi^2_{12,\mathrm{transverse}}\rangle^{1/2}$ to be slightly smaller than $\langle\Psi^2_{12,\mathrm{radial}}\rangle^{1/2}$. In redshift space both values are enhanced along the line of sight as a result of the Kaiser effect. They also found them to vary according to the linear growth factor, as expected—recall that according to the Zeldovich approximation $\boldsymbol{\Psi} \propto D(t)$. For example, at $z = 1$, $\langle\Psi^2_{12}\rangle^{1/2} \sim 10$ Mpc/h, with the precise value depending on cosmology.

In order to simplify the treatment, the dependence on the angle relative to the original separations can be neglected. Whereas in redshift space we keep the distinction between displacements along and perpendicular to the line of sight. Hence, the power spectrum should be the product of the

Gaussian damping term and the linear power spectrum:

$$P(k,\mu) = \exp\left[-\frac{k^2\mu^2\sigma_\parallel + k^2(1-\mu^2)\sigma_\perp}{2}\right] P_{\mathrm{lin}}(k), \tag{2.72}$$

where $\sigma_\parallel$ and $\sigma_\perp$ are standard deviation of the displacements along and transverse to the line-of-sight, respectively. Note that $\sigma_\parallel$ is expected to be slightly larger due to linear RSD. In real space, both values should be the same and the angular dependence cancels out.

Given that this approach is phenomenological in nature rather than exact, applying eq. (2.72) directly to the linear power spectrum yields an artificial suppression of power at large wavenumbers. To counterbalance this effect, it is convenient to introduce a *no-wiggle* power spectrum $P_{\mathrm{nw}}(k)$, which is, in essence, a power spectrum without the BAO signal. Taking this definition into account, the former expression can be replaced by

$$\begin{aligned} P(k,\mu) = \exp\left[-\frac{k^2\mu^2\sigma_\parallel + k^2(1-\mu^2)\sigma_\perp}{2}\right] & (P_{\mathrm{lin}}(k) - P_{\mathrm{nw}}(k)) \\ & + P_{\mathrm{nw}}(k), \end{aligned} \tag{2.73}$$

where in this case, the damping only acts on the oscillatory pattern.

It must be noted that a power spectrum without the baryon oscillations is only an implement suited for our present purposes and it holds no real physical significance as it would only be possible for $\Omega_b = 0$, which is not the case in our Universe. A number of methods for constructing $P_{\mathrm{nw}}(k)$ can be found in the literature; the most popular among them is a transfer function fitting formula developed by Eisenstein and Hu 1998. Other implementations include spline fitting (B. A. Reid et al. 2010), polynomial fitting (Hinton et al. 2016) and fast sine transform of the correlation function after removing the peak (Hamann et al. 2010).

It is also worth-noting that the derived damping factor is well in agreement with more sophisticated treatments of infrared resummations under different perturbation theory formalisms (cf. Matsubara 2008; Ivanov and Sibiryakov 2018).

2.6 Reconstruction

In the context of low-redshift galaxy surveys, where non-linear effects are particularly relevant, it becomes important to understand and mitigate these effects. *Reconstruction* refers to a family of methods concerned with ameliorating the acoustic scale measurement by undoing the effects of large-scale displacements. The original idea was developed in Eisenstein, Seo, Sirko, et al. 2007, with later studies under the LPT formalism by Padmanabhan, White, and Cohn 2009. Since then, a number of extensions have been proposed that take into account redshift-space distortions and galaxy/halo bias. Moreover, several independent methods have been suggested, relying on either Eulerian or Lagrangian perturbation theory.

In this text we will focus on LPT reconstruction algorithms, since they are the ones currently being tested within the Mock Challenge project. There are two conventions under which to treat redshift-space-distortions, which we shall discuss in section 2.6.3.

2.6.1 A reconstruction algorithm in real space

In order to gain some insight into how the reconstruction algorithm works, let us consider first how to tackle the problem in real space, leaving RSD and bias corrections for later. This and the next section are strongly based on Padmanabhan, White, and Cohn 2009. A relatively simple reconstruction algorithm comprises the following steps:

- Fourier transform the measured density contrast field $\delta(\boldsymbol{x})$ and filter out high-frequency modes, yielding $S(k)\delta(\boldsymbol{k})$; where $S(k)$ is usually a gaussian filter. Since linear theory is exceptionally valid at large scales, $S(k)\delta(\boldsymbol{k})$ is a reasonable approximation for $\delta_L(\boldsymbol{k})$ for sufficiently small k.

- Define the displacement field, according to the Zeldovich approximation:

$$\boldsymbol{s}(\boldsymbol{k}) = -i\frac{\boldsymbol{k}}{k^2}S(k)\delta(\boldsymbol{k}). \tag{2.74}$$

  As discussed above, this is precisely what we mean by removing large-scale displacements. Note that the minus sign implies that the galaxies will be displaced backwards. The Zeldovich approximation and the smoothed field are consistent only at linear order.

- Displace all the galaxies in the original catalogue by $\boldsymbol{s}$ and recompute the density contrast, obtaining the *displaced* field $\delta_d(\boldsymbol{k})$. As we shall see below, the displaced field contains the short-scale (high-frequency) information of the linear density contrast.

- Create a reference catalogue of randomly (or uniformly) distributed particles, shift their positions by $\boldsymbol{s}$ and compute the density contrast, which we shall define as the *shifted* field $\delta_s(\boldsymbol{k})$. This field comprises the large-scale (low-frequency) information of the linear density contrast.

Following these steps, the reconstructed field is defined as

$$\delta_r(\boldsymbol{k}) = \delta_d(\boldsymbol{k}) - \delta_s(\boldsymbol{k}). \tag{2.75}$$

Contrary to what one might be tempted to conclude, δ_r is *not* the linear density contrast. As we shall discuss in the next section, the sharpening of the peak comes from the fact that δ_r contains a second order correction.

2.6.2 Reconstruction in the light of LPT

Eulerian and Lagrangian coordinates are related by

$$\boldsymbol{r}(t) = \boldsymbol{q} + \boldsymbol{\Psi}(\boldsymbol{q}, t), \tag{2.76}$$

which defines the Lagrangian displacement field $\boldsymbol{\Psi}(\boldsymbol{q}, t)$.

By conservation of mass, and assuming the initial density contrast field is sufficiently uniform,

$$\rho(\boldsymbol{r}, t) d^3 r = \rho(\boldsymbol{q}, t) d^3 q, \tag{2.77}$$

$$\bar{\rho}(t) \left[1 + \delta(\boldsymbol{r}, t)\right] d^3 r = \bar{\rho}(t) d^3 q, \tag{2.78}$$

which is equivalent to

$$\delta(\boldsymbol{r}) = \int d^3 q \delta^{(3)}(\boldsymbol{r} - \boldsymbol{q} - \boldsymbol{\Psi}(\boldsymbol{q})) - 1, \tag{2.79}$$

where time dependence is implicit, a convention we will follow hereafter. In Fourier space,

$$\delta(\boldsymbol{k}) = \int d^3 x e^{-i\boldsymbol{k}\cdot\boldsymbol{x}} \delta(\boldsymbol{x}) = \int d^3 x e^{-i\boldsymbol{k}\cdot\boldsymbol{x}} \left[\int d^3 q \delta^{(3)}(\boldsymbol{x} - \boldsymbol{q} - \boldsymbol{\Psi}(\boldsymbol{q})) - 1\right], \tag{2.80}$$

$$\delta(\boldsymbol{k}) = \int d^3 q e^{-i\boldsymbol{k}\cdot\boldsymbol{q}} \left(e^{-i\boldsymbol{k}\cdot\boldsymbol{\Psi}(\boldsymbol{q})} - 1\right). \tag{2.81}$$

This is the theoretical non-perturbative overdensity field.

Recall that the displaced field is computed once the original particles are displaced by $\boldsymbol{s}$, we can thus formally express it as

$$\delta_d(\boldsymbol{k}) = \int d^3 q e^{-i\boldsymbol{k}\cdot\boldsymbol{q}} \left(e^{-i\boldsymbol{k}\cdot(\boldsymbol{\Psi}(\boldsymbol{q})+\boldsymbol{s})} - 1\right), \tag{2.82}$$

and analogously,

$$\delta_s(\boldsymbol{k}) = \int d^3q e^{-i\boldsymbol{k}\cdot\boldsymbol{q}} \left(e^{-i\boldsymbol{k}\cdot\boldsymbol{s}} - 1\right). \tag{2.83}$$

We can then write

$$\delta_d(\boldsymbol{k}) = (1 - S(k))\delta_L(\boldsymbol{k}) + \mathcal{O}(\delta_L^2), \tag{2.84}$$

$$\delta_s(\boldsymbol{k}) = -S(k)\delta_L(\boldsymbol{k}) + \mathcal{O}(\delta_L^2), \tag{2.85}$$

which confirms that δ_d contains restored small-scale information, whereas δ_s contains restored large-scale information.

2.6.3 Reconstruction algorithms in redshift space

As discussed in Seo, Beutler, et al. 2016, there are two conventions when it comes to treating redshift-space distortions in the reconstruction algorithm. These conventions differ in whether or not they attempt to keep the anisotropic signal, which in turns depends on how the reference catalogue is dealt with. The original BAO reconstruction method (Eisenstein, Seo, Sirko, et al. 2007; Seo, Siegel, et al. 2008; Seo, Eckel, et al. 2010; Mehta et al. 2011) seeks to keep the RSD signal, which we shall refer to as *anisotropic BAO reconstruction*. Whilst the convention by Padmanabhan, White, and Cohn 2009 and Anderson et al. 2014 attempts to remove the RSD signal, which we shall call *isotropic BAO reconstruction*.

Recall that under the Kaiser approximation and assuming linear galaxy bias, we can write

$$\delta^s = b\left(1 + \beta\mu^2\right)\delta_m, \tag{2.86}$$

where δ^s is the redshift-space galaxy overdensity field, whereas δ_m is the real space matter field.

Taking this into consideration, we distinguish between both conventions as follows:

- **Anisotropic BAO reconstruction**: The displacement field in real space is computed from the density field in redshift space, considering bias only:

  $$\boldsymbol{s}(\boldsymbol{k}) = -i\frac{\boldsymbol{k}}{k^2}S(k)\frac{\delta^s(\boldsymbol{k})}{b}. \tag{2.87}$$

  The displacement used for computing the displaced and shifted fields in redshift space is

  $$\boldsymbol{s}^s = \boldsymbol{s} + \frac{f - \beta}{1 + \beta}\left(\boldsymbol{s}\cdot\hat{\boldsymbol{z}}\right)\hat{\boldsymbol{z}}, \quad \text{for } \delta_d, \tag{2.88}$$

$$\boldsymbol{s}^s = \boldsymbol{s} + \frac{f-\beta}{1+\beta}\left(\boldsymbol{s}\cdot\hat{\boldsymbol{z}}\right)\hat{\boldsymbol{z}}, \quad \text{for } \delta_s. \tag{2.89}$$

- **Isotropic BAO reconstruction**: The displacement field in real space is computed from the density field in redshift space, considering bias as well as the Kaiser boost:

  $$\boldsymbol{s}^r(\boldsymbol{k}) = -i\frac{\boldsymbol{k}}{k^2}S(k)\frac{\delta^s(\boldsymbol{k})}{b\left(1+\beta\mu^2\right)}. \tag{2.90}$$

  The displacement used for computing the displaced and shifted fields in redshift space is

  $$\boldsymbol{s}^s = \boldsymbol{s}^r + f\left(\boldsymbol{s}^r\cdot\hat{\boldsymbol{z}}\right)\hat{\boldsymbol{z}}, \quad \text{for } \delta_d, \tag{2.91}$$

  $$\boldsymbol{s}^s = \boldsymbol{s}^r, \quad \text{for } \delta_s. \tag{2.92}$$

2.7 Modelling examples

In this section we will outline how the BAO-fitter implementation was performed in some relevant articles. The main idea is to get a picture of how subtle the choices can be during the analysis. The treatment is instructive rather than exhaustive.

Beutler 2017

Beutler et al. 2017 performed the analysis in Fourier space. They followed the analysis described above, with the template given by

$$P_t(k,\mu) = b^2\mathcal{D}(k\mu\Sigma_s)\left(1+\beta\mu^2 R\right)^2 P_{dw}(k,\mu), \tag{2.93}$$

where the *dewiggled* power spectrum is defined as

$$\begin{aligned} P_{dw}(k,\mu) = \exp\left[-\frac{k^2\mu^2\Sigma_\parallel + k^2(1-\mu^2)\Sigma_\perp}{2}\right]&\left(P_{\text{lin}}(k) - P_{\text{nw}}(k)\right) \\ &+ P_{\text{nw}}(k), \end{aligned} \tag{2.94}$$

which corresponds to eq. (2.73). Note that there is a slight change of notation, uppercase sigmas are used in this case. This convention will be followed hereafter, since lowercase sigmas will be reserved for errors.

They used a Finger of God term of the form

$$D(k\mu\Sigma_s) = \frac{1}{\left(1+k^2\mu^2\Sigma_s^2/2\right)^2}. \tag{2.95}$$

Note that this is similar to eq. (2.32), but the denominator is squared. This is because in this case a Gaussian distribution is assumed in the velocities instead of in the pairwise velocities.

As for the Kaiser term, there is an extra factor R multiplying $\beta\mu^2$. This convention follows that of Seo, Beutler, et al. 2016,

$$R = \begin{cases} 1 & \text{for isotropic reconstruction,} \\ 1 - \exp\left(-k^2\Sigma_{\text{smooth}}^2/2\right) & \text{for anisotropic reconstruction.} \end{cases} \tag{2.96}$$

Recall that in Fourier space, the map between real and fiducial wavenumbers is given by

$$k'_{\parallel} = k_{\parallel}/\alpha_{\parallel}, \tag{2.97}$$

$$k'_{\perp} = k_{\perp}/\alpha_{\perp}, \tag{2.98}$$

which implies

$$k' = \frac{k}{\alpha_{\perp}}\left[1 + \mu^2\left(\frac{\alpha_{\perp}^2}{\alpha_{\parallel}^2} - 1\right)\right]^{1/2}, \tag{2.99}$$

$$\mu' = \frac{\mu\alpha_{\perp}}{\alpha_{\parallel}}\left[1 + \mu^2\left(\frac{\alpha_{\perp}^2}{\alpha_{\parallel}^2} - 1\right)\right]^{-1/2}. \tag{2.100}$$

As opposed to what happens in configuration space, where the correlation function in fiducial coordinates has the same numerical value as the correlation function in real coordinates, in Fourier space the volume element gets rescaled by virtue of the former relations. Thus, the multipoles were calculated as

$$P_{\ell}(k) = \left(\frac{r_s^{\text{fid}}}{r_s}\right)^3 \frac{2\ell + 1}{2\alpha_{\perp}^2\alpha_{\parallel}} \int_{-1}^{1} d\mu P_t[k'(k,\mu), \mu'(\mu)]\mathcal{L}_{\ell}(\mu) + A_{\ell}(k), \tag{2.101}$$

where $A_{\ell}(k)$ accounts for broad-band corrections. The authors distinguished between pre-reconstruction and post-reconstruction data:

$$A_{\ell}^{\text{pre-recon}}(k) = \frac{a_{\ell,1}}{k^3} + \frac{a_{\ell,2}}{k^2} + \frac{a_{\ell,3}}{k} + a_{\ell,4} + a_{\ell,5}k, \tag{2.102}$$

$$A_{\ell}^{\text{post-recon}}(k) = \frac{a_{\ell,1}}{k^3} + \frac{a_{\ell,2}}{k^2} + \frac{a_{\ell,3}}{k} + a_{\ell,4} + a_{\ell,5}k^2. \tag{2.103}$$

The only difference being the fact that for post-reconstructed data, $k \to k^2$ in the last term. The authors claim this choice to optimise convergence, without any further explanation.

Xu 2013

Xu et al. 2013 worked with the dilation and warp parameters, defined as

$$\alpha = \left[\frac{D_A^2(z)}{(D_A^{\mathrm{fid}}(z))^2} \frac{H^{\mathrm{fid}}(z)}{H(z)} \right]^{1/3} \frac{r_s^{\mathrm{fid}}}{r_s} \tag{2.104}$$

$$\epsilon = \left[\frac{H^{\mathrm{fid}}(z)}{H(z)} \frac{D_A^{\mathrm{fid}}(z)}{D_A(z)} \right]^{1/3} - 1, \tag{2.105}$$

respectively. Which, in turn, are related to the alpha parameters through

$$\alpha = \alpha_{\parallel}^{1/3} \alpha_{\perp}^{2/3}, \tag{2.106}$$

$$\epsilon = \left(\frac{\alpha_{\parallel}}{\alpha_{\perp}} \right)^{1/3} - 1. \tag{2.107}$$

They carried out a first order approximation, in order to write the two-point correlation function multipoles in fiducial coordinates in terms of the multipoles in real coordinates and their derivatives:

$$\xi_0(r) = B_0^2 \xi_{0,t}(\alpha r) + \frac{2}{5}\epsilon \left(3\xi_{2,t}(\alpha r) + \frac{d\xi_{2,t}(\alpha r)}{d\log(r)} \right) + A_0(r), \tag{2.108}$$

$$\begin{aligned} \xi_2(r) = 2B_0^2 \epsilon \frac{d\xi_{0,t}(\alpha r)}{d\log(r)} + \left(1 + \frac{6}{7}\epsilon \right) \xi_{2,t}(\alpha r) + \frac{4}{7}\epsilon \frac{d\xi_{2,t}(\alpha r)}{d\log(r)} + \\ \frac{4}{7}\epsilon \left(5\xi_{4,t}(\alpha r) + \frac{d\xi_{4,t}(\alpha r)}{d\log(r)} \right) + A_2(r), \end{aligned} \tag{2.109}$$

where

$$A_\ell = \frac{a_{\ell,1}}{r^2} + \frac{a_{\ell,2}}{r} + a_{\ell,3}. \tag{2.110}$$

Note that this involves having to compute numerical derivatives for every chosen value of α.

In addition, they opted for normalising the measured multipoles by taking 50 Mpc/h as the pivot scale, which forces B_0 to be close to 1. Additionally, note that B_0 allows for a separate treatment of the monopole amplitude, in contrast to the bias parameter b originally introduced above, which multiplies the full power spectrum.

They worked with two sets of data: pre and post-reconstruction. In terms of the fit, the only difference being the treatment of redshift-space distortions. For pre-reconstructed data, the linear Kaiser boost was included, as described above, whereas for post-reconstructed data no prefactor was taken into account.

Ross 2017

A configuration space analysis can be found in Ross et al. 2017, which differs significantly from the approach taken by Xu et al. 2013. In this case, the parametrisation is chosen over $\alpha_{\parallel}$ and $\alpha_{\perp}$. Although one might be tempted to think of it as the configuration space counterpart of the Fourier space analysis from Beutler et al. 2017, it is in fact not the case. The difference comes about from the Alcock-Paczyński effect implementation:

$$\xi_0^{\mathrm{mod}}(s) = B_0\xi_0(s, \alpha_\perp, \alpha_\parallel) + A_0(s), \tag{2.111}$$

$$\xi_2^{\mathrm{mod}}(s) = \frac{5}{2}\left(B_2\xi_{\mu 2}(s, \alpha_\perp, \alpha_\parallel) - B_0\xi_0(s, \alpha_\perp, \alpha_\parallel)\right) + A_2(s), \tag{2.112}$$

with

$$\xi_{\mu 2}(s, \alpha_\perp, \alpha_\parallel) = \int_0^1 d\mu\ 3\mu^2\xi(s', \mu'). \tag{2.113}$$

Note that the essential feature of this choice is the fact that the amplitude of the monopole (in real space coordinates) is allowed to vary independently. In other words, the two terms of the second degree Legendre polynomial $\mathcal{L}_2(\mu) = \frac{1}{2}(3\mu^2 - 1)$ are separated when computing $\xi_2(s)$, thus distinguishing between the contributions from $\xi_0(s)$ and $\xi_{\mu 2}(s)$.

Broad band terms are the same as described in eq. (2.110).

Chapter 3

The DESI Mock Challenge

The work presented in this text was developed within the context of the BAO Mock Challenge of the DESI collaboration. Several tests were run in order to asses the methodology of the BAO method, by making use of clustering measurements coming from mock galaxy catalogues, which are catalogues constructed based upon cosmological simulations. The precise implementation we followed will be described in Chapter 4. The present chapter will serve as an introduction to the Mock Challenge as well as the simulations from which the catalogues employed in the analyses were constructed from.

This chapter is structured as follows. Section 3.1 provides a brief description of the DESI project, followed by an introduction to the Mock Challenge, given in section 3.2. N-body simulations and fast simulations will be discussed in 3.3, giving particular attention to UNIT and EZmock mock catalogues. Finally, section 3.4 presents a preamble to the tests described in the following chapter.

3.1 The DESI experiment

The Dark Energy Spectroscopic Instrument (DESI) is installed in the Nicholas U. Mayall 4-meter telescope located in Arizona as part of the Kitt Peak National Observatory, and it consists of 5000 robotic positioners containing an optical fibre each, which together feed a set of 10 spectrographs. By gathering the light of more than 30 million preselected tracers, over a wavelength range from 359 nm to 980 nm (i.e., all the visible spectrum plus part of the near-infrared) and covering an area in the sky of around $14,000\ \text{deg}^2$, the DESI experiment is expected to yield the largest and most comprehensive map of the Universe ever created (DESI Collaboration 2016). The main goal of the DESI collaboration is to measure the BAO signal to a subpercent level, which will permit a better understanding of the nature of Dark Energy. Additionally, measuring the growth of structure via RSD will provide an opportunity to test the validity of General Relativity at large scales.

Achieving the goals of DESI is a collaborative effort, with scientists from more than 60 institutions from 13 countries working together. It is primarily funded by the Science Office of the US Department of Energy (DOE) and managed by the Lawrence Berkeley National Laboratory (Berkeley Lab). In particular, the Instituto de Física, UNAM forms part of the Mexico Regional Participation Group, supported by the National Council of Science and Technology (CONACYT).

The main survey began in May 17th 2021; with more than 12.8 million redshifts measured one year later. The four primary targets are:

i) Luminous Red Galaxies (LRGs) up to $z = 1.0$. LRGs are massive elliptical galaxies with featureless spectra. The redshift is measured from the position of the 4000 Å break.

ii) Emission Line Galaxies (ELGs) up to $z = 1.7$. This type of galaxies are spiral or irregular star-forming galaxies. The redshift is measured from the $[OII]$ line. They correspond to the largest sample of tracers observed by DESI.

iii) Quasars, also known as quasi-stellar objects (QSOs), up to $z = 2.1$ as direct tracers of the underlying matter density. Quasars are extremely luminous sources asocciated with active galactic nuclei (AGN).

iv) QSOs as tracers of the distribution of neutral hydrogen via the Lyman-α forest, between $2.1 < z < 3.5$.

In addition, when moon conditions do not allow for observing the main targets listed above, a magnitude-limited bright galaxy survey (BGS) is being conducted with an effective redshift $z \approx 2$; as well as a survey of Milky Way stars.

DESI will build on previous work by its predecessors, namely the Baryon Oscillation Spectroscopic Survey (BOSS) (Dawson et al. 2013), part of the Sloan Digital Sky Survey (SDSS) III project, as well as the SDSS-IV extended BOSS (eBOSS) (Alam, Aubert, et al. 2021). By studying the BAO, constraints will be placed to the expansion history of the universe, which in turn can be used as a probe of the Dark Energy equation of state. Moreover, DESI will allow for additional scientific objectives, such as measuring the sum of neutrino masses along with constraining modified gravity models and theories of inflation. The DESI experiment is classified as a Stage-IV experiment, according to the requirements stated by the Dark Energy Task Force (Albrecht et al. 2006)

3.2 The BAO Mock Challenge

The Mock Challenge (MC) project started operations in 2019 (Chuang, Vargas-Magaña, and Alam 2020) with the main goal of constructing the cosmological analysis pipeline that will ultimately be used by the DESI collaboration. In order to test and validate the pipeline several mock galaxy catalogues are being used. To satisfy the precision requirements for the cosmological constraints and build a robust, efficient, and optimised pipeline, codes from different groups are being collected and depurated.

Mock catalogues coming from simulations have been (or will be) prepared for the various DESI tracers. In general, two types of simulations will be distinguished: (i) high resolution N-body simulations, which include UNIT, AbacusSummit, SLICS, and Planck Millennium simulations; and (ii) fast simulations, such as EZmocks, BAM, and FastPM.

MC development has been planned considering different stages with the aim of increasing how realistic the catalogues are with every stage. The first stage consisted of using small cubic-box catalogues, with a side length of 1 Gpc/h. This was followed by a second stage, the subject of this text, utilising large cubic boxes, of 3 Gpc/h. The third stage will consist of considering the mask of the survey: cubic boxes corresponding to a given redshift are repeated and then cut out considering the survey geometry; these are referred to as *cut-sky* mocks. Subsequently, the pipeline will be tested with *light-cone* mocks, which are constructed similarly to cut-sky mocks, but considering redshift evolution. Basically, shells from cut-sky mocks at the different redshifts are put together. In the fourth and final stage, observational systematics will be added.

The pipeline testing comprises several components:

- Validation of different codes for computing the 2-point statistics from the data: power spectrum, correlation function, cross-power spectrum, cross-correlation function.

- Comparison of different methods for constructing covariance matrices to associate to the clustering measurements, such as: analytical methods, jackknife computation, making use of high resolution or fast simulations.

- Comparison of different reconstruction codes and algorithms.
- Cross-validation of codes from different groups to fit the theoretical template for BAO measurements, which we shall refer to as the BAO fitter.
- Cross-validation of codes from different groups to fit the theoretical template for the RSD measurements.

The work addressed in this text corresponds a specific part of the post-reconstruction BAO pipeline, the BAO fitter, shown in Fig. 3.1. Our implementation of the BAO fitter was also tested along with those of other MC participants.

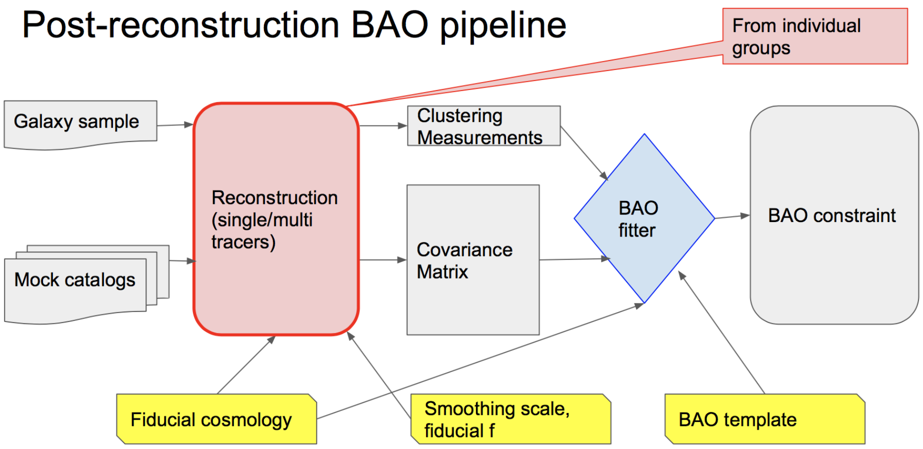

Figure 3.1: Flowchart of the BAO pipeline. Taken from Chuang, Vargas-Magaña, and Alam 2020.

3.3 Mock Catalogues

Galaxy mock catalogues can be produced from either N-body simulations or fast simulations. N-body are more accurate but require greater computational time and resources. Fast simulations are appropriately named as they quickly produce the catalogue but at the expense of accuracy.

In this section, a brief account of how this is done is given. In subsection 3.3.1, a generic algorithm for N-body simulations is described. In subsection

3.3.2, the UNIT N-body simulations are introduced. They are of particular interest in this work, as the galaxy catalogues used for the tests presented in Ch. 4 come from the these simulations. A particular instance of fast simulations, namely the EZmocks method, is presented in subsection 3.3.3. These simulations where employed to produce the covariance matrices made used of in the analysis herein considered.

In the case of N-body simulations, the raw output is the dark matter density field at a given time, as described in section 3.3.1. Given this dark matter density field, the next issue is how to populate the underlying density field with points representing galaxies. Usually, the first step consists in identifying dark matter halos. Halos are gravitationally bound structures, where galaxies are known to reside. Given a density field, halos can be determined by identifying which dark matter particles are bound together as they are bound if their velocity is not sufficiently high to overcome the gravitational potential. This can be done with algorithms such as the *friends-of-friends algorithm* or the *spherical overdensity algorithm.* At this point a halo catalogue is obtained. The following step is to relate each halo with a galaxy population. The galaxy distribution is biased with respect to the halo distribution, since galaxy formation requires non-gravitational interactions. One approach to address this is using a *halo occupation distribution* (HOD) model, in which a probability distribution $\mathcal{P}(N_g|M_h)$ is assumed for finding N_g galaxies in halo of mass M_h. This probability usually includes many free parameters, that are to be calibrated in order to match the desired statistics of a given population of tracers (for example, the ELG, LRG or QSO samples of the DESI survey).

In contrast, fast simulations are aimed at reproducing the clustering measurements of N-body simulations in a significantly shorter amount of time, although at expense of accuracy at small scales and/or physical insight of the associated distribution. Furthermore, they generate tracer catalogues directly, instead of going through the process discussed above.

3.3.1 N-body simulations in a nutshell

N-body simulations focus on the gravity-induced time evolution of phase-space elements of the dark matter distribution. Those phase-space elements are commonly referred to as *dark matter particles*, although they do not represent actual physical particles. Cubic boxes are generally used, imposing periodic boundary conditions (i.e., if a particle moves out of the box from one side it must reenter the box on the opposite side). The resolution of a simulation depends on the number of particles within the box. Given a value for Ω_m and the box volume, the total mass within the box is distributed among all particles, thus the particle mass quantifies the resolution—the lower the mass, the higher the resolution.

Recall that for cold, collisionless dark matter, the geodesic equations take a Newtonian form:

$$\dot{\boldsymbol{r}} = \frac{\boldsymbol{p}}{am}, \tag{3.1}$$

$$\dot{\boldsymbol{p}} = -H\boldsymbol{p} - \frac{m}{a}\nabla\Phi, \tag{3.2}$$

where Φ is the gravitational potential. The scale factor $a(t)$ appears as a consequence of the fact that we are using comoving coordinates. The term proportional to H represents the drag due to the expanding background. These equations are supplemented by the Poisson equation,

$$\nabla^2\Phi = 4\pi G a \bar{\rho}_m \delta_m. \tag{3.3}$$

The idea is to follow the evolution of $\boldsymbol{r}(t)$ and $\boldsymbol{p}(t)$ for each particle by updating their values at different snapshots of time.

The first aspect to take into account is the initial conditions. N-body simulations are initiated at sufficiently early times during the matter-dominated era, where the effects of non-linearities are negligible at most scales. In this fashion, Gaussian initial conditions are commonly used. The variance of the amplitude of the Fourier modes $\delta_m(\boldsymbol{k})$ is given directly from the linear power spectrum $P_{\text{lin}}(k)$ obtained from a Boltzmann code for a given set of cosmological parameters.

Now let us describe how the system of equations is solved at every step of time t_i. First, the Poisson equation is solved at the position of each particle. In other words, the gravitational force applied on each particle by to the rest of the particles is calculated. The simplest algorithm is the Particle-Particle (PP) method, which consists in directly summing pairwise forces. It has the disadvantage of been very CPU-time consuming as it scales as $\mathcal{O}(N^2)$, where N is the total number of particles. Another alternative is the Particle-Mesh (PM) method (e.g., Hockney and Eastwood 1988), in which the cubic box is divided into a grid, the density contrast in each grid cell is computed and then a Fast Fourier Transform (FFT) is applied, so that the Poisson equation can be solved for Φ directly in Fourier space

$$\Phi(\boldsymbol{k}, t_i) = -k^2 4\pi G a \bar{\rho}_m \delta_m(\boldsymbol{k}). \tag{3.4}$$

Subsequently, Φ is transformed back into configuration space, where it is interpolated into the positions of the different particles. This method scales as $\mathcal{O}(N) + \mathcal{O}(N_g \log N_g)$, where N_g is the total number of grid cells. Moreover, since the force obtained from the PM algorithm depends on the grid size, it can be supplemented with the force from nearby particles calculated directly with the PP method; this hybrid algorithm is known as P^{3}M (e.g., Efstathiou et al. 1985). An alternative and popular approach is the tree algorithm (e.g., Barnes and Hut 1986), which divides space recursively into a hierarchy of cells; for cells sufficiently small and far apart from the point of interest, the particles inside are treated as a single particle located at the centre of mass. This method scales as $\mathcal{O}(N \log N)$.

Once the gravitational potential is known, the equations for the positions and momenta are solved with a time integrator. The most popular among them is the *leapfrog* integrator, which we shall describe briefly. But before going into detail, let us note that the system of equations can be simplified if we define $\boldsymbol{p}_c = a\boldsymbol{p}$ (Dodelson and Schmidt 2021), yielding

$$\dot{\boldsymbol{r}} = \frac{\boldsymbol{p}_c}{a^2 m}, \tag{3.5}$$

$$\dot{\boldsymbol{p}}_c = -m\nabla\Phi. \tag{3.6}$$

In the leapfrog algorithm, positions and momenta are evaluated at slightly different times $\boldsymbol{r}(t_i)$, $\boldsymbol{p}_c(t_i - \Delta t/2)$, where Δt is the time step. Thus, by means of eqs. (3.5) and (3.6), the position and momentum of the jth particle at time $t_{i+1} = t_i + \Delta t$ is updated as

$$\boldsymbol{p}_c^{(j)}(t_{i+1} - \Delta t/2) = \boldsymbol{p}_c^{(j)}(t_i - \Delta t/2) - m\nabla\Phi(\boldsymbol{r}^{(j)}(t_i))\Delta t \tag{3.7}$$

$$\boldsymbol{r}^{(j)}(t_{i+1}) = \boldsymbol{r}^{(j)}(t_i) + \frac{\boldsymbol{p}_c^{(j)}(t_{i+1} - \Delta t/2)}{a^2(t_{i+1} - \Delta t/2)m}\Delta t. \tag{3.8}$$

The algorithm is iterated until the desired time t is reached.

3.3.2 UNIT simulations

The N-body simulations from the UNIT project (Chuang, Yepes, et al. 2019) were constructed following the variance suppression method proposed by Angulo and Pontzen 2016, which consists of pairing simulations with initial Fourier modes out of phase, while fixing their amplitude to that of the ensemble-averaged power spectrum. This method has been proven to significantly reduce the variance, without introducing bias to the 2-point statistics measurements.

The UNIT team used a non-public version of the N-body simulation code GADGET (Springel 2005) in order to produce a paired couple of

1 $(h^{-1}\text{Gpc})^3$ boxes. The pair of boxes contain 40963^3 particles each, with a particle mass of $\sim 1.2 \times 10^9\ h^{-1}\text{M}_\odot$. They also generated larger boxes, with side lengths of 2 h^{-1}Gpc and 3 h^{-1}Gpc, but lower resolution $\sim 10^{10}\ h^{-1}\text{M}_\odot$. The paired initial conditions where generated with FastPM (Feng et al. 2016), which makes use of second order Lagrangian perturbation theory. The cosmological parameters for this simulations are: $\Omega_m = 0.3089$, $h = 0.6774$, $n_s = 0.9667$ and $\sigma_8 = 0.8147$ (from Planck Collaboration, Ade, et al. 2016), where n_s is the scalar spectral index and σ_8 is the variance of the the smoothed matter density field with a smoothing scale of $8\,h^{-1}$Mpc . Dark matter halos were identified with the Rockstar code (Behroozi, Wechsler, and Wu 2013).

3.3.3 EZmocks

N-body simulations have the disadvantage of being highly resource consuming. When studying the large-scale structure of the universe and especially in the context of large galaxy surveys, it is imperative to have access to hundreds or even thousands of simulations. Producing such a number of full N-body simulations in a reasonable time is not feasible even with the current high-end computational resources available. On this account, several methods have been developed in order to produce reliable *fast* simulations that reproduce 2-point or even 3-point statistics of the N-body simulations to acceptable accuracy.

Chuang, Kitaura, et al. 2015 introduced a novel methodology to generate mock halo/galaxy catalogues, which they called *effective Zeldovich* mock catalogues (EZmocks). The procedure is based upon the Zeldovich approximation (cf. 2.4) and incorporates a practical description of stochastic scale-dependent, non-local and non-linear biasing. This effective bias model allows for directly generating tracer catalogues from the dark matter density field, as opposed to the regular approach followed with N-body simulations, which consists in using a halo finder algorithm in order to generate the halo catalogue and then populating those halos with galaxies by making use of an Halo Occupation Distribution (HOD) model.

The EZmock method was revised in Zhao et al. 2021, in this subsection we shall follow the description therein presented. The algorithm starts by generating the initial density contrast $\delta_m(\boldsymbol{q})$ in Fourier space from a Gaussian realisation with variance equal to a given linear power spectrum, and random phases. The displacement field in Fourier space is then generated according to the Zeldovich approximation (eq. 2.69), and then a inverse Fast Fourier Transform (FFT) is applied in order to obtain the displacements in configuration space. The dark matter particles are displaced accordingly and the density field $\rho_m(\boldsymbol{r}, t)$ is computed using the Cloud-in-Cell assignment scheme.

So far, the method is equivalent to a single-step N-body algorithm. The next step comprises the population of the box with tracers via the biasing model. The tracer density ρ_t is modelled as (Baumgarten and Chuang 2018)

$$\rho_t = \theta(\rho_m - \rho_c)\rho_{\text{sat}}\left[1 - \exp(-\rho_m/\rho_{\text{exp}})\right] B_s, \tag{3.9}$$

where θ is the Heaviside step function

$$\theta(x) = \begin{cases} 0, & x < 0, \\ 1, & x \geq 0, \end{cases} \tag{3.10}$$

with ρ_c, ρ_{sat} and ρ_{exp} as free parameters. The parameter ρ_c represents a critical density as for bound systems to form, a minimal density is required in order to overcome the background expansion. The quantity ρ_{sat} is a saturation density, meaning that above this density every value of ρ_m should be treated equivalently. Whereas ρ_{exp} introduces an exponential cut-off.

The factor B_s in eq. (3.9) accounts for the stochasticity of tracers and it is given by

$$B_s = \begin{cases} 1 + G(\lambda), & G(\lambda) \geq 0, \\ \exp(G(\lambda)), & G(\lambda) < 0, \end{cases} \tag{3.11}$$

where $G(\lambda)$ is a random number coming from a Gaussian realisation with mean equal to zero and standard deviation equal to λ.

The probability distribution function of the tracers is modelled as a power law

$$\mathcal{P}(n_t) = Ab^{n_t}, \tag{3.12}$$

where n_t is the number of tracers per grid cell. The normalisation factor A is determined by the total number of tracers, since it is one of the input parameters, whereas b is a free parameter with the condition $0 < b < 1$.

The number of cells $n_c(n_t)$ with exactly n_t tracers will be given by

$$n_c(n_t) = \lfloor N_c \mathcal{P}(n_t) \rceil, \tag{3.13}$$

where N_c is the total number of tracers and $\lfloor \cdot \rceil$ is the round-up to the nearest integer operator. Note that since $\mathcal{P}(n_t)$ is a monotonically decreasing function, then the maximum number of particles that a cell could contain would be

$$n_{t,\max} = \min\left\{n_t | N_c P(n_t) < 0.5\right\}. \tag{3.14}$$

In order to map n_c to the analytical density in eq. (3.9), the cells are ranked by their ρ_t value. In this way, the first $n_c(n_{t,\max})$ with the largest density are assigned $n_{t,\max}$ tracers, the following $n_c(n_{t,\max} - 1)$ cells are assigned $n_{t,\max} - 1$ tracers and so on. The tracers are finally assigned randomly to the positions of the dark matter particles.

In addition to the bias model discussed above, the EZmock method also takes into account the non-linear random motion of tracers with respect to the dark matter velocity field. This effect will only modify redshift-space measurements. Recall that according to eq. (2.70), the peculiar velocity can be written in terms of the Zeldovich displacement field as

$$\boldsymbol{v} = a\dot{\boldsymbol{\Psi}} = aHf\boldsymbol{\Psi}, \tag{3.15}$$

since $\boldsymbol{\Psi} \propto D(t)$. Then, velocities of the tracers are modelled as

$$\boldsymbol{v}_t = aHf\boldsymbol{\Psi} + \boldsymbol{G}(\nu), \tag{3.16}$$

where $\boldsymbol{G}(\nu)$ is drawn from an isotropic three-dimensional Gaussian distribution, centred at zero with width ν. Note that this term is related to the Finger-of-God effect discussed in section 2.1.2.

Parameter	Description	Effect on clustering measurements
b	PDF base	Tunes small-scale clustering.
λ	Stochasticity	Modifies bias almost linearly.
ν	Random motion	Adjusts the quadrupole at small scales.
δ_c	Density cut	Tweaks bispectrum.

Table 3.1: Free parameters of the EZmock methodology; specifically the version corresponding to the pyEZmock wrapper.

All of the parameters introduced above are in principle free, but since some of them are degenerate, Zhao et al. 2021 decided to fix $\rho_{\text{sat}} = 10$ and $\lambda = 10$. However, the EZmocks for the Mock Challenge were generated following the python wrapper of the EZmock code, *pyEZmock* [1]. In this code, the fixed parameters are $\rho_{\text{sat}} = 100$ and $\rho_{\text{exp}} = 0$. This python wrapper allows for measuring the two-point correlation function, power spectrum and bispectrum of the EZmocks in order to compare and thus calibrate with a given reference. The fine tuning of the parameters has to be done manually. Once a suitable set of parameters is found, it has to be validated by producing a couple of dozens of EZmocks with different random seeds to

---

[1] `https://github.com/cheng-zhao/pyEZmock` developed by Cheng Zhao.

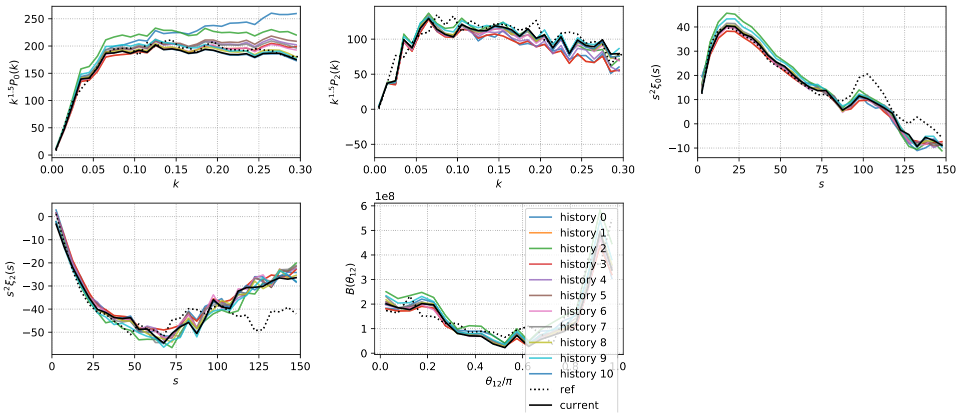

Figure 3.2: Calibration of the EZmocks parameters with a given reference.

account for cosmic variance. The wrapper also has a convenient feature for mass production of EZmocks after the callibration has been done. In Table 3.1 the four free parameters are listed along with their effective impact on the clustering measurements. In the GitHub repository for pyEZmock, a *cheatsheet* can be found that shows a visual representation of how varying the parameters affects the clustering. Figure 3.2 is an example of how the calibration works. It involves deciding the best parameters "by eye" by recomputing the EZmock catalogue at every step during the tuning process. The clustering measurements in the figure are shown for illustrative purposes only and do not correspond to the EZmocks used for the covariance matrices discussed in this work. Incidentally, our group at UNAM was involved in the mass production of thousands of EZmocks calibrated with the Survey Validation 3 (SV3) data of the DESI collaboration.

3.4 Stage 2 BAO MC

In Stage 2 of the BAO Mock Challenge, several groups where asked to perform BAO fits with their own implementation of the BAO fitter following the model by Beutler et al. 2017. The fits were done on the clustering measurements from two sets of post-reconstruction ELG mock catalogues corresponding to a UNIT cubic box of 3 Gpc/h at $z = 0.9873$. Each post-reconstruction set of mocks corresponding to one of the two reconstruction conventions (isotropic and anisotropic) with different smoothing scales:

5 Mpc/h, 10 Mpc/h and 15 Mpc/h. The original pre-reconstruction ELG mock catalogue was previously prepared by the Cosmological Simulations Working Group (CosmoSims WG), using the HOD model from Alam, John A Peacock, et al. 2020.

The covariance matrices for the power spectrum and correlation function were prepared by rescaling the covariance matrices previously used in Stage 1 of the Mock Challenge, where mock catalogues of 1 Gpc/h were used (i.e., $C \to \frac{(1\ \mathrm{Gpc}/h)^3}{(3\ \mathrm{Gpc}/h)^3} C = \frac{1}{27} C$.) In order to calculate the original covariance matrices, two sets of 1000 EZmocks were produced by the CosmoSims WG. The first set consisted of EZmocks to which the same amplitude suppression technique described in 3.3.2 was applied (fixed amplitude covariance), while the second set consisted of regular EZmocks (non-fixed amplitude covariance). In each set, covariance matrices were calculated post-reconstruction following the two different conventions. For fixed amplitude, only the covariances for the post-reconstruction EZmocks with a smoothing of 15 Mpc/h were made available, whereas for non-fixed amplitude, covariances were prepared for all of the smoothing cases; however, for the official Stage 2 tasks, only covariances for $\Sigma_{\mathrm{smooth}} = 15\,\mathrm{Mpc}/h$ were used. Figure 3.3 displays the correlation matrices for the different types of reconstruction with both the fixed amplitude method and the standard method (non-fixed amplitude). Recall that the correlation matrix is defined as

$$\rho_{ij} = \frac{\sigma_{ij}}{\sqrt{\sigma_{ii}\sigma_{jj}}}, \tag{3.17}$$

where σ is the covariance matrix. Correlation matrices are preferred when it comes to plotting, since the normalisation allows for a better comparison—recall that $-1 \leq \rho_{ij} \leq 1$.

Each participant was requested to report the obtained values for the dilation parameters as well as their respective error ($\alpha_{\parallel}$, $\alpha_{\perp}$, $\sigma_{\alpha_{\parallel}}$, $\sigma_{\alpha_{\perp}}$). By using a linear power spectrum with the same cosmological parameters as the UNIT simulations (Planck Collaboration, Ade, et al. 2016), an unbiased fitter should be consistent with $\alpha_{\parallel} = \alpha_{\perp} = 1$. The aim of Stage 2, and of this work, was to test how sensitive the BAO fitter can be in terms of the smoothing scale, reconstruction convention, and fit range. The methodology and results from our fitter will be discussed in the next chapter. In addition to the official tests required for the BAO MC, three additional tests are included in this work.

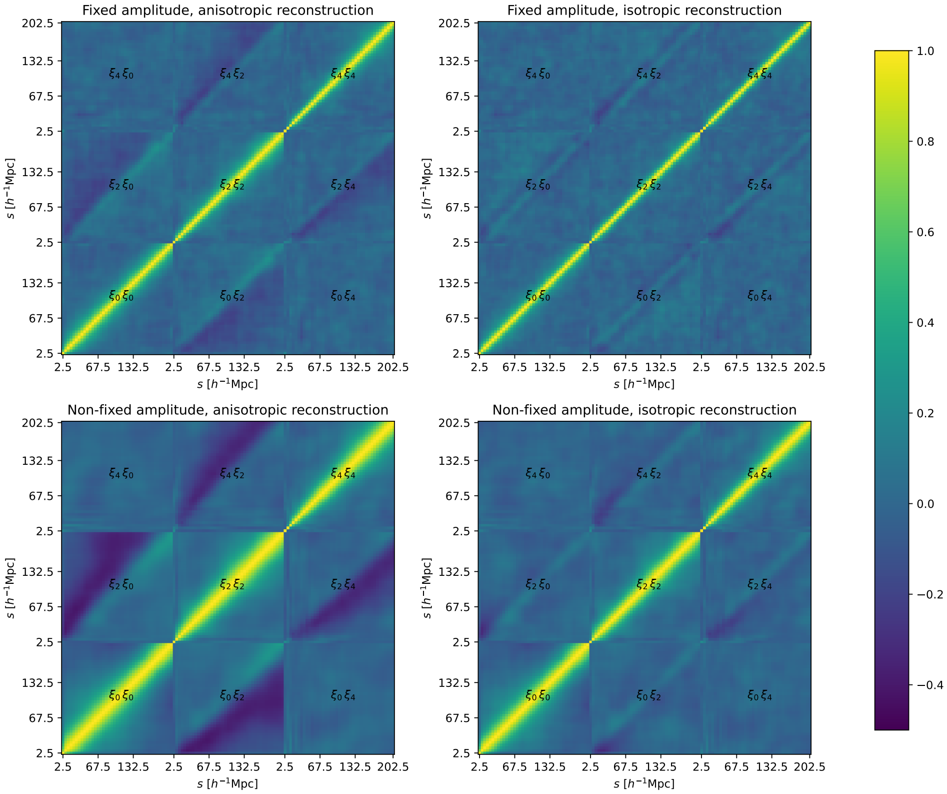

Figure 3.3: Correlation matrices calculated from the post-reconstruction EZmocks with $\Sigma_{\mathrm{smooth}} = 15\,\mathrm{Mpc}/h$.

Chapter 4

BAO tests, analysis and results

The BAO tests performed with our implementation of the BAO fitter will be presented in this chapter.

4.1 Implementation of the BAO fitter

We used the template from Beutler et al. 2017 for the power spectrum:

$$P_t(k,\mu) = b^2\mathcal{D}(k\mu\Sigma_s)\left(1+\beta\mu^2 R\right)^2 P_{dw}(k,\mu) \tag{4.1}$$

with the *dewiggled* power spectrum given by

$$\begin{aligned} P_{dw}(k,\mu) = \exp\left[-\frac{k^2\mu^2\Sigma_{\parallel} + k^2(1-\mu^2)\Sigma_{\perp}}{2}\right]&(P_{\text{lin}}(k) - P_{\text{nw}}(k)) \\ &+ P_{\text{nw}}(k), \end{aligned} \tag{4.2}$$

where the linear power spectrum $P_{\text{lin}}(k)$ was generated with CAMB (Lewis, Challinor, and Lasenby 2000) making use of the cosmological parameters from Planck Collaboration, Ade, et al. 2016 (in consistency with the UNIT simulations) , while the no-wiggle power spectrum $P_{\text{nw}}(k)$ was constructed using the polynomial fitting approach introduced by Hinton et al. 2016. The dispersion term accounting for the finger of God effect is

$$D(k\mu\Sigma_s) = \frac{1}{\left(1+k^2\mu^2\Sigma_s^2/2\right)^2}; \tag{4.3}$$

and recall that

$$R = \begin{cases} 1 & \text{for isotropic reconstruction,} \\ 1 - \exp\left(-k^2\Sigma^2_{\text{smooth}}/2\right) & \text{for anisotropic reconstruction.} \end{cases} \tag{4.4}$$

As our fitter works in configuration space, the multipoles from the template (eq. 4.1) were transformed into multipoles of the 2-point correlation function by means of eq. 2.13. Formally, the multipoles from the data $\xi_{\ell,d}(s)$ were fitted to the template as

$$\xi_{\ell,d}(s) = \frac{2\ell+1}{2}\int_{-1}^{1} d\mu\ \xi_t(s'[s,\mu],\mu'[s,\mu])\mathcal{L}_\ell(\mu), \tag{4.5}$$

where (s,μ) are the fiducial coordinates, while the prime coordinates (s',μ') are the real coordinates, with the transformation given by eqs. (2.49) and (2.50), namely

$$s'[s,\mu] = \alpha_\perp s\left[1+\mu^2\left(F^2-1\right)\right]^{1/2}, \tag{4.6}$$

$$\mu'[s,\mu] = F\mu\left[1+\mu^2\left(F^2-1\right)\right]^{-1/2}, \tag{4.7}$$

where $F = \alpha_\parallel/\alpha_\perp$.

In practice, we constructed the correlation function in 2D by interpolating the first three non-zero multipoles from the template (monopole, quadrupole and hexadecapole) to the real coordinates and adding their contributions together:

$$\xi_t(s',\mu') = \sum_{\ell=0}^{\infty}\xi_{\ell,t}(s')\mathcal{L}_\ell(\mu') \approx \sum_{\ell=0}^{4}\xi_{\ell,t}(s')\mathcal{L}_\ell(\mu'). \tag{4.8}$$

As we were mainly interested in fitting monopole and quadrupole from the data, note that in theory the approximation in this equation should be sufficiently accurate. Furthermore, contributions from $\ell > 4$ are so minimal, that they have rarely been used in the literature. Additionally, recall that at linear order, the only non-zero multipoles due to the Kaiser boost are monopole, quadrupole and hexadecapole.

In order to account for broad-band shape discrepancies due to non-linear bias or poorly modelled redshift-space distortions, three polynomial terms per mulitpole were included as

$$\xi_{0,d}(s) = \frac{2\ell+1}{2}\int_{-1}^{1} d\mu\ \xi_t(s'[s,\mu],\mu'[s,\mu]) + A_0(s), \tag{4.9}$$

$$\xi_{2,d}(s) = \frac{2\ell+1}{2}\int_{-1}^{1} d\mu\ \xi_t(s'[s,\mu],\mu'[s,\mu])\mathcal{L}_2(\mu) + A_2(s), \tag{4.10}$$

with

$$A_\ell(s) = \frac{a_{\ell,1}}{s^2} + \frac{a_{\ell,2}}{s} + a_{\ell,3}, \tag{4.11}$$

analogously to Xu et al. 2013.

Thus, our implementation includes 13 parameters in total: $\alpha_\parallel$, $\alpha_\perp$, b, β, $\Sigma_\parallel$, $\Sigma_\perp$, Σ_s , $\{a_{0,i}\}_{i=1}^3$ and $\{a_{2,i}\}_{i=1}^3$. The two parameters of interest are $\alpha_\parallel$ and $\alpha_\perp$, for which the best-fit values are to be found. The rest of the parameters are treated as nuisance parameters, to be marginalised over. In particular, analytical marginalisation was performed on the broad-band coefficients as described in section 4.3, and hence strictly speaking they do not count as free parameters.

4.2 A brief overview on parameter inference

Bayesian statistics is the preferred tool to make parameter inferences in modern cosmology. It is based on the premise that probabilities can be updated in the light of new information available. Given a model characterised by a set of parameters $\boldsymbol{\theta} = (\theta_1, \ldots, \theta_n)$, and a measured data vector $\boldsymbol{d} = (d_1, \ldots, d_m)$, we would like to determine the probability distribution of the parameters given the data $\mathcal{P}(\boldsymbol{\theta}|\boldsymbol{d})$, in order to find the preferred values for the model. Bayes theorem states that

$$\mathcal{P}(\boldsymbol{\theta}|\boldsymbol{d}) = \frac{\mathcal{P}(\boldsymbol{d}|\boldsymbol{\theta})\mathcal{P}(\boldsymbol{\theta})}{\mathcal{P}(\boldsymbol{d})}, \tag{4.12}$$

where $\mathcal{P}(\boldsymbol{\theta})$ is referred to as the *prior*, $\mathcal{P}(\boldsymbol{d}|\boldsymbol{\theta})$ is the *likelihood* and $\mathcal{P}(\boldsymbol{d})$ is known as the *evidence*. Hence, the *posterior* $\mathcal{P}(\boldsymbol{\theta}|\boldsymbol{d})$ is essentially the updated probability.

The likelihood is the probability of the data given a set of parameters, and it is often denoted as

$$\mathcal{L}(\boldsymbol{\theta}|\boldsymbol{d}) \equiv \mathcal{P}(\boldsymbol{d}|\boldsymbol{\theta}). \tag{4.13}$$

Note that it is a PDF in $\boldsymbol{d}$, but not in $\boldsymbol{\theta}$.

In general, the model will include parameters of interest which are aimed to be constrained, as well nuisance parameters, whose probabilities do not provide any insight into the model. Let us say that in this case, θ_1, θ_2, are the parameters of interest. Their probability density, can be obtained by marginalising over the rest of the parameters:

$$\mathcal{P}(\theta_1, \theta_2|\boldsymbol{d}) = \int \mathcal{P}(\boldsymbol{\theta}|\boldsymbol{d}) d\theta_3 \cdots d\theta_n. \tag{4.14}$$

Now, let us come back to how the posterior is to be determined. Suppose that there are reasons to believe, either from previous measurements or theoretical arguments, that the parameters should be constrained between certain values or centred at a specific value. In that case, the prior can be chosen to be flat within a given boundary or Gaussian. Additionally, for the purposes of parameter inference, the evidence will act merely as a normalisation factor. Therefore, the central role in the analysis will be played by the likelihood function.

Under the assumption of Gaussianly-distributed data, the likelihood is given by a multi-variate Gaussian:

$$\mathcal{L}(\boldsymbol{\theta}|\boldsymbol{d}) = \frac{1}{(2\pi)^{m/2} \left|\det C\right|^{1/2}} \exp\left[-\frac{1}{2}\sum_{ij}(\boldsymbol{d}-\boldsymbol{y})_i C^{-1}_{ij}(\boldsymbol{d}-\boldsymbol{y})_j\right], \tag{4.15}$$

here $\boldsymbol{y}$ is the theoretical data vector predicted by the model and therefore depends on $\boldsymbol{\theta}$, while C is the covariance matrix, defined as

$$C_{ij} = \langle(\boldsymbol{d}-\boldsymbol{y})_i(\boldsymbol{d}-\boldsymbol{y})_j\rangle. \tag{4.16}$$

The argument of the exponential in eq. (4.15) is proportional to the quantity

$$\chi^2 = \sum_{ij}(\boldsymbol{d}-\boldsymbol{y})_i C^{-1}_{ij}(\boldsymbol{d}-\boldsymbol{y})_j, \tag{4.17}$$

which will in fact follow a χ^2 (chi squared) distribution if the data is Gaussianly distributed. In the case of a flat prior, for instance, finding the best-fit values by maximising the posterior is equivalent to maximising the likelihood, which in turn will be equivalent to minimising the chi squared.

Despite the fact that the likelihood is Gaussian in the data, it is in general not Gaussian in the parameters $\boldsymbol{\theta}$, since both $\boldsymbol{y}$ and C might depend on the model in a non-trivial way.

One way to sample the posterior distribution is with the help of a Markov Chain Monte Carlo (MCMC) method. The aim of an MCMC algorithm is to yield a sequence of points in the parameter space $\{\boldsymbol{\theta}^{(1)}, ..., \boldsymbol{\theta}^{(N)}\}$ with a number density that is asymptotically proportional to the *target* probability density—the posterior in this case. The sequence of points is constructed such that the probability of the i-th element only depends on the $(i-1)$-th element, plus random numbers. Each step in the sequence is determined by a conditional probability $K(\boldsymbol{\theta}|\boldsymbol{\theta}')$ that must satisfy the *detailed balance condition*

$$\frac{\mathcal{P}_{\rm target}(\boldsymbol{\theta})}{\mathcal{P}_{\rm target}(\boldsymbol{\theta}')} = \frac{K(\boldsymbol{\theta}|\boldsymbol{\theta}')}{K(\boldsymbol{\theta}'|\boldsymbol{\theta})}. \tag{4.18}$$

The exact form of K will be subject to the specific MCMC algorithm. Popular MCMC algorithms include Metropolis-Hastings algorithm, Gibbs sampling, slice sampling, among others.

There are two significant issues to tackle when working with an MCMC sampler. The first is that it takes time for the sample to reach an equilibrium distribution, known as the *burn-in* period. In consequence, about 30-50% of the initial points should be discarded.

The second aspect is determining the convergence, where one knows whether the number of points in the chain is large enough to assure that the equilibrium state has been reached. There are a few diagnostic tools that can be used to determine convergence but by far, the most common and most relevant is the Gelman-Rubin (GR) *convergence criterion.* Given a model with an arbitrary number of parameters, let us focus on a single parameter θ. Suppose we have M independent chains of N points each (after burn-in has been discarded), and let $\theta_j^{(i)}$ represent the i-th value in the j-th chain. The mean value of each chain is given by

$$\langle\theta\rangle_j = \frac{1}{N}\sum_{i=1}^{N}\theta_j^{(i)}, \tag{4.19}$$

while the overall mean will be

$$\langle\theta\rangle = \frac{1}{M}\sum_{j=1}^{M}\langle\theta\rangle_j = \frac{1}{NM}\sum_{i=1}^{N}\sum_{j=1}^{M}\theta_j^{(i)}. \tag{4.20}$$

By definition, the variance of each chain is

$$\sigma_j^2 = \frac{1}{N-1}\sum_{i=1}^{N}\left(\theta_j^{(i)} - \langle\theta\rangle_j\right)^2, \tag{4.21}$$

which means that the mean of the variances can be written as

$$W = \frac{1}{M}\sum_{j=1}^{M}\sigma_j^2 = \frac{1}{M(N-1)}\sum_{j=1}^{M}\sum_{i=1}^{N}\left(\theta_j^{(i)} - \langle\theta\rangle_j\right)^2. \tag{4.22}$$

This quantity can be compared to the variance of the chain means,

$$B = \frac{1}{M-1}\sum_{j=1}^{M}\left(\langle\theta\rangle_j - \langle\theta\rangle\right)^2 . \tag{4.23}$$

The ratio

$$R = \frac{\frac{N-1}{N}W + \frac{M+1}{M}B}{W} \tag{4.24}$$

is expected to asymptotically approach unity and accordingly can be regarded as a measure of convergence. The value to be met can be set somewhat arbitrarily, depending on the specific situation.

In the previous description, only one parameter was taken into account. In general, convergence will be reached when $R \approx 1$ individually for each of the parameters of the model.

4.3 Methodology

With the model described in section 4.1, the set of parameters is

$$\boldsymbol{\theta} = (\alpha_{\|}, \alpha_{\perp}, b, \beta, \Sigma_{\|}, \Sigma_{\perp}, \Sigma_s, a_{0,1}, a_{0,2}, a_{0,3}, a_{2,1}, a_{2,2}, a_{2,3}), \tag{4.25}$$

with the data vector given by the multipoles from the UNIT ELG post-reconstruction catalogues,

$$\boldsymbol{d} = \left(\xi_0(s_{\mathrm{min}}), \ldots, \xi_0(s_{\mathrm{max}}), \xi_2(s_{\mathrm{min}}), \ldots, \xi_2(s_{\mathrm{max}})\right), \tag{4.26}$$

where the upper bound of the fitting range was fixed to $s_{\mathrm{max}} = 160\,h^{-1}\mathrm{Mpc}$, while the lower bound s_{min} was varied as part of the tests described below.

In our fitter, the total number of free parameters is reduced by solving analytically for the broad-band coefficients in the following manner. Notice that the predicted vector can be decomposed into two contributions

$$\boldsymbol{y} = \tilde{\boldsymbol{y}} + \boldsymbol{y}^{\mathrm{bb}}, \tag{4.27}$$

where $\tilde{\boldsymbol{y}}$ corresponds to the model without the broad-band correction and $\boldsymbol{y}^{\mathrm{bb}}$ corresponds to the broad-band polynomials and therefore depends only on the set of parameters $\boldsymbol{\nu} = (a_{0,1}, a_{0,2}, a_{0,3}, a_{2,1}, a_{2,2}, a_{2,3})$. For a fixed value for the rest of the parameters, the chi-squared function can be thought of only in terms of $\boldsymbol{\nu}$ as

$$\chi^2(\boldsymbol{\nu}) = \sum_{ij}(\boldsymbol{d}-\boldsymbol{y})_i C^{-1}_{ij}(\boldsymbol{d}-\boldsymbol{y})_j = \sum_{ij}(\tilde{\boldsymbol{d}}-\boldsymbol{y}^{\mathrm{bb}})_i C^{-1}_{ij}(\tilde{\boldsymbol{d}}-\boldsymbol{y}^{\mathrm{bb}})_j. \tag{4.28}$$

Here the new data vector is defined as $\tilde{\boldsymbol{d}} = \boldsymbol{d} - \tilde{\boldsymbol{y}}$. In this case, the elements of $\boldsymbol{y}^{\mathrm{bb}}$ depend linearly on the elements of $\boldsymbol{\nu}$, as

$$y_i^{\mathrm{bb}} = \sum_j \nu_j f_j(s_i), \tag{4.29}$$

where $f_j(s) = s^{-2}, s^{-1}, s$, depending on j in consistency with eq. (4.11). Since these functions are linearly independent, χ^2 is minimised by setting

$$\boldsymbol{\nu} = \left(AC^{-1}A^T\right)^{-1} AC^{-1}\tilde{\boldsymbol{d}}, \tag{4.30}$$

where

$$A_{ij} = f_i(x_j). \tag{4.31}$$

In this way, for any given value of the remaining parameters, the chi squared is analytically minimised with respect to the broad-band coefficients and we are left with a set of 7 free parameters

$$\boldsymbol{\theta} = (\alpha_{\parallel}, \alpha_{\perp}, b, \beta, \Sigma_{\parallel}, \Sigma_{\perp}, \Sigma_s). \tag{4.32}$$

The posterior of this set of parameters was sampled by making use of the *Zeus MCMC* sampler by Karamanis and Beutler 2020. Zeus is an implementation of a recently developed algorithm, *ensemble slice sampling*, introduced in the same paper. We set a flat prior, and a Gaussian likelihood $\mathcal{L} \propto \exp\left(-\frac{1}{2}\chi^2\right)$, where the χ^2 is calculated with the analytical broad-band coefficients discussed above. To be specific, at the i-th step, chi squared is minimised with respect to the broad-band coefficients by fixing the rest of the parameters to $\boldsymbol{\theta}^{(i)}$.

Instead of having one sampler at a time, Zeus works with an ensemble of *walkers* that explore the parameter space. We set the number of walkers to 14 (two times the number of parameters) and ran 8 independent ensembles in parallel. For each ensemble, we combined the chains of the 14 walkers. In this fashion, the Gelman-Rubin diagnostic test was assessed with the 8 ensemble chains. The convergence criterion was set to $R = 1.01$, with a burn-in of 30%. Lastly, the 8 chains were merged and the statistics are reported for the merged chain.

Our code will be publicly available on a GitHub repository [1]. It is written in *Python 3* and works by taking the model of section 4.1 and producing the corresponding script for the Zeus sampler.

The sampler was run on the Cori supercomputer that forms part of the National Energy Research Scientific Computing Center (NERSC) of the

---

[1] `https://github.com/alexzpi/BAO_fitter/`

DOE. Specifically, the Haswell compute nodes of Cori were used. They comprise two sockets populated with a 2.3 GHz 16-core Intel Xeon Processor each and have a memory of 128 GB DDR4 2133 MHz.

The main objective of this work was to test the performance of the BAO fitter under different conditions. The BAO fits were done with the following variations, in accordance with the Stage 2 of the BAO Mock Challenge (cf. section 3.4):

- Covariance matrix: Fixed amplitude vs. non-fixed amplitude. In both cases, the covariance matrices come from the post-reconstruction EZmocks with a smoothing scale of $15\,h^{-1}$Mpc, regardless of the smoothing scale of the UNIT catalogues.

- Reconstruction convention: Anisotropic reconstruction vs. isotropic reconstruction. For both types of covariance matrices.

- Scale of smoothing: $\Sigma_{\mathrm{smooth}} = 5\,h^{-1}\mathrm{Mpc}, 10\,h^{-1}\mathrm{Mpc}, 15\,h^{-1}\mathrm{Mpc}$. For all of the cases specified above.

- Fitting range: $s_{\mathrm{min}} = 35\,h^{-1}\mathrm{Mpc}, 45\,h^{-1}\mathrm{Mpc}, 55\,h^{-1}\mathrm{Mpc}$. For all of the cases specified above.

For the purpose of this work, the following additional tests were run:

- Fixing sigmas: We tested the effect of having only 4 free parameters instead of 7, by fixing $\Sigma_{\parallel}, \Sigma_{\perp}, \Sigma_s$ to their best-fit values, determined by numerically minimising χ^2.

- Covariance matrix smoothing: Given that the original tests were run with a covariance matrix corresponding to a single smoothing scale, in this case we made use of the non-fixed amplitude covariance matrices constructed from the post-reconstruction EZmocks with the proper smoothing scale corresponding to their UNIT counterpart.

- Multipole calculation: We had access to two sets of correlation function multipoles for each case: (i) one calculated with the LS estimator by counting pairs and (ii) a second set calculated by fast Fourier transforming the power spectrum multipoles. This test consisted in determining how sensitive the fit is to the use of this approximate multipoles.

4.4 Results and Discussion

This section is divided as follows. Before delving into the details of the results, the convergence of the chains is discussed in subsection 4.4.1. Subsections 4.4.3 and 4.4.4 are dedicated to the interpretation of the results corresponding to fixed amplitude and non-fixed amplitude covariances, respectively, including the different subcases.

4.4.1 Convergence test

As explained above, we set $R - 1 = 0.01$ for the Gelman-Rubin convergence criterion. More precisely, the built-in Gelman-Rubin implementation of the Zeus sampler was used. It has the advantage of calculating R at every given number of steps and stopping the sampling once the criterion has been reached. We set the configuration such that the criterion was checked every 100 steps. All of the fits stopped either at 400 or 500 steps. Note that although it may seem like a low number at first, the fact that we are using 8 independent chains of 14 walkers each compensates for this. If the total number of steps is N_s, the total number of points in the resultant posterior distribution sample will be

$$N_p = \lfloor 0.7 \times 14 \times 8 \times N_s \rfloor = \lfloor 78.4 \, N_s \rfloor, \tag{4.33}$$

where the 0.7 factor accounts for the burn-in. Therefore, for $N_s = 500$ the total number of points in the sample is $N_p = 39,200$.

Formally, the Gelman-Rubin criterion should suffice to argue that our chains converged successfully. Notwithstanding, it is always good practice to have a visual confirmation. Figure 4.1 is a corner plot that illustrates how the confidence levels, along with the 1-D distributions, evolve with the number of points. The confidence levels (CL) shown correspond to 68% (1-σ) and 95 (2-σ). Only the subspace $(\alpha_{\parallel}, \alpha_{\perp}, b, \beta)$ is plotted for clarity. This plot corresponds specifically to the fit with fixed amplitude covariance, anisotropic reconstruction, $\Sigma_{\text{smooth}} = 15 \, h^{-1}$Mpc and $s_{\text{min}} = 45 \, h^{-1}$Mpc; and was chosen arbitrarily. It must be mentioned that this particular example represents the general behaviour of the fits. The figure suggest that the posterior in this subspace convergences to a multivariate Gaussian-like distribution. Notice that the confidence levels for the 50% of the points are very close to the ones for the 100%, which can lead us to conclude that $R = 0.01$ exceeds the needs of our present purposes.

On the other hand, it is important to keep in mind that the convergence test was applied to the 8 independent chains, meaning that it ensures the convergence of the merged chain, but not necessarily the convergence of the individual chains. This is depicted in Figure 4.2, where confidence levels are plotted for the results obtained from the same fit as in Figure 4.1. The distribution from the 8 independent chains is shown along with the one from the merged chain. Note that the contours from the independent chains are less well-defined than the contours from the merged chain. Another interesting feature on this plot is the fact that the 2-D projections that involve any of the parameters $\Sigma_{\|}$, $\Sigma_{\perp}$ and Σ_s do not seem to follow a Gaussian distribution.

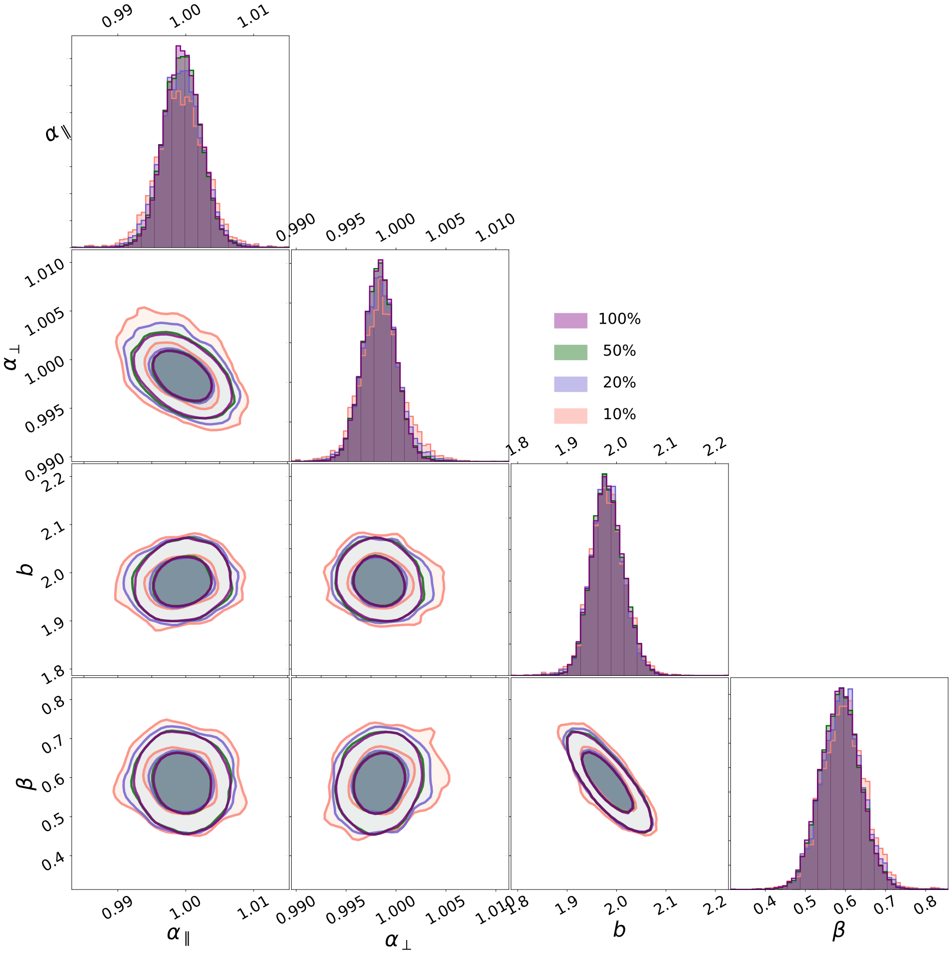

Figure 4.1: Corner plot for the subspace $(\alpha_\parallel, \alpha_\perp, b, \beta)$ showing the evolution of the distribution with the number of points. Different colours represent different percentages of the total number of points: 10%, 20%, 50% and 100%.

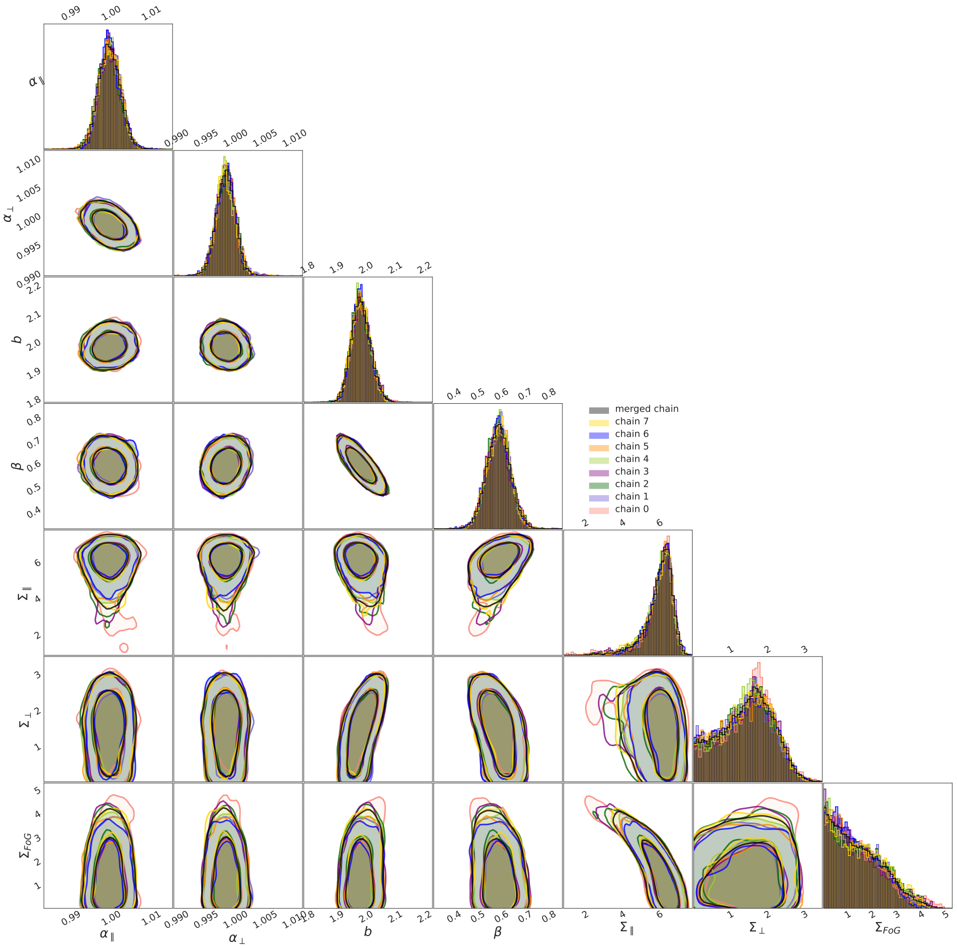

Figure 4.2: Results obtained from individual chains are compared with the merged chain.

4.4.2 On how the results are reported

In the following subsections, the values for $\alpha_\parallel$ and $\alpha_\perp$ that are presented correspond to the average of the distribution from the merged chains, whereas the errors correspond to the standard deviation

$$\sigma_\theta = \sqrt{\frac{1}{N-1}\sum_i \left(\theta^{(i)} - \langle\theta\rangle\right)^2}, \tag{4.34}$$

where θ can be either $\alpha_\parallel$ or $\alpha_\perp$ and $\langle\theta\rangle$ indicates the mean, as usual.

When reporting the mean of the different subcases, the calculation is carried out by weighting each value with the inverse of their respective variance $1/\sigma^2$, as follows. Given N subcases, with a reported value $\theta_j \pm \sigma_j$, the mean is given by

$$\langle\theta\rangle = C\sum_{j=1}^{N}\frac{\theta_j}{\sigma_j^2}. \tag{4.35}$$

Here, the normalisation factor is

$$C = \left(\sum_{j=1}^{N}\frac{1}{\sigma_j^2}\right)^{-1}. \tag{4.36}$$

Concerning the error, the weighted mean of the variances is

$$\langle\sigma^2\rangle = C\sum_{j=1}^{N}\frac{\sigma_j^2}{\sigma_j^2} = NC, \tag{4.37}$$

while the variance of the results is given by

$$\sigma^2_{\text{scatter}} = \frac{1}{N-1}C\sum_{j=1}^{N}\frac{(\theta_j - \langle\theta\rangle)^2}{\sigma_j^2}. \tag{4.38}$$

Hence, the total error is estimated by adding up both quantities in quadrature,

$$\sigma_{\text{total}} = \sqrt{\langle\sigma^2\rangle + \sigma^2_{\text{scatter}}}. \tag{4.39}$$

4.4.3 Fixed amplitude covariance

Figure 4.3 shows the results obtained for $\alpha_\parallel$ and $\alpha_\perp$ corresponding to the fixed amplitude covariance matrix with the different variations. The two most important features of this figure are: (i) All the individual measurements are consistent, within less than 2 standard deviations (2-σ), with the expected values for the fiducial cosmology ($\alpha_{||} = \alpha_{\perp} = 1$), which gives a reasonable estimate of the expected precision of our fitter. (ii) The errors are below the forecast errors for both Year 1 and even Year 5 of the DESI experiment.

The overall means of these measurements are:

$$\alpha_{||} = 0.9983 \pm 0.0029, \tag{4.40}$$

$$\alpha_{\perp} = 0.9989 \pm 0.0016. \tag{4.41}$$

There are several worth-mentioning factors in figure 4.3. Firstly, both $\alpha_{||}$ and $\alpha_{\perp}$ are in general underestimated, resulting in the underestimated means given above. This can be most likely attributed to cosmic variance. Additionally, results appear to be virtually insensitive to the fitting range, while the smoothing scale seems to play a significant role in determining both parameters. Now, let us discuss the tendencies for both parameters separately:

- For $\alpha_{||}$: Values tend to to increase with $\Sigma_{\rm smooth}$ for the anisotropic reconstruction convention. Measurements corresponding to the isotropic convention are always shifted towards lower values with respect to their anisotropic counterpart; for $\Sigma_{\rm smooth} = 10, 15\,h^{-1}$Mpc this difference is slightly less than 1-σ, although the difference is smaller for $\Sigma_{\rm smooth} = 5\,h^{-1}$Mpc, causing the isotropic case with smoothing scale $\Sigma_{\rm smooth} = 10\,h^{-1}$Mpc to yield the smallest value for $\alpha_{||}$. Note that a smoothing scale $\Sigma_{\rm smooth} = 5\,h^{-1}$Mpc tends to give peculiarly larger errors for the isotropic convention.

- For $\alpha_{\perp}$: For a given smoothing scale, values for both reconstruction conventions are in well agreement, differing by less than 0.03%. The less biased estimates are obtained with smoothing scale $\Sigma_{\rm smooth} = 10\,h^{-1}$Mpc, while the most biased results correspond to $\Sigma_{\rm smooth} = 15\,h^{-1}$Mpc. In this case, all of the errors are consistent with each other.

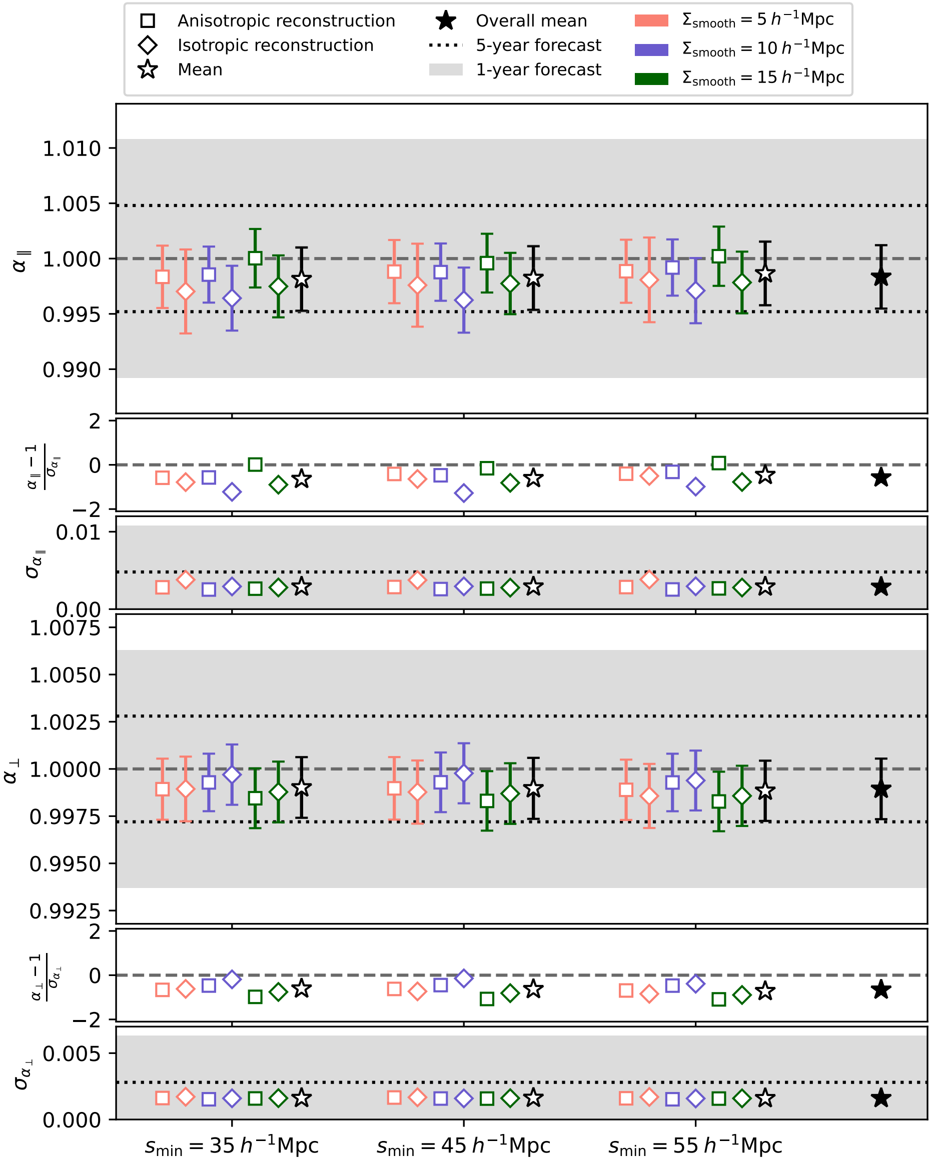

Figure 4.3: Variations of fitting range, smoothing scale and reconstruction convention for the fixed amplitude covariance case. The first three panels, from top to bottom, correspond to $\alpha_\parallel$, while the rest correspond to $\alpha_\perp$. In each case, from top to bottom, the plots show: the mean value of the chains with their respective error bars, the number of σ-s relative to the fiducial value, and the value of the standard deviation.

Note that it would not make sense to try to conclude, from this data alone, that there is a preferred configuration for the fitting. In particular, just by looking at figure 4.3 one could argue that the optimal settings for $\alpha_{\parallel}$ are: anisotropic convention, $\Sigma_{\rm smooth} = 15\, h^{-1}$Mpc and $s_{\rm min} = 35\, h^{-1}$Mpc; while at the same time asserting that for $\alpha_{\perp}$ the best settings are: isotropic convention, $\Sigma_{\rm smooth} = 10\, h^{-1}$Mpc and $s_{\rm min} = 45\, h^{-1}$Mpc. Which are, of course, non-compatible conclusions. Furthermore, recall that these tests were performed with only one ELG catalogue. An analysis where the systematics associated to our fitter could be studied thoroughly, as well as determining the best overall configuration for the fitting, would require the use of several simulations.

So far, we have been considering the results obtained from the chains, without considering what the actual fits look like. Figures 4.4, 4.5 and 4.6 show the data points with the respective theoretical template evaluated at the best-fit values. To be precise, we took the mean from the sample for $b, \beta, \alpha_{\parallel}, \alpha_{\perp}$, while for $\Sigma_{\parallel}$, $\Sigma_{\perp}$, and Σ_s the median value was used, as their distribution is far from Gaussian. Error bars were calculated by taking the square root of the diagonal of the covariance matrix. Each plot shows the list of values in addition to the value of the reduced chi squared χ^2/ν, where ν is the number of degrees of freedom (in this case, the length of the data vector minus the number of free parameters). Recall that this quantity can be used to measure the goodness of fit, and the rule of thumb indicates that ideally $\chi^2/\nu \sim 1$. It can be noted that for $\Sigma_{\rm smooth} = 5\, h^{-1}$Mpc the criteria is met in general (except for the anisotropic reconstruction with $s_{\rm min} = 35\, h^{-1}$Mpc), while for the other two cases the reduced chi-squared tends to be closer to 2. However, "by eye" the fitting appears to be fairly reasonable, while at the same time error bars are so small that they are not appreciable in most cases. Hence, the high values of chi squared may be due to these small errors (in comparison to the errors corresponding to the non-fixed amplitude covariance). Moreover, there appears to be a tendency for the isotropic reconstruction results to yield lower values of chi squared than their anisotropic counterpart, and thus presumably better fits.

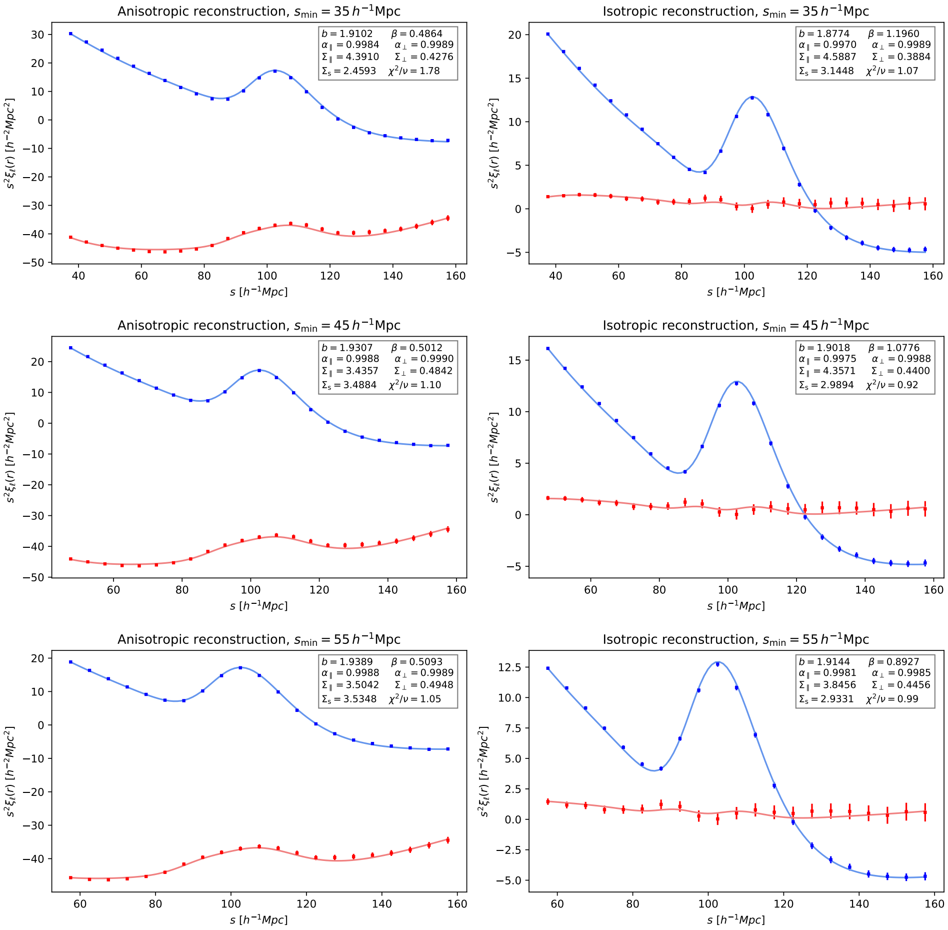

Figure 4.4: Fits corresponding to $\Sigma_{\rm smooth} = 5\,h^{-1}$Mpc with a fixed amplitude covariance matrix. Blue lines represent the monopole, while red lines represent the quadrupole.

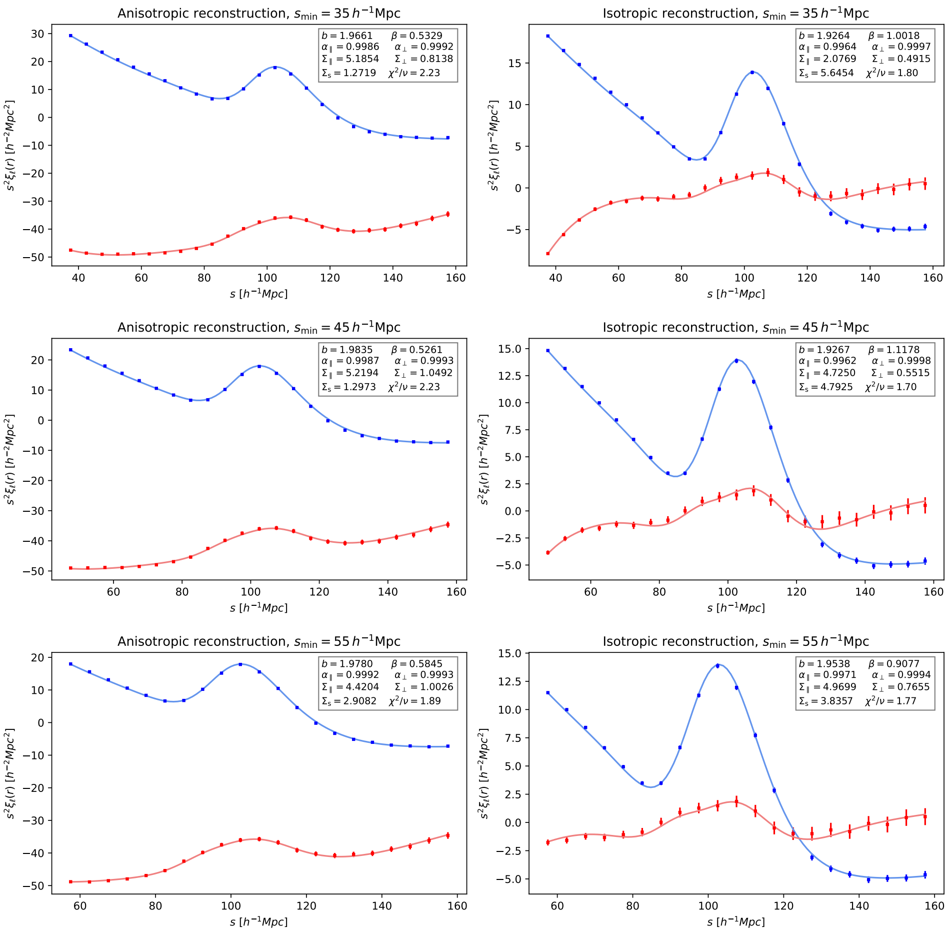

Figure 4.5: Fits corresponding to $\Sigma_{\rm smooth} = 10\,h^{-1}$Mpc with a fixed amplitude covariance matrix. Blue lines represent the monopole, while red lines represent the quadrupole.

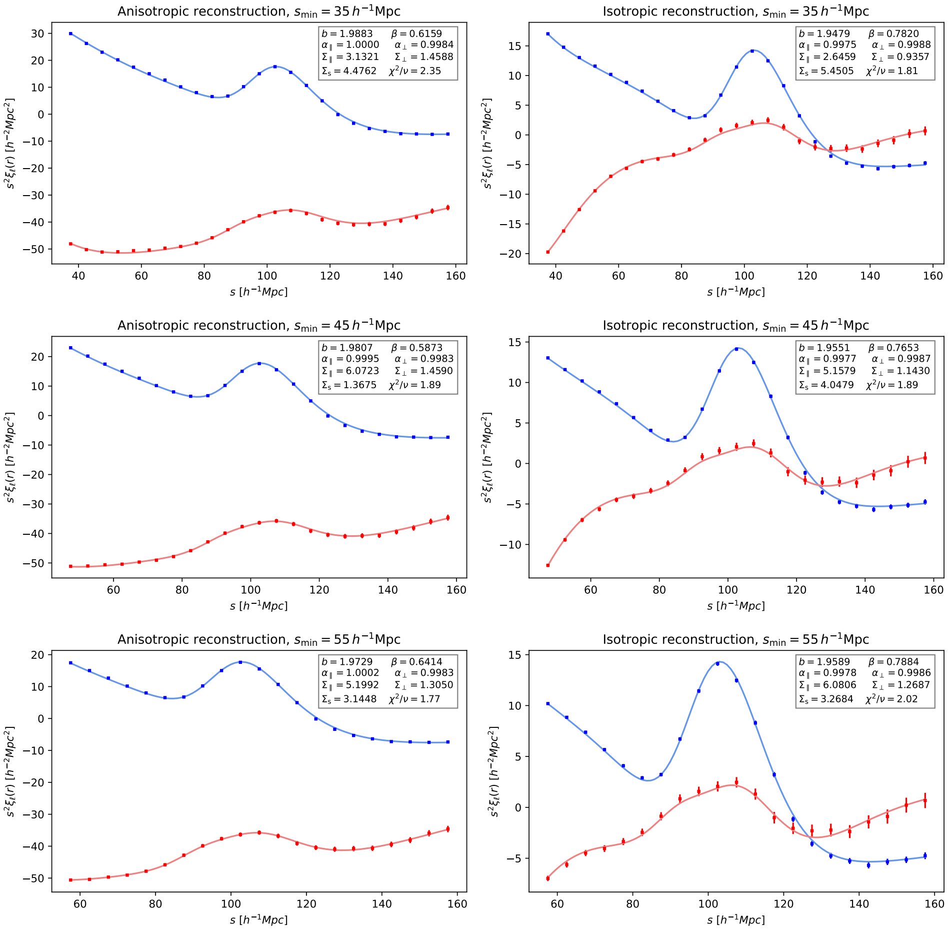

Anisotropic reconstruction, $s_{\rm min} = 35\,h^{-1}$Mpc

Isotropic reconstruction, $s_{\rm min} = 35\,h^{-1}$Mpc

Anisotropic reconstruction, $s_{\rm min} = 45\,h^{-1}$Mpc

Isotropic reconstruction, $s_{\rm min} = 45\,h^{-1}$Mpc

Anisotropic reconstruction, $s_{\rm min} = 55\,h^{-1}$Mpc

Isotropic reconstruction, $s_{\rm min} = 55\,h^{-1}$Mpc

Figure 4.6: Fits corresponding to $\Sigma_{\rm smooth} = 15\,h^{-1}$Mpc with a fixed amplitude covariance matrix. Blue lines represent the monopole, while red lines represent the quadrupole.

4.4.4 Non-fixed amplitude covariance

For non-fixed amplitude covariance (Figure 4.7), the tendencies are practically the same as in the previous case, with the noticeable difference that now the error bars have increased by about 60% and 40% for $\alpha_{\parallel}$ and $\alpha_{\perp}$, respectively. Note that despite these larger errors, they remain significantly smaller than the forecasted error for the Year 1 of DESI. With respect to the Year 5 forecast, errors for $\alpha_{\perp}$ still exceed the precision, while errors for $\alpha_{\parallel}$ are only just in agreement. Moreover, the former finding with regard to the 2-σ intervals remains valid. The overall means are

$$\alpha_{\parallel} = 1.0004 \pm 0.0047, \tag{4.42}$$

$$\alpha_{\perp} = 0.9988 \pm 0.0023. \tag{4.43}$$

The errors are 162% and 143% of the respective values for the fixed amplitude covariance matrix.

Note that this measurement for $\alpha_{\perp}$ seems to have the same accuracy as the one in the previous section. In contrast, the value for $\alpha_{\parallel}$ obtained in this case is more accurate than the one for fixed amplitude covariance. This is due to the fact that, as opposed to the behaviour shown in Figure 4.3, where all values of $\alpha_{\parallel}$ are underestimated, in Figure 4.7 there is a balance between underestimated and overestimated values. Comparing each subcase individually, it can be seen that for non-fixed amplitude covariance values are systematically shifted towards higher values by 15-30%.

Figures 4.8, 4.9 and 4.10 show the data points in comparison with the model evaluated at the best-fit values. The reduced chi-squared values have decreased with respect to those obtained with the fixed-amplitude covariance matrix by virtue of the larger error bars, as one would naturally expect.

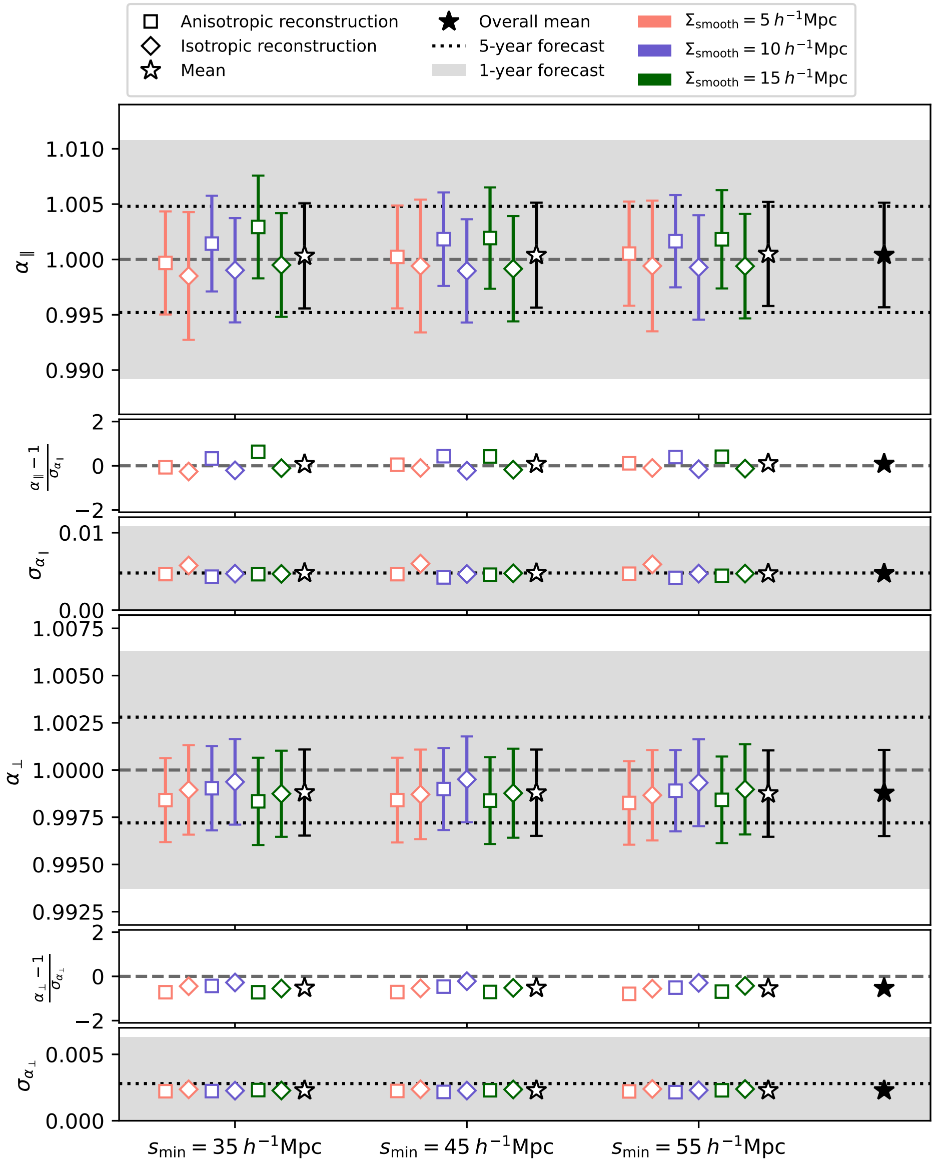

Figure 4.7: Variations of fitting range, smoothing scale and reconstruction convention for the non-fixed amplitude covariance case.

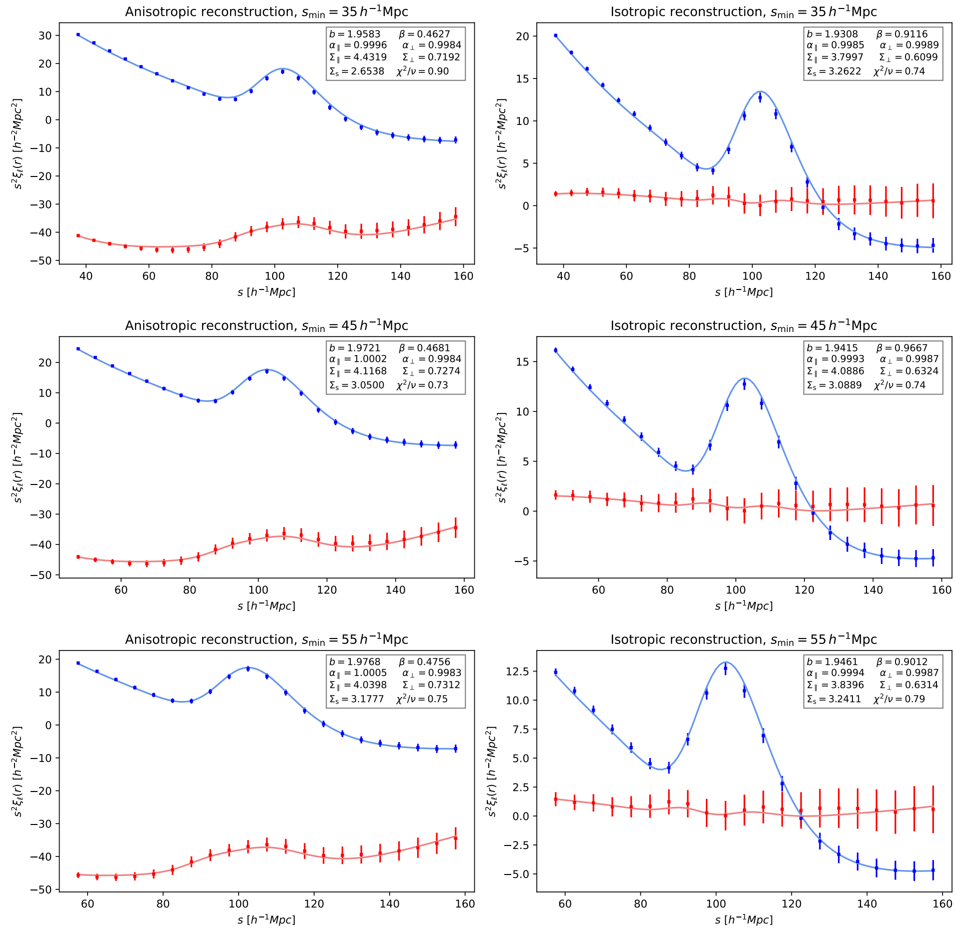

Figure 4.8: Fits corresponding to $\Sigma_{\text{smooth}} = 5\,h^{-1}$Mpc with a non-fixed amplitude covariance matrix. Blue lines represent the monopole, while red lines represent the quadrupole.

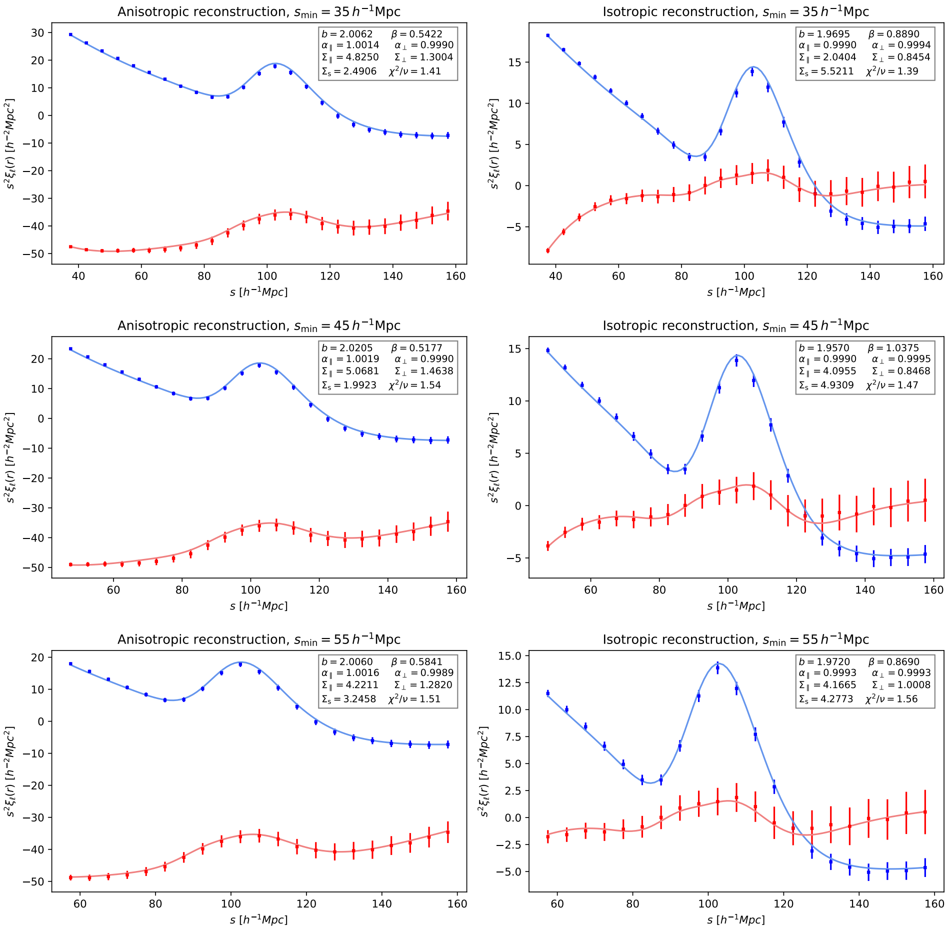

Figure 4.9: Fits corresponding to $\Sigma_{\text{smooth}} = 10\,h^{-1}$Mpc with a non-fixed amplitude covariance matrix. Blue lines represent the monopole, while red lines represent the quadrupole.

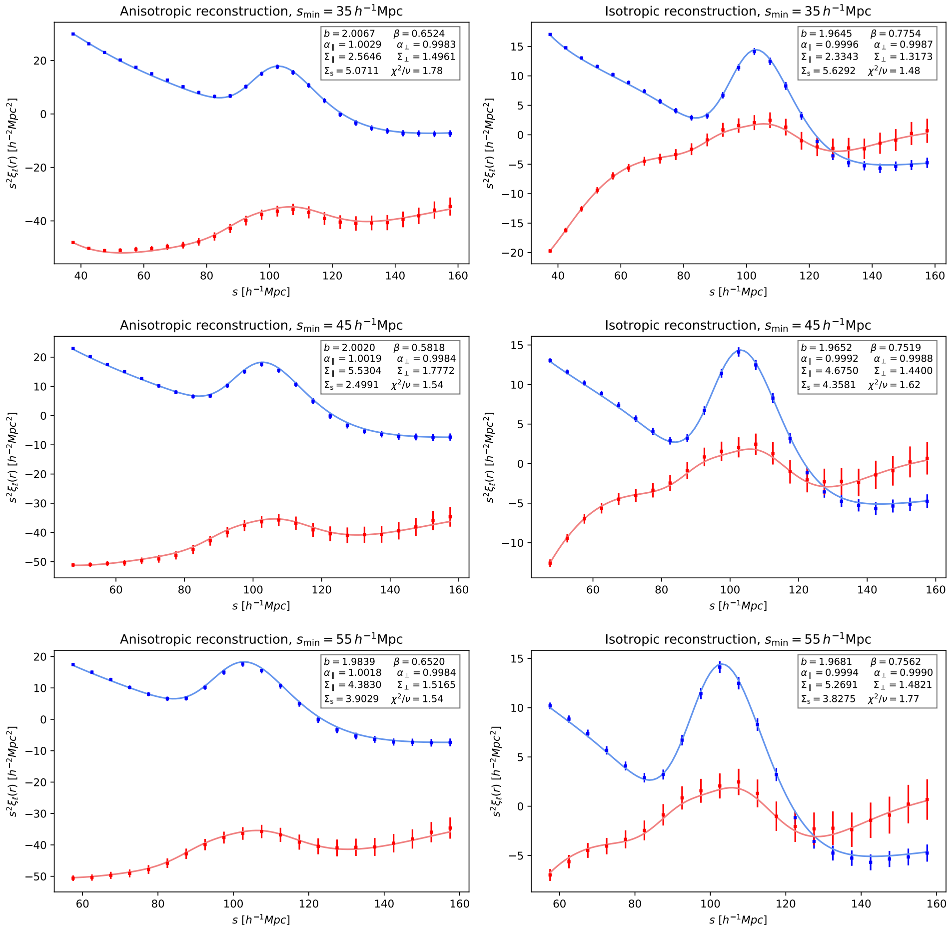

Figure 4.10: Fits corresponding to $\Sigma_{\rm smooth} = 15\,h^{-1}$Mpc with a non-fixed amplitude covariance matrix. Blue lines represent the monopole, while red lines represent the quadrupole.

4.4.5 Additional tests

Fixing sigmas

Figure 4.11 compares the values measured with our standard methodology with those obtained by reducing the number of free parameters (cf. 4.3), where $\Sigma_\parallel, \Sigma_\perp$ and Σ_s were kept fixed to the values obtained by minimising χ^2 *a priori*. The differences are negligible in the main: between 0.0015% and 0.012%.

Even though these sigmas are treated as nuisance parameters in our fitter, recall that they have actual physical meaning (cf. 2.1.2, 2.5), unlike the broad-band correction terms. Thus, dispensing with them as free parameters should not be a trivial matter, especially considering that their marginalised posterior is not Gaussian-like, but rather a spread distribution with no clear centre. The following explanation may account for the fact that practically the same measurements are recovered as with the regular methodology: when minimising χ^2, the numerical optimisation method (namely, the *scipy* implementation of the BFGS algorithm) converges to one of the values enclosed withing the 68% confidence level for $(\Sigma_\parallel, \Sigma_\perp, \Sigma_s)$, not necessarily the mean or the median of the posterior; this value is kept fixed during the MCMC, causing the broad-band coefficients to be the only parameters to modulate the non-linearities. Hence, the fitter "compensates" for the lack of free sigmas by tuning the broad-band coefficients accordingly, since they are analytically solved for, as opposed to the rest of the parameters. This behaviour can be regarded as a reassurance of the robustness of our methodology.

Covariance and smoothing scale

As stated above, the official results of the BAO Mock Challenge were calculated using the same covariance matrix corresponding to a single smoothing scale $\Sigma_{\rm smooth} = 15\,h^{-1}$Mpc with all of the multipoles sets, regardless of the smoothing scale of the catalogues. In Figure 4.12, the effect of this simplification is illustrated for the case of non-fixed amplitude covariance. Only results for $\Sigma_{\rm smooth} = 5\,h^{-1}$Mpc and $\Sigma_{\rm smooth} = 10\,h^{-1}$Mpc are shown, as the results for $\Sigma_{\rm smooth} = 15\,h^{-1}$Mpc do not suffer from this additional bias.

For $\alpha_\parallel$, measurements with the respective covariance (filled markers) show a tendency towards lower values, with a mean shift of 0.14% with respect to the previously reported numbers (unfilled markers). Errors do not vary significantly, although there is special case: isotropic reconstruction with smoothing scale of $5\,h^{-1}$Mpc, where the previously anomalous large error has been reduced.

The differences in $\alpha_\perp$ exhibit a slightly different behaviour. For the smoothing scale $\Sigma_{\rm smooth} = 10\,h^{-1}$Mpc, the new values are moderately smaller than the original ones, while for $\Sigma_{\rm smooth} = 5\,h^{-1}$Mpc, they are generally larger, albeit barely appreciably. Standard deviations remain virtually the same.

Multipoles (FFT vs. pair counts)

In Figure 4.13 a general upward trend can be discerned for $\alpha_\parallel$ values obtained with the FFT multipoles with respect to the original measurements, with values shifting up to 0.15%. In general, the shift is more pronounced for the anisotropic convention and there are cases, corresponding to the isotropic convention, where the shift is actually towards lower values, for example for a smoothing scale of $15\,h^{-1}$Mpc with $s_{\rm min} = 45\,h^{-1}$Mpc and $s_{\rm min} = 55\,h^{-1}$Mpc. There is no significant impact on the errors; although some values of $\frac{\alpha_\parallel - 1}{\sigma_{\alpha_\parallel}}$ are slightly improved as a result of the upward shift. This may be misleading, however, since the results for this particular realisation tend to systematically underestimate $\alpha_\parallel$, as discussed in 4.4.3.

Conversely, values for $\alpha_\perp$ are modified in such a way that their magnitude is moderately smaller than the previous ones calculated by making use of the pair-counts multipoles. The tendency is clear regardless of the reconstruction type; although it can be seen that for $\Sigma_{\rm smooth} = 5\,h^{-1}$Mpc the anisotropic reconstruction results are less sensitive to the change. As a result of the original underestimation of the parameters, the opposite effect takes place to the one observed for $\alpha_\parallel$; namely $\frac{\alpha_\perp - 1}{\sigma_{\alpha_\perp}}$ is slightly worsened, yet it remains within the 2-σ range.

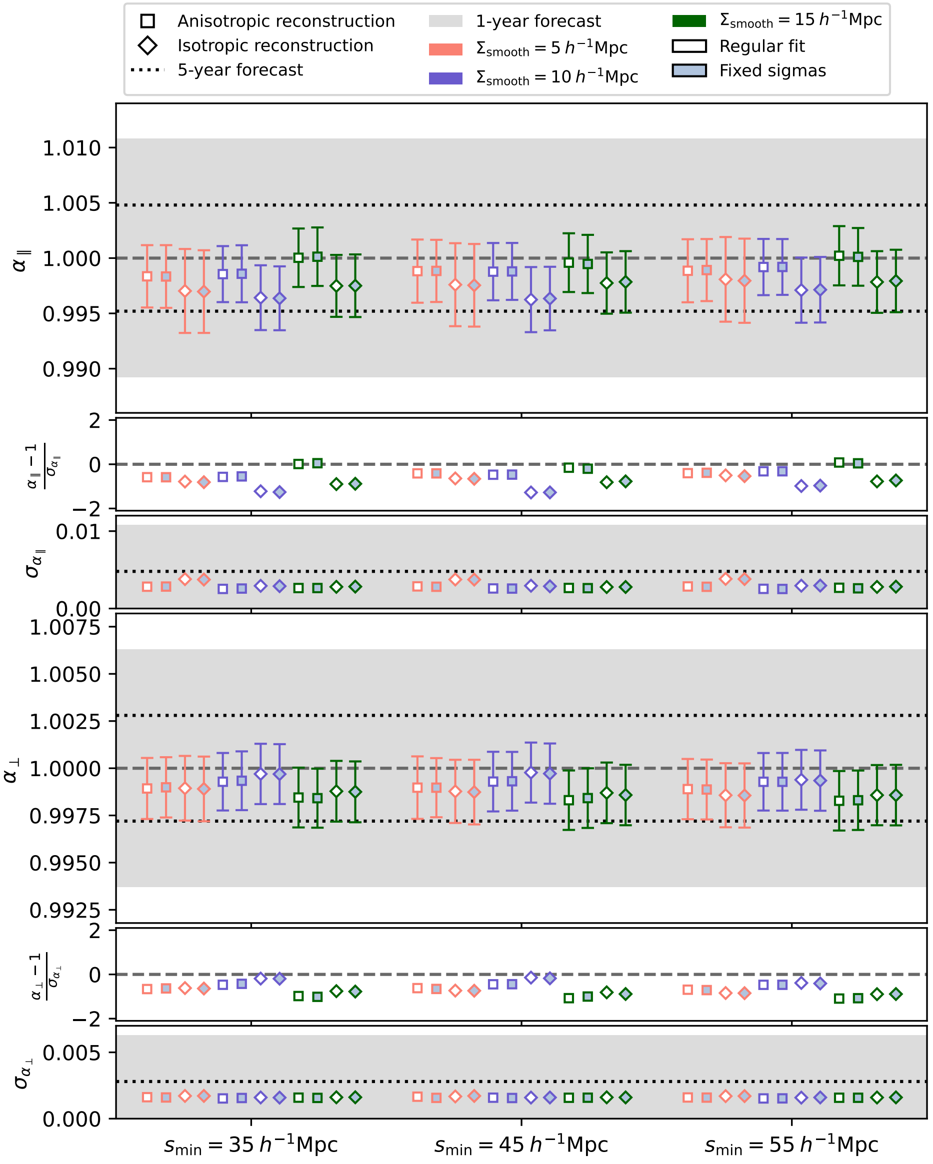

Figure 4.11: Comparison of the regular fit methodology (unfilled markers) vs. fits with fixed $\Sigma_\parallel, \Sigma_\perp$ and Σ_s (filled markers).

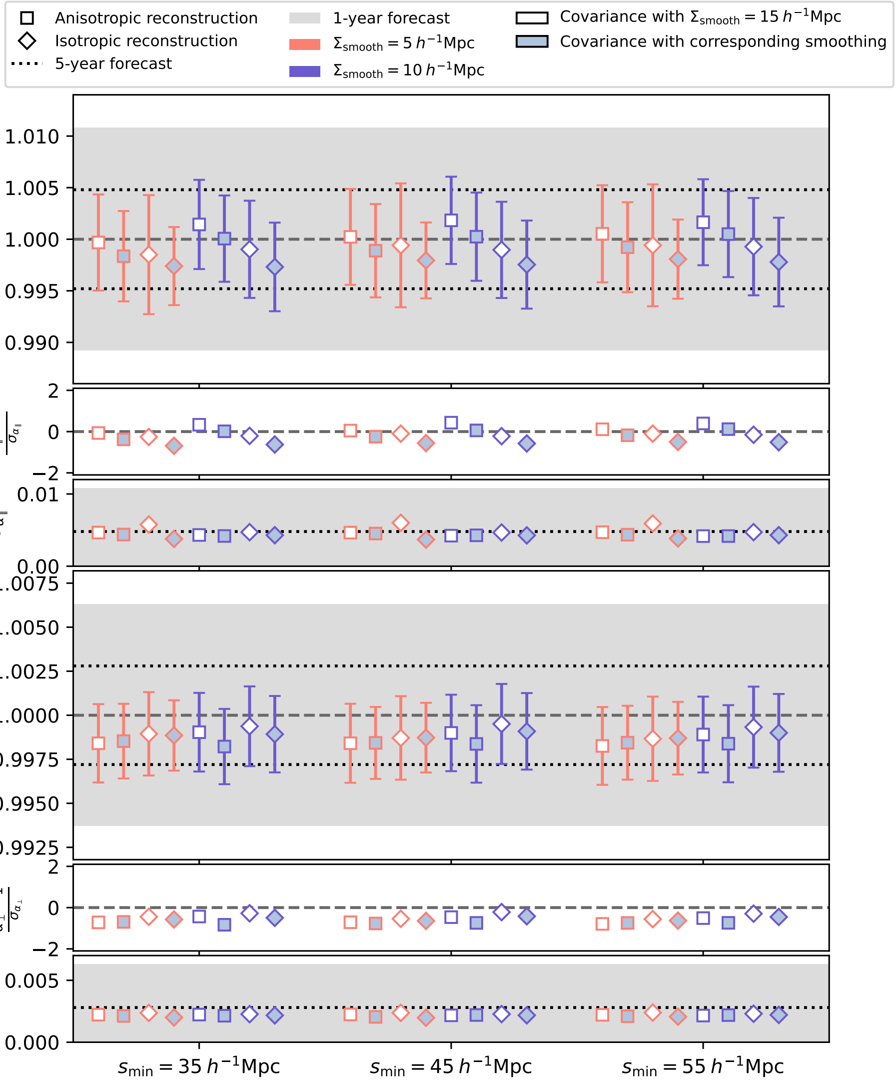

Figure 4.12: Tests of the effect of using the wrong smoothing scale in the covariance matrix, as opposed of using the respective smoothing.

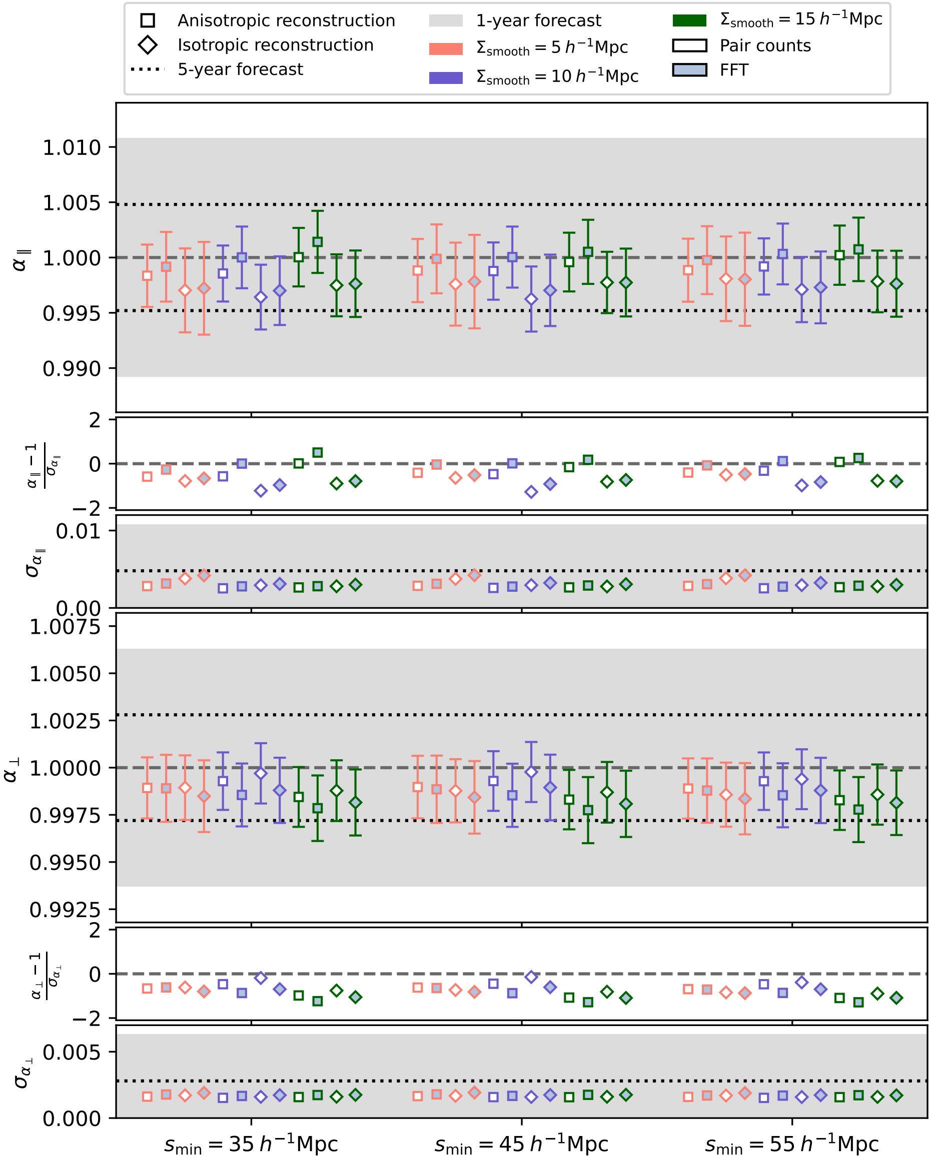

Figure 4.13: Comparison of the results obtained by using the LS estimator for the multipoles (unfilled markers) vs. using approximate multipoles by Hankel transforming the power spectrum multipoles (filled markers).

Chapter 5

Summary and Conclusions

In this thesis, the generalities of the BAO method were presented following an instructive approach rather than a comprehensive one. Emphasis was placed on the physics concerning the observed large-scale structure clustering measurements at low z. The sound waves that propagated in the baryon-photon plasma during the early Universe froze in place at the epoch of recombination, yielding a resonant wavelength in the two-point statistics of the matter distribution. This preferred scale has a comoving value of $100\,h^{-1}$Mpc. The resultant overdensities served as seeds to the large-scale structure formation that took place during the matter dominated era. The galaxies we observe today are used as tracers of the underlying matter distribution. However, several effects must be taken into account if one wants to be able to recover cosmological information from a galaxy survey.

In particular, the anisotropic signal due to RSD was introduced along with the multipoles of the two-point statistics. They represent the central objects of our study, as in order to find constrains for the parameters of interest, multipoles measurements for the data contrasted with those coming from theory. In addition, the degradation of the BAO peak due to nonlinear gravitational collapse was thoroughly discussed and it was argued how it can be modelled by an anisotropic Gaussian damping. Reconstruction algorithms were reviewed as well; they re applied to galaxy catalogues with the objective of sharpening the BAO peak by decreasing the effects of linear bulk-flows. Most importantly, the role of the Alcock-Paczyński with regard to distance measurements was stressed. The information is comprised in the dilation parameters $\alpha_{\|}$ and $\alpha_{\perp}$, which are directly related to $H(z)$ and $D_A(z)$, respectively.

The methodology was tested in the context of Stage 2 of the BAO Mock

Challenge as part of the DESI Collaboration. Briefly, the Mock Challenge consists of testing and perfecting the BAO analysis pipeline by making use of galaxy mock catalogues. Namely, the ELG mocks derived from UNIT simulations were used as the main data, whereas covariance matrices were computed by making use of EZmock catalogues. Additionally, cubic boxes of side length of $3\,h^1$Gpc were used in this stage. UNIT simulations are an instance of full N-body simulations, but with a special variance reduction feature in the initial conditions. In contrast, EZmocks are fast simulations with the implementation of a effective biasing model. The general aspects of both N-body simulations and EZmocks were outlined in the text.

The implementation of the BAO fitter herein presented follows the modern Bayesian approach in combination with a Markov Chain Monte Carlo method. Specifically, the brand-new *Zeus* sampler was made use of, which is an implementation of the ensemble slice sampling algorithm. Our fitter works in configuration space and analytically solves for the broad-band correction terms, so that it effectively works in a 7-dimensional parameter space $\boldsymbol{\theta} = (b, \beta, \alpha_{||}, \alpha_{\perp}, \Sigma_{||}, \Sigma_{\perp}, \Sigma_s)$. The dilation alpha parameters are the parameters of interest, while the remaining parameters act as nuisance parameters and are marginalised over.

In order to test the performance of the BAO fitter, as part of the official tasks of the Stage 2 of the Mock Challenge; variations in the type of covariance matrix, reconstruction algorithm, smoothing scale, and fitting range were considered. Our fitter exhibits an extraordinarily low sensitivity to all of these differences, apart from the expected increase in errors for the non-fixed amplitude covariance with respect to the fixed one. Fitting range seems to play a negligible role in general, whereas differences are easily perceived when varying the smoothing scale. Values corresponding to the different reconstruction conventions differ from each other in a systematic way. Values for $\alpha_{||}$ and $\alpha_{\perp}$ tend to be underestimated in general for the fixed-amplitude covariance cases, which can be attributed to cosmic variance. In turn, $\alpha_{||}$ measurements are slightly more accurate for the non-amplitude covariance case, as a result of an upward shift trend. The most important attribute of these results is the following: for the fixed-amplitude covariance matrix, we were able to test the methodology with the required precision for the Year 1 analyses. For this UNIT catalogue, we found an error that corresponds to 25% of the statistical error expected for DESI Year 1 data. The results obtained in this work are compatible within 2-σ with the Gaussian distribution expected for the errors. With respect to the Year 5 forecast, the errors obtained are of the same order of magnitude, which means that for Year 5 analyses mocks with greater effective volume would be required in order to reach the required precision. Taking into account the different variations in the methodology, a scattering of 0.03% and 0.01% was found for $\alpha_{\parallel}$ and $\alpha_{\perp}$, respectively; which was added in quadrature to the statistical error. This signifies that, for the analysed mock, these variations could only account for 0.9% of the total error for $\alpha_{\parallel}$ and 0.4% of the total error for $\alpha_{\perp}$.

Bibliography

Alam, Shadab, Marie Aubert, et al. (Apr. 2021). "Completed SDSS-IV extended Baryon Oscillation Spectroscopic Survey: Cosmological implications from two decades of spectroscopic surveys at the Apache Point Observatory". In: *Physical Review D* 103.8, 083533, p. 083533. DOI: `10.1103/PhysRevD.103.083533`. arXiv: `2007.08991 [astro-ph.CO]`.

Alam, Shadab, John A Peacock, et al. (July 2020). "Multitracer extension of the halo model: probing quenching and conformity in eBOSS". In: *Monthly Notices of the Royal Astronomical Society* 497.1, pp. 581–595. DOI: `10.1093/mnras/staa1956`. URL: `https://doi.org/10.1093%2Fmnras%2Fstaa1956`.

Albrecht, Andreas et al. (2006). *Report of the Dark Energy Task Force.* arXiv: `astro-ph/0609591 [astro-ph]`.

Alcock, C. and B. Paczynski (Oct. 1979). "An evolution free test for non-zero cosmological constant". In: *Nature* 281, p. 358. DOI: `10.1038/281358a0`.

Anderson, Lauren et al. (Apr. 2014). "The clustering of galaxies in the SDSS-III Baryon Oscillation Spectroscopic Survey: baryon acoustic oscillations in the Data Releases 10 and 11 Galaxy samples". In: *Monthly Notices of the Royal Astronomical Society* 441.1, pp. 24–62. ISSN: 0035-8711. DOI: `10.1093/mnras/stu523`. URL: `http://dx.doi.org/10.1093/mnras/stu523`.

Angulo, Raul E. and Andrew Pontzen (May 2016). "Cosmological N-body simulations with suppressed variance". In: *Monthly Notices of the Royal Astronomical Society: Letters* 462.1, pp. L1–L5. ISSN: 1745-3925. DOI: `10.1093/mnrasl/slw098`. eprint: `https://academic.oup.com/mnrasl/article-pdf/462/1/L1/8009434/slw098.pdf`. URL: `https://doi.org/10.1093/mnrasl/slw098`.

Ballinger, W. E., J. A. Peacock, and A. F. Heavens (Oct. 1996). "Measuring the cosmological constant with redshift surveys". In: *Monthly Notices of the Royal Astronomical Society* 282.3, pp. 877–888. DOI: `10.1093/`

mnras/282.3.877. URL: https://doi.org/10.1093%2Fmnras%2F282.3.877.

Barnes, Josh and Piet Hut (Dec. 1986). "A hierarchical O(N log N) force-calculation algorithm". In: *Nature* 324.6096, pp. 446–449. DOI: 10.1038/324446a0.

Bassett, Bruce A. and Renée Hlozek (2009). *Baryon Acoustic Oscillations*. arXiv: 0910.5224 [astro-ph.CO].

Baumgarten, Falk and Chia-Hsun Chuang (Aug. 2018). "Robustness of the covariance matrix for galaxy clustering measurements". In: *Monthly Notices of the Royal Astronomical Society* 480.2, pp. 2535–2543. ISSN: 0035-8711. DOI: 10.1093/mnras/sty1971. eprint: https://academic.oup.com/mnras/article-pdf/480/2/2535/25459809/sty1971.pdf. URL: https://doi.org/10.1093/mnras/sty1971.

Behroozi, Peter S., Risa H. Wechsler, and Hao-Yi Wu (Jan. 2013). "The ROCKSTAR Phase-space Temporal Halo Finder and the Velocity Offsets of Cluster Cores". In: *The Astrophysical Journal* 762.2, 109, p. 109. DOI: 10.1088/0004-637X/762/2/109. arXiv: 1110.4372 [astro-ph.CO].

Beutler, Florian et al. (2017). "The clustering of galaxies in the completed SDSS-III Baryon Oscillation Spectroscopic Survey: baryon acoustic oscillations in the Fourier space". In: *Monthly Notices of the Royal Astronomical Society* 464.3, pp. 3409–3430. ISSN: 1365-2966. DOI: 10.1093/mnras/stw2373. URL: http://dx.doi.org/10.1093/mnras/stw2373.

Busca, N. G. et al. (Apr. 2013). "Baryon acoustic oscillations in the Ly-α forest of BOSS quasars". In: *Astronomy & Astrophysics* 552, A96. ISSN: 1432-0746. DOI: 10.1051/0004-6361/201220724. URL: http://dx.doi.org/10.1051/0004-6361/201220724.

Chevallier, Michel and David Polarski (Apr. 2001). "Accelerating Universe with Scaling Dark Matter". In: *International Journal of Modern Physics D* 10.02, pp. 213–223. DOI: 10.1142/s0218271801000822. URL: https://doi.org/10.1142%2Fs0218271801000822.

Chuang, Chia-Hsun, Francisco-Shu Kitaura, et al. (Jan. 2015). "EZmocks: extending the Zel'dovich approximation to generate mock galaxy catalogues with accurate clustering statistics". In: *Monthly Notices of the Royal Astronomical Society* 446.3, pp. 2621–2628. DOI: 10.1093/mnras/stu2301. arXiv: 1409.1124 [astro-ph.CO].

Chuang, Chia-Hsun, Mariana Vargas-Magaña, and Shadab Alam (2020). *DESI mock challenge plan*.

Chuang, Chia-Hsun, Gustavo Yepes, et al. (May 2019). "UNIT project: Universe N-body simulations for the Investigation of Theoretical models from galaxy surveys". In: *Monthly Notices of the Royal Astronomical*

Society 487.1, pp. 48–59. DOI: 10.1093/mnras/stz1233. URL: https://doi.org/10.1093%2Fmnras%2Fstz1233.

Cole, Shaun et al. (Sept. 2005). "The 2dF Galaxy Redshift Survey: power-spectrum analysis of the final data set and cosmological implications". In: *Monthly Notices of the Royal Astronomical Society* 362.2, pp. 505–534. ISSN: 1365-2966. DOI: 10.1111/j.1365-2966.2005.09318.x. URL: http://dx.doi.org/10.1111/j.1365-2966.2005.09318.x.

Davis, M. and P. J. E. Peebles (Apr. 1983). "A survey of galaxy redshifts. V. The two-point position and velocity correlations." In: *The Astrophysical Journal* 267, pp. 465–482. DOI: 10.1086/160884.

Dawson, Kyle S. et al. (Jan. 2013). "The Baryon Oscillation Spectroscopic Survey of SDSS-III". In: *The Astrophysical Journal* 145.1, 10, p. 10. DOI: 10.1088/0004-6256/145/1/10. arXiv: 1208.0022 [astro-ph.CO].

DESI Collaboration (2016). *The DESI Experiment Part I: Science,Targeting, and Survey Design*. arXiv: 1611.00036 [astro-ph.IM].

Dodelson, Scott and Fabian Schmidt (2021). *Modern Cosmology*. 2nd ed. London: Academic Press. ISBN: 978-0-12-815948-4. DOI: https://doi.org/10.1016/C2017-0-01943-2.

Efstathiou, G. et al. (Feb. 1985). "Numerical techniques for large cosmological N-body simulations". In: *The Astrophysical Journal Supplement Series* 57, pp. 241–260. DOI: 10.1086/191003.

Eisenstein, Daniel J. and Wayne Hu (Apr. 1998). "Baryonic Features in the Matter Transfer Function". In: *The Astrophysical Journal* 496.2, pp. 605–614. ISSN: 1538-4357. DOI: 10.1086/305424. URL: http://dx.doi.org/10.1086/305424.

Eisenstein, Daniel J., Hee-Jong Seo, Edwin Sirko, et al. (Aug. 2007). "Improving Cosmological Distance Measurements by Reconstruction of the Baryon Acoustic Peak". In: *The Astrophysical Journal* 664.2, pp. 675–679. ISSN: 1538-4357. DOI: 10.1086/518712. URL: http://dx.doi.org/10.1086/518712.

Eisenstein, Daniel J., Hee-Jong Seo, and Martin White (Aug. 2007). "On the Robustness of the Acoustic Scale in the Low-Redshift Clustering of Matter". In: *The Astrophysical Journal* 664.2, pp. 660–674. ISSN: 1538-4357. DOI: 10.1086/518755. URL: http://dx.doi.org/10.1086/518755.

Eisenstein, Daniel J., Idit Zehavi, et al. (Nov. 2005). "Detection of the Baryon Acoustic Peak in the Large-Scale Correlation Function of SDSS Luminous Red Galaxies". In: *The Astrophysical Journal* 633.2, pp. 560–574. ISSN: 1538-4357. DOI: 10.1086/466512. URL: http://dx.doi.org/10.1086/466512.

Feng, Yu et al. (Aug. 2016). “FastPM: a new scheme for fast simulations of dark matter and haloes”. In: *Monthly Notices of the Royal Astronomical Society* 463.3, pp. 2273–2286. DOI: `10.1093/mnras/stw2123`. URL: `https://doi.org/10.1093%2Fmnras%2Fstw2123`.

Fisher, Karl. B. et al. (Apr. 1994). “Clustering in the 1.2-Jy IRAS Galaxy Redshift Survey – II. Redshift distortions and $\xi(r_p, \pi)$”. In: *Monthly Notices of the Royal Astronomical Society* 267.4, pp. 927–948. ISSN: 0035-8711. DOI: `10.1093/mnras/267.4.927`. eprint: `https://academic.oup.com/mnras/article-pdf/267/4/927/9415505/mnras267-0927.pdf`. URL: `https://doi.org/10.1093/mnras/267.4.927`.

Hamann, Jan et al. (July 2010). “Cosmological parameters from large scale structure - geometric versus shape information”. In: *Journal of Cosmology and Astroparticle Physics* 2010.07, pp. 022–022. DOI: `10.1088/1475-7516/2010/07/022`. URL: `https://doi.org/10.1088%2F1475-7516%2F2010%2F07%2F022`.

Hamilton, A. J. S. (1998). “Linear Redshift Distortions: A Review”. In: *The Evolving Universe*, pp. 185–275. ISSN: 2214-7985. DOI: `10.1007/978-94-011-4960-0_17`. URL: `http://dx.doi.org/10.1007/978-94-011-4960-0_17`.

Hinton, Samuel R. et al. (Oct. 2016). “Measuring the 2D baryon acoustic oscillation signal of galaxies in WiggleZ: cosmological constraints”. In: *Monthly Notices of the Royal Astronomical Society* 464.4, pp. 4807–4822. ISSN: 0035-8711. DOI: `10.1093/mnras/stw2725`. eprint: `https://academic.oup.com/mnras/article-pdf/464/4/4807/8314205/stw2725.pdf`. URL: `https://doi.org/10.1093/mnras/stw2725`.

Hockney, R. W. and J. W. Eastwood (1988). *Computer simulation using particles*.

Ivanov, Mikhail M. and Sergey Sibiryakov (July 2018). “Infrared resummation for biased tracers in redshift space”. In: *Journal of Cosmology and Astroparticle Physics* 2018.07, pp. 053–053. DOI: `10.1088/1475-7516/2018/07/053`. URL: `https://doi.org/10.1088%2F1475-7516%2F2018%2F07%2F053`.

Jackson, J. C. (Feb. 1972). “A Critique of Rees’s Theory of Primordial Gravitational Radiation”. In: *Monthly Notices of the Royal Astronomical Society* 156.1, 1P–5P. ISSN: 0035-8711. DOI: `10.1093/mnras/156.1.1P`. eprint: `https://academic.oup.com/mnras/article-pdf/156/1/1P/9402724/mnras156-001P.pdf`. URL: `https://doi.org/10.1093/mnras/156.1.1P`.

Kaiser, Nick (July 1987). “Clustering in real space and in redshift space”. In: *Monthly Notices of the Royal Astronomical Society* 227, pp. 1–21. DOI: `10.1093/mnras/227.1.1`.

Karamanis, Minas and Florian Beutler (2020). *Ensemble Slice Sampling.* arXiv: `2002.06212 [stat.ML]`.

Landy, Stephen D. (Feb. 2002). “The Pairwise Velocity Distribution Function of Galaxies in the Las Campanas Redshift Survey, Two-Degree Field Survey, and Sloan Digital Sky Survey”. In: *The Astrophysical Journal* 567.1, pp. L1–L4. DOI: `10.1086/339900`. URL: `https://doi.org/10.1086%2F339900`.

Landy, Stephen D. and Alexander S. Szalay (July 1993). “Bias and Variance of Angular Correlation Functions”. In: *The Astrophysical Journal* 412, p. 64. DOI: `10.1086/172900`.

Landy, Stephen D., Alexander S. Szalay, and Thomas J. Broadhurst (Feb. 1998). “The Pairwise Velocity Distribution of Galaxies in the Las Campanas Redshift Survey”. In: *The Astrophysical Journal* 494.2, pp. L133–L136. DOI: `10.1086/311197`. URL: `https://doi.org/10.1086%2F311197`.

Lewis, Antony, Anthony Challinor, and Anthony Lasenby (Aug. 2000). “Efficient Computation of Cosmic Microwave Background Anisotropies in Closed Friedmann-Robertson-Walker Models”. In: *The Astrophysical Journal* 538.2, pp. 473–476. ISSN: 1538-4357. DOI: `10.1086/309179`. URL: `http://dx.doi.org/10.1086/309179`.

Linder, Eric V. (Mar. 2003). “Exploring the Expansion History of the Universe”. In: *Phys. Rev. Lett.* 90 (9), p. 091301. DOI: `10.1103/PhysRevLett.90.091301`. URL: `https://link.aps.org/doi/10.1103/PhysRevLett.90.091301`.

Matsubara, Takahiko (Mar. 2008). “Resumming cosmological perturbations via the Lagrangian picture: One-loop results in real space and in redshift space”. In: *Physical Review D* 77.6. DOI: `10.1103/physrevd.77.063530`. URL: `https://doi.org/10.1103%2Fphysrevd.77.063530`.

Mehta, Kushal T. et al. (May 2011). “Galaxy Bias And Its Effects On The Baryon Acoustic Oscillation Measurements”. In: *The Astrophysical Journal* 734.2, p. 94. ISSN: 1538-4357. DOI: `10.1088/0004-637x/734/2/94`. URL: `http://dx.doi.org/10.1088/0004-637X/734/2/94`.

Padmanabhan, Nikhil, Martin White, and J. D. Cohn (Mar. 2009). “Reconstructing baryon oscillations: A Lagrangian theory perspective”. In: *Physical Review D* 79.6. ISSN: 1550-2368. DOI: `10.1103/physrevd.79.063523`. URL: `http://dx.doi.org/10.1103/PhysRevD.79.063523`.

Peacock, J. A. and S. J. Dodds (Apr. 1994). "Reconstructing the linear power spectrum of cosmological mass fluctuations". In: *Monthly Notices of the Royal Astronomical Society* 267.4, pp. 1020–1034. ISSN: 0035-8711. DOI: `10.1093/mnras/267.4.1020`. eprint: `https://academic.oup.com/mnras/article-pdf/267/4/1020/4057489/mnras267-1020.pdf`. URL: `https://doi.org/10.1093/mnras/267.4.1020`.

Perlmutter, S. et al. (June 1999). "Measurements of Ω and Λ from 42 High-Redshift Supernovae". In: *The Astrophysical Journal* 517.2, pp. 565–586. ISSN: 1538-4357. DOI: `10.1086/307221`. URL: `http://dx.doi.org/10.1086/307221`.

Planck Collaboration, P. A. R. Ade, et al. (Sept. 2016). "Planck 2015 results. XIII. Cosmological parameters". In: *Astronomy & Astrophysics* 594, A13, A13. DOI: `10.1051/0004-6361/201525830`. arXiv: `1502.01589 [astro-ph.CO]`.

Planck Collaboration, N. Aghanim, et al. (Sept. 2020). "Planck 2018 results. IV. Cosmological Parameters". In: *Astronomy & Astrophysics* 641, A6. DOI: `10.1051/0004-6361/201833910`. URL: `https://doi.org/10.1051%2F0004-6361%2F201833910`.

Reid, Beth A. et al. (Apr. 2010). "Cosmological constraints from the clustering of the Sloan Digital Sky Survey DR7 luminous red galaxies". In: *Monthly Notices of the Royal Astronomical Society* 404.1, pp. 60–85. ISSN: 0035-8711. DOI: `10.1111/j.1365-2966.2010.16276.x`. eprint: `https://academic.oup.com/mnras/article-pdf/404/1/60/11177257/mnras0404-0060.pdf`. URL: `https://doi.org/10.1111/j.1365-2966.2010.16276.x`.

Riess, Adam G. et al. (Sept. 1998). "Observational Evidence from Supernovae for an Accelerating Universe and a Cosmological Constant". In: *The Astronomical Journal* 116.3, pp. 1009–1038. ISSN: 0004-6256. DOI: `10.1086/300499`. URL: `http://dx.doi.org/10.1086/300499`.

Ross, Ashley J. et al. (2017). "The clustering of galaxies in the completed SDSS-III Baryon Oscillation Spectroscopic Survey: observational systematics and baryon acoustic oscillations in the correlation function". In: *Monthly Notices of the Royal Astronomical Society* 464.1, pp. 1168–1191. ISSN: 1365-2966. DOI: `10.1093/mnras/stw2372`. URL: `http://dx.doi.org/10.1093/mnras/stw2372`.

Seo, Hee-Jong, Florian Beutler, et al. (2016). "Modeling the reconstructed BAO in Fourier space". In: *Monthly Notices of the Royal Astronomical Society* 460.3, pp. 2453–2471. ISSN: 1365-2966. DOI: `10.1093/mnras/stw1138`. URL: `http://dx.doi.org/10.1093/mnras/stw1138`.

Seo, Hee-Jong, Jonathan Eckel, et al. (Aug. 2010). “High-Precision Predictions For The Acoustic Scale In The Nonlinear Regime”. In: *The Astrophysical Journal* 720.2, pp. 1650–1667. ISSN: 1538-4357. DOI: 10.1088/0004-637x/720/2/1650. URL: http://dx.doi.org/10.1088/0004-637X/720/2/1650.

Seo, Hee-Jong and Daniel J. Eisenstein (Nov. 2005). “Baryonic Acoustic Oscillations in Simulated Galaxy Redshift Surveys”. In: *The Astrophysical Journal* 633.2, pp. 575–588. DOI: 10.1086/491599. URL: https://doi.org/10.1086%2F491599.

Seo, Hee-Jong, Ethan R. Siegel, et al. (Oct. 2008). “Nonlinear Structure Formation and the Acoustic Scale”. In: *The Astrophysical Journal* 686.1, pp. 13–24. ISSN: 1538-4357. DOI: 10.1086/589921. URL: http://dx.doi.org/10.1086/589921.

Springel, Volker (Dec. 2005). “The cosmological simulation code gadget-2”. In: *Monthly Notices of the Royal Astronomical Society* 364.4, pp. 1105–1134. ISSN: 0035-8711. DOI: 10.1111/j.1365-2966.2005.09655.x. eprint: https://academic.oup.com/mnras/article-pdf/364/4/1105/18657201/364-4-1105.pdf. URL: https://doi.org/10.1111/j.1365-2966.2005.09655.x.

Wang, Lile, Beth Reid, and Martin White (Nov. 2013). “An analytic model for redshift-space distortions”. In: *Monthly Notices of the Royal Astronomical Society* 437.1, pp. 588–599. DOI: 10.1093/mnras/stt1916. URL: https://doi.org/10.1093%2Fmnras%2Fstt1916.

Weinberg, David H. et al. (Sept. 2013). “Observational probes of cosmic acceleration”. In: *Physics Reports* 530.2, pp. 87–255. ISSN: 0370-1573. DOI: 10.1016/j.physrep.2013.05.001. URL: http://dx.doi.org/10.1016/j.physrep.2013.05.001.

Xu, Xiaoying et al. (Mar. 2013). “Measuring DA and H at z=0.35 from the SDSS DR7 LRGs using baryon acoustic oscillations”. In: *Monthly Notices of the Royal Astronomical Society* 431.3, pp. 2834–2860. ISSN: 0035-8711. DOI: 10.1093/mnras/stt379. URL: http://dx.doi.org/10.1093/mnras/stt379.

Zhao, Cheng et al. (Feb. 2021). “The completed SDSS-IV extended Baryon Oscillation Spectroscopic Survey: 1000 multi-tracer mock catalogues with redshift evolution and systematics for galaxies and quasars of the final data release”. In: *Monthly Notices of the Royal Astronomical Society* 503.1, pp. 1149–1173. DOI: 10.1093/mnras/stab510. URL: https://doi.org/10.1093%2Fmnras%2Fstab510.